Efficient Models for Rayleigh-Taylor and Richtmyer-Meshkov Instability

By

Gavin Pandya

DISSERTATION

Submitted in partial satisfaction of the requirements for the degree of

DOCTOR OF PHILOSOPHY

in

MATHEMATICS

in the

OFFICE OF GRADUATE STUDIES

of the

UNIVERSITY OF CALIFORNIA

DAVIS

Approved:

John Hunter

Sameer Iyer

Steve Shkoller, Chair

Committee in Charge

2025

© Gavin Pandya, 2025. All rights reserved.

This thesis is dedicated to my family and friends, near and far, who supported me in success and in failure, and without whom I never would have made it this far.

Contents

1 Introduction **1**

1.1 The Rayleigh-Taylor and Richtmyer-Meshkov instabilities 2

1.2 Difficulties associated with vortex-dominated flow 4

1.3 Overview and Contributions 5

2 Interface models for 3d RT problems **8**

2.1 Introduction 9

2.1.1 Outline 12

2.2 Interface models 13

2.2.1 The irrotational and incompressible Euler equations 18

2.2.2 The Need for Approximation 20

2.2.3 The 3D Lower-Order z-Model 21

2.2.4 The 3D Medium-Order and Higher-Order z-Models 25

2.2.5 Dynamics of Vorticity 27

2.3 Numerical Simulation and Validation against Experiments 30

2.3.1 Numerical Approximation of the z-Model 31

2.3.2 Convergence of the z-Model 34

2.3.3 Single-Mode Initial Data 35

2.3.4 The 3D Rocket Rig Experiment 38

2.3.5 Fluid mixing in the Rocket Rig experiment 42

2.3.6 Fluid Mixing in Complex Stratifications 47

2.4 Conclusions 50

3 A multiscale vortex method for compressible flow **53**

3.1 Introduction . . . 54

3.2 Governing equations . . . 55

3.2.1 The compressible Euler equations . . . 55

3.2.2 The incompressible Euler equations . . . 57

3.3 Review of the 2d z-model . . . 58

3.4 Review of the multiscale model of Ramani and Shkoller . . . 60

3.5 The multiscale z-model . . . 62

3.5.1 The two-phase compressible Euler equations . . . 63

3.5.2 The continuous-singular decomposition . . . 64

3.5.3 The full multiscale system . . . 67

3.5.4 Boundary conditions for the Birkhoff-Rott integral . . . 68

3.6 Numerical Method . . . 69

3.6.1 Spatial discretization . . . 71

3.6.2 The continuous part . . . 71

3.6.3 Computation of the Atwood number . . . 72

3.6.4 The singular part . . . 73

3.6.5 Temporal discretization . . . 74

3.7 Examples . . . 76

3.7.1 Single-mode Rayleigh-Taylor instability . . . 76

3.7.2 Single-mode Richtmyer-Meshkov instability . . . 81

3.7.3 Radial implosion/explosion problem . . . 85

3.8 Conclusions . . . 91

Chapter 1

Introduction

1.1 The Rayleigh-Taylor and Richtmyer-Meshkov instabilities

The Rayleigh Taylor and Richtmyer-Meshkov instabilities occur at the interface between two fluids of different densities, ρ^+ and ρ^-, when subjected to a non-normal pressure gradient. The misalignment of density and pressure gradients generates baroclinic torque $\frac{1}{\rho^2}\nabla\rho \times \nabla p$, and deposits vorticity on the material interface. In the case of a sustained pressure gradient—due to the force of gravity, for example—we obtain Rayleigh-Taylor (RT) instability, while in the case of an impulsive pressure gradient—due to the passage of a shock wave—we obtain Richtmyer-Meshkov (RM) instability. These instabilities are ubiquitous in scientific and engineering applications of fluid dynamics, ranging from a astrophysical processes such as stellar convection and supernova remnants, to inertial confinement fusion (ICF) implosions (Cabot and Cook, 2006; Zhou et al., 2021). One may even observe Rayleigh-Taylor instability from the comfort of one's own home, as I did when I captured the following image of cloud mixing from my apartment window (Figure 1.1).



Figure 1.1: Rayleigh-Taylor instability in clouds, compared against simulations.

Linear analysis of the Euler equations in the presence of a constant gravitational acceleration g shows that small perturbations of wavenumber k grow like $e^{\lambda t}$, where

$$\lambda = \sqrt{Agk}, \qquad A = \frac{\rho^+ - \rho^-}{\rho^+ + \rho^-},$$

(Rayleigh, 1883; Taylor, 1950). The number A is called the *Atwood number*, and is an essential parameter in the analysis of these instabilities. Note that these perturbations do not grow unless the Atwood number is positive; or in other words unless the upper fluid ρ^+ is denser than the lower fluid ρ^-. This is no surprise—oil floats stably on top of water, but trying to float water on top of oil would result in violent instability. On the other hand, if a shock wave accelerates the interface to a velocity U from rest, small perturbations of wavenumber k grow like λt, where

$$\lambda = AU\varepsilon k,$$

where ε is the initial amplitude of the perturbation. For both RT and RM instability, linear analysis predicts that the growth rate tends to infinity as the wavenumber of the perturbation becomes large, and hence that microscopic perturbations can quickly have a macroscopic effect on the dynamics. In reality, nonlinear effects cause energy to cascade from small to large scales (and back again), eventually transitioning to a state of turbulent mixing. Accurately capturing these multi-scale vortex dynamics poses a significant challenge to numerical simulations, as it requires resolving sharp gradients in velocity, pressure, and density, which demand fine spatial and temporal resolution. Moreover, the numerical dissipation inherent to most discretization schemes can suppress small-scale structures critical to turbulent mixing, leading to an underprediction of mixing rates and energy spectra. Predicting the rate of mixing in such systems, and developing mechanisms by which one can enhance or suppress the rate of mixing, are key questions for various engineering applications, most notably for improving the fusion yield in inertial confinement fusion (Zhou et al., 2021, 2025).

1.2 Difficulties associated with vortex-dominated flow

The governing equations for the fluid flows considered in this work are the *compressible Euler equations*, which take the form

$$\begin{aligned} \partial_t \rho + \nabla \cdot (\rho \boldsymbol{u}) &= 0, \\ \partial_t (\rho \boldsymbol{u}) + \nabla \cdot (\rho \boldsymbol{u} \otimes \boldsymbol{u}) + \nabla p &= 0, \\ \partial_t (\rho e) + \nabla \cdot ((\rho e + p) \boldsymbol{u}) &= 0, \end{aligned}$$

where ρ is the density of the fluid, $\boldsymbol{u}$ its velocity, e its specific energy, and p its pressure. The compressible Euler equations are a system of *hyperbolic conservation laws*, with a finite speed of propagation. Its wave speeds are given by $\boldsymbol{u} \cdot \boldsymbol{n} - c$, $\boldsymbol{u} \cdot \boldsymbol{n}$, and $\boldsymbol{u} \cdot \boldsymbol{n} + c$, where $\boldsymbol{n}$ is a unit vector specifying the direction of propagation and c is the *sound speed*,

$$c = \left(\frac{\partial p}{\partial \rho} \right)^{\frac{1}{2}}.$$

In vorticity-dominated flows, the speed of wave propagation is often much faster than the characteristic speed of vortex motion. Moreover, it is necessary for the stability of numerical simulations to resolve the propagation of acoustic waves. Consequently, it is often useful to consider a mathematical model which filters out these acoustic waves in order to more efficiently simulate vortex-dominated flow where compressible effects are not too strong. The strength of compressible effects is measured using the *Mach number*,

$$M = \frac{|\boldsymbol{u}|}{c}.$$

Contact-dominated compressible flows, such as those governed by Rayleigh-Taylor or Richtmyer-Meshkov instabilities, exhibit sharp shear layers and concentrated vorticity localized near material interfaces, but may exhibit relatively low Mach numbers. In the nearly-incompressible regime—where the fluid Mach number $M \ll 1$—the compressible Euler equations become stiff, as acoustic waves travel much faster than the convective flow. This leads to numerical difficulties: time step restrictions from the CFL condition make explicit schemes inefficient, while standard compressible

solvers fail to capture the correct low-Mach asymptotics. In this setting, the pressure ceases to behave as a thermodynamic variable and instead enforces a near-incompressibility constraint on the velocity field. Conventional shock-capturing schemes misrepresent this role, generating spurious compressibility effects and unphysical entropy production that distort vortex dynamics and degrade the accuracy of long-time simulations. These issues are especially damaging in baroclinic vorticity production—the principal mechanism driving RT and RM instabilities—where small numerical errors in pressure or density gradients can substantially alter the structure and magnitude of the vorticity field.

In flows where compressibility is weak, it is useful to consider the incompressible limit of the Euler equations as $M \to 0$. The resulting system, derived formally from full compressible Euler, filters out acoustic waves while retaining the convective and vortical dynamics relevant for instability growth. In this limit, pressure acts purely as a Lagrange multiplier to enforce incompressibility of the velocity field. For vortex-dominated flows, this approximation is attractive because it eliminates the stiff acoustic modes that make compressible simulations computationally expensive. The z-model presented in Chapter 2 is an illustrative example of the efficiency gains which can be obtained from the use of incompressible models. See Figure 1.2 for an example of the fine scales present in incompressible Rayleigh-Taylor instability. However, not all problems can be treated accurately with an incompressible model equation, even when the Mach number is low. Therefore, in Chapter 3, we have presented a hybrid method for compressible flow, based on a generalization of the z-model, which takes advantage of the small-scale structure afforded by the z-model, while coupling to a background compressible flow which accounts for bulk compression and vorticity.

1.3 Overview and Contributions

In Chapter 2, we develop a suite of reduced-order interface models—collectively termed the z-models—for the efficient simulation of Rayleigh–Taylor instability. These instabilities are driven by interfacial vorticity, produced through baroclinic torque in variable-density flows, and are characterized by complex, multiscale roll-up dynamics. We validate these models against both classical single-mode and random multi-mode RTI experiments, demonstrating their ability to capture universal growth rates, self-similar density profiles, and optimal viscous mixing under ensemble av-

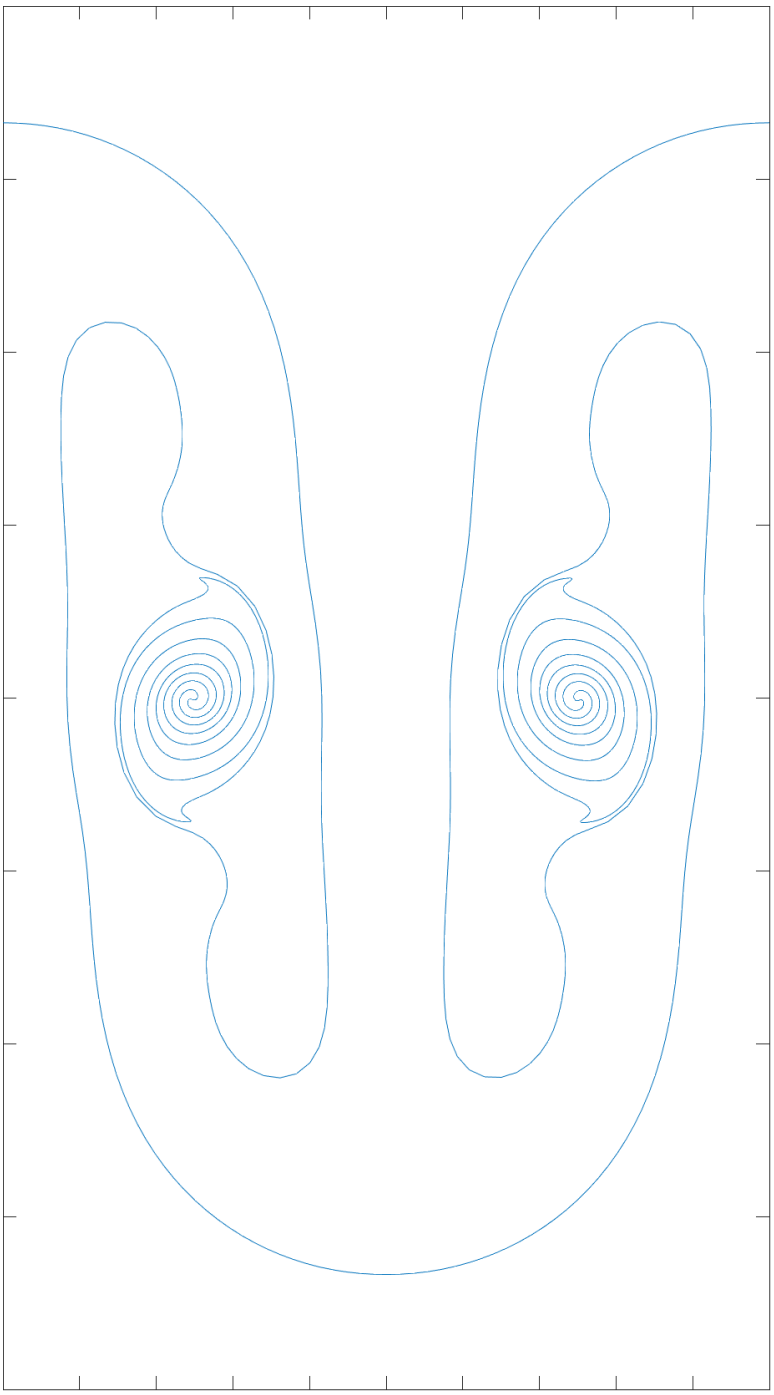


Figure 1.2: Single-mode Rayleigh-Taylor instability, computed using a 2d incompressible vortex method (2d higher-order z-model).

eraging. Furthermore, we generalize the models to handle stratified multi-fluid configurations and use them to investigate the stabilizing effects of intermediate fluid layers on mixing layer growth.

Chapter 3 extends this methodology to compressible flows via a multiscale hybrid framework that couples a high-resolution interface model to a coarse-grid compressible background solver. We conclude with numerical demonstrations of this compressible multiscale model on canonical RTI and RMI problems, along with a perturbed radial explosion case, illustrating its flexibility, efficiency, and physical fidelity.

Chapter 2

Interface models for 3d RT problems

This chapter contains material published in the Journal of Fluid Mechanics, Vol. 959, "Interface models for three-dimensional Rayleigh–Taylor instability" by G. Pandya and S. Shkoller, 2023.

2.1 Introduction

Rayleigh-Taylor instability (RTI) occurs when the interface between two fluids of different density is subjected to a normal pressure gradient. When a fluid undergoes RTI, vorticity is deposited on the material interface separating the two fluids. This interface vorticity then initiates the Kelvin-Helmholtz instability (KHI), which causes the interface to roll-up into extremely complex shapes. RTI is fundamental to a wide variety of complex physical processes, and is often coupled to the effects of electromagnetism, gravity, reaction chemistry, or combustion, as well as the effects of shock waves and Richtmeyer-Meshkov instability. For a comprehensive review of the state of the art in the theory, computation, and application of RTI, see the two-part review of Zhou (2017b,a).

Our objective is the analysis and quantification of certain universal aspects of RTI by a novel derivation and implementation of reduced-order interface models. Specifically, we wish to make use of the dimensional reduction afforded by irrotational, incompressible, and inviscid fluids, coupled to an asymptotic expansion in the non-locality of the flow to derive accurate models of complex interface motion, which allow for roll-up, small-scale structure formation, multiple interface interaction and stratification, and viscous mixing via ensemble averaging of large sets of randomly initialized inviscid RTI runs. There are certain universal features associated with the RT instability that have been discovered experimentally, derived analytically by turbulence closure models, or established via Direct Numerical Simulation (DNS) which are fundamental to our understanding of turbulence. We are particularly interested in the universality of (a) the Froude number for bubble growth under a single-mode RT instability which, in turn, implies that the asymptotic bubble velocity depends only bubble size; (b) the theoretically and experimentally predicted quadratic growth rate of the interface amplitude under random multi-mode perturbations, (c) the optimal (viscous) mixing rates induced by the RT instability, and the self-similar evolution of horizontally averaged density profiles; (d) the persistent formation of small-scale features due to multiple fluid interface interactions; and finally (e) the remarkable self-similar stabilization of the mixing layer growth rate which arises for the three-fluid two-interface heavy-light-heavy configuration, in which the addition of a third fluid bulk slows the growth of the mixing layer to a linear rate (as opposed to the standard quadratic growth rate for two fluid RTI).

Historically, early studies of RTI focused on the development of single-mode perturbations of

a flat interface, and studied questions concerning the nonlinear growth of these perturbations and their longtime behavior (Wilkinson and Jacobs, 2007). For instance, the asymptotic bubble/spike velocity of single-mode RTI appears to be a universal feature of bubbly flows, depending only on the size of the bubble, although there is some evidence of "re-acceleration" of bubbles at very late times (Ramaprabhu et al., 2006). For many engineering and physics applications, the quantification of the growth of the mixing-layer and the rate of fluid mixing in RTI-driven turbulence is of fundamental importance (Sharp, 1984). For example, the growth of the mixing layer in turbulent RTI has been an area of intense study for decades, starting with Read (1984). The growth of the interface amplitude is the natural quantity to measure in a variety of experimental settings, exhibiting a universal quadratic growth rate at long times due to nonlinear mode interactions, as well as a self-similar scaling of the density profile (Boffetta et al., 2010). However, interesting questions remain about the dependence of the non-dimensional growth-rate parameter upon the spectrum of the initial perturbation (Ristorcelli and Clark, 2004), so that a correct prediction of this growth rate is essential to the study of RTI. In practical terms, this predicted amplitude growth rate is a measure of the growth of the mixing-layer in the case that fluids have viscosity. It is of paramount interest to understand how fast multiple fluids *mix* under the action the RT interface instability. This rate can be quantified by the so-called "mix norms" which are defined in Lin et al. (2011). Therein, it was shown that for passive scalar transport by a specially constructed (shear-type) transport velocity, optimal mixing occurs in the sense of exponentially fast convergence to the scalar average. While no theorems as yet exist for the case of mixing by the Navier-Stokes equations (or any other fluids equations for that matter), there is also very little numerical evidence of optimal mixing under RTI. The development of our reduced-order interface models is intended for the study of these fundamental behaviors.

Well-known reduced-order models which have been used to study the interface growth rate under RTI are the Haan and Goncharov models, which approximate single-mode and multi-mode initial perturbations, respectively (Haan, 1989; Goncharov, 2002). All the aforementioned models assume that the interface remains a graph; as such, these models have limited accuracy and predictive capabilities beyond the linear stage of the interface motion (see Rollin and Andrews, 2013).

Herein, we shall derive interface models for the Rayleigh-Taylor instability by a suitable approximation of the multi-phase irrotational and incompressible Euler equations. Specifically, with

the aim of preserving the geometric complexity of RTI, we do not use traditional asymptotic assumptions of smallness in either amplitude or slopes. Instead, we use an asymptotic expansion of the interaction potential between interfacial particle positions to derive reduced-order approximations of the Euler equations, with a general parametrization which allows for interface turnover and roll-up. This process results in three interface models for Rayleigh-Taylor problems which we shall refer to as z-models. These three z-models are nonlocal evolution equations for the interface parametrization $\boldsymbol{z} = (z^1, z^2, z^3)$ and the vortex sheet density on the interface $\boldsymbol{\mu} = (\mu_1, \mu_2)$. The velocity is then obtained by Laplacian inversion via an approximation of the Birkhoff-Rott singular integral kernel. Our z-models are presented in what we term low-order, medium-order, and high-order variants, corresponding to the amount of nonlocality each model retains from the original Euler system. We note that our initial derivation of the z-models are for a two-phase flow with one material interface, but we shall also provide a generalization to the case of n fluid interfaces with $n \geqslant 1$.

After deriving the z-models using our asymptotic method in non-locality, we present a simple numerical discretization, which runs two orders of magnitude faster than traditional numerical methods for the Euler equations, and use it to study universality in RTI. We begin with single-mode RTI and compute the evolution of the bubble and spike Froude numbers, dimensionless quantities measuring the ratio of inertial to gravitational effects on RT bubble and spike motion. Then we reproduce results from the classical "rocket rig" experiments of Read (1984) and Youngs (1984), on the growth rate of turbulent RT mixing layers, and compare against more recent models for mixing layer development of Ristorcelli and Clark (2004) and Cabot and Cook (2006). Due to the speed of our model, we are able to quickly compute emsemble-averaged quantities such as the density field, and we show that this closely matches the self-similar density distribution computed from a so-called Prandtl closure model. In addition, using the standard mixing norms introduced in Mathew et al. (2005), we demonstrate that the ensemble-averaged density field (associated to many simulations initiated with randomly perturbed data) reproduces optimal mixing rates for a passive scalar, a property which has only been proven for specially chosen (shear-type) transport velocities (Thiffeault, 2012). Finally, as we noted above, we generalize our z-model to allow for multiple fluid interfaces and use this to corroborate experimental evidence from Jacobs and Dalziel (2005) on the self-similarity of the species fraction profile in *three*-phase fluid problems, which in turn shows that

the presence of multiple fluid layers has an important effect on the long-time growth of the mixing layer.

2.1.1 Outline

In Section 2.2, we motivate and derive a class of interface models using a new type of asymptotic expansion in nonlocality. In Section 2.2.1, we formulate the two-phase irrotational and incompressible Euler equations as a system of singular integral equations for the fluid interface parameterization and the vorticity measure on the interface. In Section 2.2.2, we outline the difficulty of numerically simulating the boundary integral formulation of the Euler equations, and explain the need for simplified models for interface evolution in RTI. In Section 2.2.3, we compute the leading order terms in an asymptotic expansion of the Birkhoff-Rott kernel, and derive the so-called lower-order z-model, which is a fast modal model for interface evolution in RTI which allows for interface turnover. In Section 2.2.4, we introduce the medium- and higher-order z-models, which are modifications of the lower-order z-model which include increasing amounts of nonlocality from the original Euler system. Finally, in Section 2.2.5, we perform some basic analysis indicating that the modifications we have made in formulating the z-models are appropriate for the regime under consideration.

In Section 2.3, we describe a numerical discretization of the z-models, and validate our models against a variety of classical Rayleigh-Taylor test problems. In Section 2.3.1, we describe our numerical method, and demonstrate its large-scale convergence properties in Section 2.3.2. We validate our model against experiments initialized with both single-mode initial data (Section 2.3.3) as well as random multi-mode initial data (Section 2.3.4). In Section 2.3.5, we compute ensemble-averaged quantities from many z-model runs using data with random fluctuations, and demonstrate that we are able to model viscous mixing layers with optimal mixing rates. In Section 2.3.5, we use a so-called Prandtl closure model to produce a self-similar solution for the density profile, and show that it compares well with results from our z-model. In Section 2.3.6, we use our z-model to study stratified flows containing unstable density interfaces, and demonstrate self-similarity in the ensemble-averaged species fraction profile.

2.2 Interface models

When the fluids are inviscid, incompressible, and irrotational in their respective bulks, the 3D Euler equations can be written as boundary integral equations involving only the interface position and the vortex sheet density on the interface. In three dimensions, these nonlocal integral equations were first derived and simulated by Baker et al. (1984), following the earlier derivation by Birkhoff (1962) and Rott (1956) for vortex sheets in 2D flows. We consider two immiscible, inviscid, incompressible, irrotational fluids occupying two open volumes $\Omega^+(t)$ and $\Omega^-(t)$ in $\mathbb{R}^3$, separated by a time-dependent material interface $\Gamma(t)$, where t denotes time. The evolution of the fluid is restricted to a time interval $0 \leqslant t \leqslant T$, and is modeled by the incompressible and irrotational Euler equations, which can be written as

$$\left.\begin{aligned} \rho^\pm(\partial_t \boldsymbol{u}^\pm + \boldsymbol{u}^\pm \cdot \boldsymbol{\nabla}\boldsymbol{u}^\pm) + \boldsymbol{\nabla} p^\pm &= -g\rho^\pm \boldsymbol{e}_3 \\ \partial_t \rho^\pm + \boldsymbol{u}^\pm \cdot \boldsymbol{\nabla}\rho^\pm &= 0 \end{aligned}\right\} \quad \text{in} \quad \Omega^\pm(t)\,, \quad 0 < t \leqslant T\,, \tag{2.2.1}$$

with the constraints that

$$\operatorname{div} \boldsymbol{u}^\pm = 0 \quad \text{and} \quad \operatorname{curl} \boldsymbol{u}^\pm = \boldsymbol{0} \quad \text{in} \quad \Omega^\pm(t)\,, \quad 0 \leqslant t \leqslant T\,.$$

The initial interface $\Gamma(0)$ is specified and hence so too are the initial domains $\Omega^\pm(0)$, and initial conditions for velocity and density are given:

$$\boldsymbol{u}^\pm(\boldsymbol{x}, 0) = \mathring{\boldsymbol{u}}^\pm(\boldsymbol{x})\,, \quad \rho^\pm(\boldsymbol{x}, 0) = \mathring{\rho}^\pm(\boldsymbol{x}) \quad \text{in} \quad \Omega^\pm(0)\,.$$

Here, $\boldsymbol{u}^\pm$ denotes the velocity and $p^\pm$ denotes the pressure in $\Omega^\pm(t)$, while g represents the gravitational acceleration, and the unit vector $\boldsymbol{e}_3 = (0, 0, 1)$. We assume constant initial density functions $\rho^\pm$ in $\Omega^\pm(0)$, which implies that $\rho^\pm$ remain constant functions in $\Omega^\pm(t)$. Our focus is on flows in which $\Gamma(t)$ denotes a vortex sheet, and hence we supplement the Euler equations with the following jump conditions on $\Gamma(t)$:

$$\left.\begin{aligned} [\![p]\!] &= 0 \\ [\![\boldsymbol{u} \cdot \boldsymbol{n}]\!] &= 0 \end{aligned}\right\} \quad \text{for} \quad 0 \leqslant t \leqslant T\,, \tag{2.2.2a}$$

where n denotes the unit normal to $\Gamma(t)$, and $[\![f]\!] = f^+ - f^-$ on $\Gamma(t)$. In this manuscript we restrict our attention to flows where surface tension is negligible, but in general the condition $[\![p]\!] = 0$ is replaced by the Young-Laplace law $[\![p]\!] = 4\sigma H$, where σ is the coefficient of surface tension and H is the mean curvature of the interface $\Gamma(t)$. We assume that $\rho^+ \neq \rho^-$ so that

$$[\![\rho]\!] \neq 0 \quad \text{on} \quad \Gamma(t) \quad \text{for} \quad 0 \leqslant t \leqslant T\,. \tag{2.2.2b}$$

Because of (2.2.2a) and (2.2.2b), even if $\mathring{\boldsymbol{u}}^+ = \mathring{\boldsymbol{u}}^-$ on $\Gamma(0)$, the tangential component of velocity becomes discontinuous across $\Gamma(t)$ and we have that

$$[\![\boldsymbol{u} \cdot \boldsymbol{\tau}_\alpha]\!] \neq 0 \quad \text{on} \quad \Gamma(t) \quad \text{for} \quad 0 < t \leqslant T\,, \quad \alpha = 1, 2\,. \tag{2.2.2c}$$

Here, $\boldsymbol{\tau}_1$ and $\boldsymbol{\tau}_2$ are the unit tangent vectors to $\Gamma(t)$, chosen such that $(\boldsymbol{\tau}_1, \boldsymbol{\tau}_2, \boldsymbol{n})$ form a right-handed orthonormal basis. To complete the description of the dynamics, the motion of the interface $\Gamma(t)$ is governed by the normal component of the fluid velocity. Letting $\mathcal{V}(\Gamma(t))$ denote the normal speed of the interface,

$$\mathcal{V}(\Gamma(t)) = \boldsymbol{u} \cdot \boldsymbol{n}\,. \tag{2.2.3}$$

Let (x^1, x^2, x^3) denote the standard Euclidean coordinates on $\mathbb{R}^3$, and let (s^1, s^2) denote coordinates on $\mathbb{R}^2$, used to parameterize $\Gamma(t)$. Specifically, the time-dependent interface $\Gamma(t)$ is parametrized by a smooth function $\boldsymbol{z} : \mathbb{R}^2 \times [0, T] \to \mathbb{R}^3$ and

$$\Gamma(t) = \{\boldsymbol{z}(s^1, s^2, t) \ : (s^1, s^2) \in \mathbb{R}^2\,,\ t \in [0, T]\}\,,\ \boldsymbol{z} = (z^1, z^2, z^3)\,. \tag{2.2.4}$$

We use Latin indices for coordinates in Euclidean space, and Greek indices for coordinates on $\Gamma(t)$, and we will apply Einstein's summation convention without further comment. Euclidean space is endowed with the standard diagonal metric δ_{ij}, and the induced metric on $\Gamma(t)$ is given by

$$h = h_{\alpha\beta} \mathrm{d}s^\alpha \otimes \mathrm{d}s^\beta\,, \qquad\qquad h_{\alpha\beta} = \partial_\alpha \boldsymbol{z} \cdot \partial_\beta \boldsymbol{z}\,.$$

We set

$$|h| = \det h\,, \qquad\qquad \sqrt{h} = \sqrt{\det h}\,.$$

With respect to the parameterization (2.2.4), the time-dependent unit normal is given by

$$\boldsymbol{n} = \frac{\partial_1 \boldsymbol{z} \times \partial_2 \boldsymbol{z}}{\sqrt{h}}\,.$$

As noted above, we assume that the vorticity vanishes in the open sets $\Omega^+(t)$ and $\Omega^-(t)$, but on the material interface $\Gamma(t)$, the tangential component of velocity experiences a jump discontinuity, resulting in a vorticity measure $\boldsymbol{\omega}(s,t)$ concentrated on the interface. The velocity in $\Omega^+(t) \cup \Omega^-(t)$ is computed from this vorticity measure using the Birkhoff-Rott integral

$$\boldsymbol{u}(\boldsymbol{x},t) = \frac{1}{4\pi} \iint\limits_{\mathbb{R}^2} \boldsymbol{\omega}(s,t) \times \frac{\boldsymbol{x} - \boldsymbol{z}(s,t)}{|\boldsymbol{x} - \boldsymbol{z}(s,t)|^3} \mathrm{d}s\,, \tag{2.2.5}$$

where

$$\boldsymbol{\omega} = \omega^\alpha \partial_\alpha \boldsymbol{z}$$

and ω^α, $\alpha = 1, 2$ denote the components of the vorticity measure with respect to the basis $\partial_\alpha \boldsymbol{z}$. To be more precise, $\boldsymbol{\omega}(s,t) = \boldsymbol{\omega}(s^1, s^2, t)$ denotes the the vortex sheet *density* and is often referred to as the *amplitude of vorticity* or simply the vorticity measure on $\Gamma(t)$. When evaluated on $\Gamma(t)$ (or equivalently, along the parameterization $\boldsymbol{z}(s,t)$), the Birkhoff-Rott integral exists in the principal value sense, and gives the average velocity

$$\bar{\boldsymbol{u}} = \tfrac{1}{2}(\boldsymbol{u}^+ + \boldsymbol{u}^-) \circ \boldsymbol{z}\,, \tag{2.2.6}$$

where the '$\circ$' denotes composition. In particular, by choosing the Lagrangian parameterization $\boldsymbol{z}(s,t)$ such that $\partial_t \boldsymbol{z}(s,t) = \frac{1}{2}(\boldsymbol{u}^+ + \boldsymbol{u}^-)(\boldsymbol{z}(s,t),t)$ with $\boldsymbol{z}(s,0) = s^1 \boldsymbol{e}_1 + s^2 \boldsymbol{e}_2$, we have that

$$\partial_t \boldsymbol{z}(s,t) = \bar{\boldsymbol{u}}(s,t) := \frac{1}{4\pi} \iint\limits_{\mathbb{R}^2} \boldsymbol{\omega}(s',t) \times \frac{\boldsymbol{z}(s,t) - \boldsymbol{z}(s',t)}{|\boldsymbol{z}(s,t) - \boldsymbol{z}(s',t)|^3} \mathrm{d}s'\,. \tag{2.2.7}$$

where s' is a dummy variable for integration. Let us remark that according to (2.2.3), it is only the normal component of $\boldsymbol{u}$ that determines the shape of $\Gamma(t)$, and there exists an infinite-dimensional

tangential reparameterization symmetry of the interface which does not change its shape. This means that a different parameterization $\boldsymbol{z}(s,t)$ such that $\partial_t \boldsymbol{z} \cdot \boldsymbol{n}(\boldsymbol{z},t) = \bar{\boldsymbol{u}}(\boldsymbol{z},t) \cdot \boldsymbol{n}(\boldsymbol{z},t)$ but $\partial_t \boldsymbol{z} \cdot \boldsymbol{\tau}_\alpha(\boldsymbol{z},t) \neq \bar{\boldsymbol{u}}(\boldsymbol{z},t) \cdot \boldsymbol{\tau}_\alpha(\boldsymbol{z},t)$ would provide the same shape for $\Gamma(t)$, but would alter the distribution of particles along the interface. For our purposes, the Lagrangian parameterization (2.2.7) is a convenient choice, as the resulting evolution equation (2.2.18b) takes a particularly simple form.

We may write the vorticity measure $\boldsymbol{\omega}$ on $\Gamma(t)$ in terms of the velocity jump

$$\boldsymbol{w} = (\boldsymbol{u}^+ - \boldsymbol{u}^-) \circ \boldsymbol{z}\,, \tag{2.2.8}$$

in the form

$$\boldsymbol{\omega} = (\boldsymbol{w} \cdot \partial_2 \boldsymbol{z}) \partial_1 \boldsymbol{z} - (\boldsymbol{w} \cdot \partial_1 \boldsymbol{z}) \partial_2 \boldsymbol{z}\,, \tag{2.2.9}$$

so that $\boldsymbol{w} \cdot \partial_2 \boldsymbol{z} = \boldsymbol{\omega} \cdot \partial_1 \boldsymbol{z}$ and $\boldsymbol{w} \cdot \partial_1 \boldsymbol{z} = -\boldsymbol{\omega} \cdot \partial_2 \boldsymbol{z}$. Some of the difficulty of vortex methods stem from the computation of the Birkhoff-Rott velocity; specifically, a straightforward numerical quadrature results in chaotic motion of the interface (Krasny, 1986a). Let us describe our method of evaluation. Equation (2.2.7) may be rewritten as

$$\bar{\boldsymbol{u}}(s,t) = \iint_{\mathbb{R}^2} \boldsymbol{\omega}(s',t) \times \boldsymbol{\nabla} G(\boldsymbol{z}(s,t) - \boldsymbol{z}(s',t)) \mathrm{d}s'\,, \tag{2.2.10}$$

where $G(x) = (4\pi|x|)^{-1}$ is the fundamental solution of the Laplacian in $\mathbb{R}^3$. Note that (2.2.5) is defined everywhere in the bulk $\Omega^+(t) \cup \Omega^-(t)$ and has arguments $(x^1, x^2, x^3, t) \in \mathbb{R}^3 \times [0,T]$, while (2.2.7) is well-defined on the interface $\Gamma(t)$ and has arguments $(s^1, s^2, t) \in \mathbb{R}^2 \times [0,t]$. To avoid the singularity in the integral (2.2.10), we replace G by a regularized function

$$G^\epsilon(\boldsymbol{x}) = \frac{1}{4\pi\sqrt{\epsilon^2 + |\boldsymbol{x}|^2}},$$

where $\epsilon > 0$ and G^ϵ converges weakly to G as $\epsilon \to 0$. This results in the regularized Birkhoff-Rott velocity

$$\bar{\boldsymbol{u}}^\epsilon(s,t) = \frac{1}{4\pi} \iint_{\mathbb{R}^2} \boldsymbol{\omega}(s',t) \times \frac{\boldsymbol{z}(s,t) - \boldsymbol{z}(s',t)}{\left(\epsilon^2 + |\boldsymbol{z}(s,t) - \boldsymbol{z}(s',t)|^2\right)^{3/2}} \mathrm{d}s'. \tag{2.2.11}$$

This particular regularization was chosen for algebraic simplicity and falls under the well-known

umbrella of *vortex blob methods* (see, for example, Krasny, 1986b).

These are methods where the standard Green's function, satisfying $\Delta G = \delta$, is replaced with a regularized Green's function satisfying

$$\Delta G^\epsilon(\boldsymbol{x}) = \psi^\epsilon(\boldsymbol{x}) := \frac{1}{\epsilon^3}\psi\left(\frac{\boldsymbol{x}}{\epsilon}\right),$$

where ψ is a smooth, nonnegative function with most of its mass near zero and $\int_{\mathbb{R}^3}\psi = 1$. This kind of regularization has the effect of replacing a singular vorticity distribution $\boldsymbol{\omega}(\boldsymbol{x}) = \boldsymbol{\omega}_0\delta(\boldsymbol{x}-\boldsymbol{x}_0)$ with a smooth 'vortex blob' of finite size $\boldsymbol{\omega}(\boldsymbol{x}) = \boldsymbol{\omega}_0\psi^\epsilon(\boldsymbol{x}-\boldsymbol{x}_0)$. For our choice of regularization,

$$\psi(\boldsymbol{x}) = \frac{3}{4\pi}\frac{1}{(1+|\boldsymbol{x}|^2)^{\frac{5}{2}}}. \tag{2.2.12}$$

With this regularization employed, we may evaluate $\bar{\boldsymbol{u}}^\epsilon$ with any standard 2D quadrature method. This allows us to obtain arbitrarily high-order spatial discretizations.

The regularization applied here represents averaging over a length of size ϵ, and has the effect of replacing an infinitely thin vortex sheet with a vortex sheet of finite width proportional to ϵ. In particular, discontinuous quantities like the density ρ are replaced by $\rho * \psi^\epsilon$, and the interface $\Gamma(t)$ represents the contour of volume fraction $1/2$, which has the effect of damping instability in the interface position at scales smaller than ϵ. In the event of a mixing transition to a space-filling vorticity field, the interface still makes sense as the contour of volume fraction $1/2$. In the high-Reynolds number limit, the instability takes place simultaneously at all scales down to the molecular, and is self-similar in the sense that the instability appears the same at every scale. Thus, by setting our regularization parameter ϵ, we allow the vorticity to be space-filling at scales $\propto\epsilon$, which smears out the instability at length scales $\lambda \ll \epsilon$ while maintaining an accurate picture at scales $\lambda \gg \epsilon$. For example, to simulate RTI in cloud formation as viewed from many kilometers away, one might set $\epsilon \sim 1\,\text{km}$ and achieve accurate results, despite the fact that the instability is taking place at all scales simultaneously.

2.2.1 The irrotational and incompressible Euler equations

Thanks to the irrotationality of the two fluids, we may write the velocities $\boldsymbol{u}^{\pm}$ in $\Omega^{\pm}(t)$ in terms of velocity potentials, $\boldsymbol{u}^{\pm} = \boldsymbol{\nabla}\varphi^{\pm}$, where $\varphi^{\pm}$ are governed by Bernoulli's law,

$$\begin{cases} \partial_t \varphi^+ + \frac{1}{2}|\boldsymbol{u}^+|^2 + gx^3 = -\frac{p^+}{\rho^+} & \text{in } \Omega^+(t) \\ \partial_t \varphi^- + \frac{1}{2}|\boldsymbol{u}^-|^2 + gx^3 = -\frac{p^-}{\rho^-} & \text{in } \Omega^-(t) \end{cases}, \tag{2.2.13}$$

and where (we recall that) $p^{\pm}$ denotes the pressure functions, $\rho^{\pm}$ denotes the density functions, and g denotes the gravitational acceleration. We assume that the two fluids have infinite extent, so that $\Omega^+(t) \cup \Gamma(t) \cup \Omega^-(t) = \mathbb{R}^3$. The jump conditions on $\Gamma(t)$ associated to (2.2.13) are given by (2.2.2).

To determine how the potential jump $\varphi^+ - \varphi^-$ varies along $\Gamma(t)$, we compose (2.2.13) with the parameterization $\boldsymbol{z}$ and apply the chain rule:

$$\begin{aligned} \partial_t((\varphi^+ - \varphi^-) \circ \boldsymbol{z}) &= (\boldsymbol{\nabla}\varphi^+ \circ \boldsymbol{z} - \boldsymbol{\nabla}\varphi^- \circ \boldsymbol{z}) \cdot \partial_t \boldsymbol{z} + \partial_t(\varphi^+ - \varphi^-) \circ \boldsymbol{z} = \boldsymbol{w} \cdot \bar{\boldsymbol{u}} + \partial_t(\varphi^+ - \varphi^-) \circ \boldsymbol{z}\,, \\ \partial_t((\varphi^+ + \varphi^-) \circ \boldsymbol{z}) &= (\boldsymbol{\nabla}\varphi^+ \circ \boldsymbol{z} + \boldsymbol{\nabla}\varphi^- \circ \boldsymbol{z}) \cdot \partial_t \boldsymbol{z} + \partial_t(\varphi^+ + \varphi^-) \circ \boldsymbol{z} = 2|\bar{\boldsymbol{u}}|^2 + \partial_t(\varphi^+ + \varphi^-) \circ \boldsymbol{z}\,. \end{aligned}$$

Here, $\boldsymbol{w} = \boldsymbol{u}^+ - \boldsymbol{u}^-$ is the velocity jump on $\Gamma(t)$. Note that $\bar{\boldsymbol{u}}$, defined by (2.2.10), and $\boldsymbol{w}$ are well-defined on $\Gamma(t)$, and are thus functions of (s^1, s^2) and t. We introduce the *Atwood number*

$$A = \frac{\rho^+ - \rho^-}{\rho^+ + \rho^-}\,.$$

By using (2.2.2a), we write

$$\left(\frac{p^+}{\rho^+} - \frac{p^-}{\rho^-}\right) + A\left(\frac{p^+}{\rho^+} + \frac{p^-}{\rho^-}\right) = (A+1)\frac{p^+}{\rho^+} + (A-1)\frac{p^-}{\rho^-} = 2\frac{p^+ - p^-}{\rho^+ + \rho^-} = 0. \tag{2.2.14}$$

Using (2.2.13)–(2.2.14) and the identity

$$|\boldsymbol{u}^{\pm}|^2 = \left|\bar{\boldsymbol{u}} \pm \tfrac{1}{2}\boldsymbol{w}\right| = |\bar{\boldsymbol{u}}|^2 \pm \bar{\boldsymbol{u}} \cdot \boldsymbol{w} + \tfrac{1}{4}|\boldsymbol{w}|^2\,,$$

we find that along $\Gamma(t)$,

$$\left(\frac{p^+}{\rho^+}-\frac{p^-}{\rho^-}\right)\circ\boldsymbol{z}=\left(\partial_t(\varphi^+-\varphi^-)+\tfrac{1}{2}\left(|\boldsymbol{u}^+|^2-|\boldsymbol{u}^-|^2\right)\right)\circ\boldsymbol{z}=\partial_t((\varphi^+-\varphi^-)\circ\boldsymbol{z})\,, \tag{2.2.15a}$$

$$\begin{aligned}\left(\frac{p^+}{\rho^+}+\frac{p^-}{\rho^-}\right)\circ\boldsymbol{z}&=\left(\partial_t(\varphi^++\varphi^-)+\tfrac{1}{2}\left(|\boldsymbol{u}^+|^2+|\boldsymbol{u}^-|^2\right)\right)\circ\boldsymbol{z}+2gz^3\\&=\partial_t((\varphi^+-\varphi^-)\circ\boldsymbol{z})-|\bar{\boldsymbol{u}}|^2+\tfrac{1}{4}|\boldsymbol{w}|^2+2gz^3\,.\end{aligned} \tag{2.2.15b}$$

Substitution of (2.2.15) into (2.2.14) results in

$$\partial_t((\varphi^+-\varphi^-)\circ\boldsymbol{z})+A\partial_t((\varphi^++\varphi^-)\circ\boldsymbol{z})+A\left(-|\bar{\boldsymbol{u}}|^2+\tfrac{1}{4}|\boldsymbol{w}|^2+2gz^3\right)=0. \tag{2.2.16}$$

It is convenient to introduce a "rotated" version of the vorticity components,

$$\mu_\alpha=\boldsymbol{w}\cdot\partial_\alpha\boldsymbol{z}\,.\quad(\alpha=1,2)\,,$$

Differentiating (2.2.16) with respect to s_α then yields

$$\partial_t(\mu_\alpha+2A\bar{\boldsymbol{u}}\cdot\partial_\alpha\boldsymbol{z})=A\partial_\alpha\left(|\bar{\boldsymbol{u}}|^2-\tfrac{1}{4}h^{\alpha\beta}\mu_\alpha\mu_\beta-2gz^3\right), \tag{2.2.17}$$

where $h^{\alpha\beta}$ is the (α,β) component of the inverse of the induced metric on $\Gamma(t)$:

$$h^{\alpha\beta}h_{\beta\gamma}=\delta^\alpha{}_\gamma.$$

The coupled system of equations (2.2.7) and (2.2.17) are written as

$$\partial_t\boldsymbol{z}=\bar{\boldsymbol{u}}\,, \tag{2.2.18a}$$

$$\partial_t(\mu_\alpha+2A\bar{\boldsymbol{u}}\cdot\partial_\alpha\boldsymbol{z})=A\partial_\alpha\left(|\bar{\boldsymbol{u}}|^2-\tfrac{1}{4}h^{\beta\gamma}\mu_\beta\mu_\gamma-2gz^3\right), \tag{2.2.18b}$$

and are an equivalent form of the 3D irrotational and incompressible Euler equations (2.2.1), giving the interface position $\boldsymbol{z}=(z^1,z^2,z^3)$ and the components of velocity jump $\mu=(\mu_1,\mu_2)$ (or equivalently, the vorticity measure). This results in a form of the Euler equations which have 3 independent variables instead of the usual 4. The system (2.2.18) is supplemented with the initial

conditions $\boldsymbol{z}(s,0) = \mathring{\boldsymbol{z}}(s)$ and $\mu_\alpha(s,0) = \mathring{\mu}_\alpha(s)$.

2.2.2 The Need for Approximation

The numerical solution of the singular integral form of the Euler equations (2.2.18) is difficult because of the time-derivative term $\partial_t(2A\bar{\boldsymbol{u}}\cdot\partial_\alpha\boldsymbol{z})$ in (2.2.18b). Expanding this term using (2.2.18a) shows that

$$\begin{aligned}\partial_t(2A\bar{\boldsymbol{u}}\cdot\partial_\alpha\boldsymbol{z}) = \frac{A}{2\pi}\iint_R \big(\mu_2(s)\partial_1\bar{\boldsymbol{u}}(s) - \mu_1(s)\partial_2\bar{\boldsymbol{u}}(s)\big)\times\frac{\boldsymbol{z}-\boldsymbol{z}(s)}{|\boldsymbol{z}-\boldsymbol{z}(s)|^3}\\ + \big(\partial_t\mu_2(s)\partial_1\boldsymbol{z}(s) - \partial_t\mu_1(s)\partial_2\boldsymbol{z}(s)\big)\times\frac{\boldsymbol{z}-\boldsymbol{z}(s)}{|\boldsymbol{z}-\boldsymbol{z}(s)|^3}\\ - \big(\mu_2(s)\partial_1\boldsymbol{z}(s) - \mu_1(s)\partial_2\boldsymbol{z}(s)\big)\times\big(\boldsymbol{z}-\boldsymbol{z}(s)\big)\frac{3(\bar{\boldsymbol{u}}-\bar{\boldsymbol{u}}(s))\cdot(\boldsymbol{z}-\boldsymbol{z}(s))}{|\boldsymbol{z}-\boldsymbol{z}(s)|^5}\mathrm{d}s\,.\end{aligned}$$

where we have not written the time-dependence in the integrand. Hence we see that (2.2.18) takes the form of a system of nonlinear and nonlocal integral equations for the time-derivatives $\partial_t(z^1, z^2, z^2, \mu_1, \mu_2)$. In addition to the difficulty of solving (2.2.18) caused by the term $\partial_t(2A\bar{\boldsymbol{u}}\cdot\partial_\alpha\boldsymbol{z})$, yet another challenge stems from fact that the Birkhoff-Rott integral can be time-consuming to evaluate: a naive implementation takes $O(N^2)$ operations for an N-point discretization of $\Gamma(t)$, although this can be improved greatly by the use of fast multipole methods. We are not aware of any successful attempts to directly simulate the singular integral form of the Euler equations (2.2.18), despite numerous simulations of these equations in two space dimensions and with axisymmetry. The models which we derive in the following sections make the appropriate reductions of the full incompressible and irrotational Euler equations so as to retain high accuracy in the interface position while avoiding the considerable numerical challenges that we have explained above.

In two dimensions, Granero-Belinchón and Shkoller (2017) remedied the computational difficulty of the Birkhoff-Rott velocity by introducing an approximate velocity which can be computed as a Hilbert transform, requiring only $O(N\log N)$ evaluations:

$$\widetilde{\boldsymbol{u}} = \frac{H\omega}{2|\partial_1\boldsymbol{z}|}\boldsymbol{n}, \qquad \widehat{Hf}(k) = -\mathrm{i}\,\mathrm{sgn}(k)\hat{f}(k). \tag{2.2.19}$$

The system (2.2.19) is the approximation which results from taking a limit of "small nonlocality"

(explained in detail in the sequel), which is accurate when the interface is not too curved; in particular, it was shown in Granero-Belinchón and Shkoller (2017) that

$$\max_{s\in\mathbb{R}} |\bar{\boldsymbol{u}}(s,t) - \widetilde{\boldsymbol{u}}(s,t)| \leqslant \frac{2}{\pi}\sqrt{3K}\int_{\Gamma(t)} \omega(s,t)^2\sqrt{h}\mathrm{d}s\,, \tag{2.2.20}$$

where K is the maximum curvature of the interface. Inserting the approximate velocity (2.2.19) into the 2D version of (2.2.18) provides a simple set of evolution equations for $\boldsymbol{z}$ and ω, called the 2D *lower-order z-model*. It was subsequently verified in Canfield et al. (2020) that the lower-order z-model agrees well with experimental data of Rayleigh-Taylor problems, forming a sort of "envelope" for the interface roll-up.

2.2.3 The 3D Lower-Order z-Model

The aim of this section is to introduce a 3D generalization of the 2D lower-order z-model of Granero-Belinchón and Shkoller (2017), as well as two more accurate models (with greater nonlocality), which we shall refer to as the "medium-order" and "higher-order" z-models. While already useful for 2D simulations (in respect to the speed-up over traditional Euler solvers), the need for such a simplification is even greater for 3D simulations.

For the remainder of this section, we omit writing the explicit dependence on time t. The derivation begins with the observation that the dominant contribution to the Birkhoff-Rott velocity $\bar{\boldsymbol{u}}(s)$ in (2.2.5) arises from the singular integrand in a small neighborhood of s. Expanding $\boldsymbol{z}(s')$ in a small neighborhood of s yields

$$\boldsymbol{z}(s') = \boldsymbol{z}(s) + \partial_\alpha \boldsymbol{z}(s)(s'^\alpha - s^\alpha) + \tfrac{1}{2}\partial_{\alpha\beta}\boldsymbol{z}(s)(s'^\alpha - s^\alpha)(s'^\beta - s^\beta) + O(|s-s'|^3)\,, \tag{2.2.21}$$

and the expansion of $\omega(s')$ about $\omega(s)$ is given by

$$\begin{aligned}\boldsymbol{\omega}(s') &= \mu_2(s')\partial_1\boldsymbol{z}(s') - \mu_1(s')\partial_2\boldsymbol{z}(s')\\ &= \mu_2(s')\partial_1\boldsymbol{z}(s) - \mu_1(s')\partial_2\boldsymbol{z}(s)\\ &\quad + \mu_2(s')\partial_{1\alpha}\boldsymbol{z}(s)(s'^\alpha - s^\alpha) - \mu_1(s')\partial_{2\alpha}\boldsymbol{z}(s)(s'^\alpha - s^\alpha) + O(|s-s'|^2)\,.\end{aligned} \tag{2.2.22}$$

The first-order expansion in (2.2.21) is useful in regions where the interface curvature is small, which is a valid assumption prior to interface roll-up or near bubble and spike tips. See section 2.2.5 for precise estimates of the error between the approximate and exact velocities, and compare figures 2.1 and 2.2 to see the effect of this low-curvature assumption. In order to expand $|\boldsymbol{z}(s)-\boldsymbol{z}(s')|^{-1}$ about the singular point $s=s'$, we expand $\boldsymbol{z}(s)-\boldsymbol{z}(s')$ about $s=s'$, factor the linear term of this expansion, and use the series expansion for $1/(1-\xi)$ about $\xi=0$; in particular, we have that

$$\begin{aligned}\frac{1}{|\boldsymbol{z}(s)-\boldsymbol{z}(s')|^3} &= \frac{1}{|\partial_\alpha \boldsymbol{z}(s)(s'^\alpha - s^\alpha)|^3}\left(\frac{|\boldsymbol{z}(s)-\boldsymbol{z}(s')|}{|\partial_\alpha \boldsymbol{z}(s)(s'-s)|}\right)^{-3} \\ &= \frac{1}{|\partial_\alpha \boldsymbol{z}(s)(s'^\alpha - s^\alpha)|^3}\left(1+\frac{1}{2}\frac{\partial_{\alpha\beta}\boldsymbol{z}(s)(s'^\alpha-s^\alpha)(s'^\beta-s^\beta)}{|\partial_\alpha \boldsymbol{z}(s)(s'^\alpha-s^\alpha)|}+\cdots\right)^{-3} \\ &= \frac{1}{|\partial_\alpha \boldsymbol{z}(s)(s'^\alpha - s^\alpha)|^3}\left(1-\frac{3}{2}\frac{\partial_{\alpha\beta}\boldsymbol{z}(s)(s'^\alpha-s^\alpha)(s'^\beta-s^\beta)}{|\partial_\alpha \boldsymbol{z}(s)(s'^\alpha-s^\alpha)|}+\cdots\right) \end{aligned} \tag{2.2.23}$$

The expansions (2.2.21)–(2.2.23), together with a somewhat tedious computation, show that the Birkhoff-Rott integrand $\omega(s')\times(\boldsymbol{z}(s)-\boldsymbol{z}(s'))/|\boldsymbol{z}(s)-\boldsymbol{z}(s')|^3$ has the following expansion about $s=s'$:

$$\begin{aligned}&\frac{(s^\alpha-s'^\alpha)}{\big(h_{\alpha\beta}(s)(s^\alpha-s'^\alpha)(s^\beta-s'^\beta)\big)^{\frac{3}{2}}}\Big(\mu_\alpha(s')+(s^\beta-s'^\beta)\big(\mu_\alpha(s')\partial_\beta\sqrt{h}-\tfrac{1}{2}\partial_{\alpha\beta}\boldsymbol{z}\cdot\partial_\gamma z)h^{\gamma\delta}(s)\mu_\delta(s')\big)\Big)\boldsymbol{n} \\ &\quad+\frac{(s^\alpha-s'^\alpha)(s^\beta-s'^\beta)}{\big(h_{\alpha\beta}(s)(s^\alpha-s'^\alpha)(s^\beta-s'^\beta)\big)^{\frac{3}{2}}}\Big(\mu_\alpha(s')\sqrt{h}\partial_\beta\boldsymbol{n}-\tfrac{1}{2}(\mu_2(s')\partial_1\boldsymbol{z}-\mu_1(s')\partial_2\boldsymbol{z})\times\boldsymbol{n}(\partial_{\alpha\beta}\boldsymbol{z}\cdot\boldsymbol{n})\Big) \\ &\quad-\frac{3}{2}\frac{\mu_\alpha(s')(s^\alpha-s'^\alpha)(s^\beta-s'^\beta)(s^\gamma-s'^\gamma)(s^\delta-s'^\delta)(\partial_{\alpha\beta}\boldsymbol{z}\cdot\partial_\gamma\boldsymbol{z})\partial_\delta\boldsymbol{z}}{\big(h_{\alpha\beta}(s)(s^\alpha-s'^\alpha)(s^\beta-s'^\beta)\big)^{\frac{5}{2}}}\boldsymbol{n}+O(1)\,. \end{aligned} \tag{2.2.24}$$

Isolating the dominant contribution, we thus have that

$$\boldsymbol{\omega}(s')\times\frac{\boldsymbol{z}(s)-\boldsymbol{z}(s')}{|z(s)-z(s')|^3}=\frac{\mu_1(s')(s^1-s'^1)+\mu_2(s')(s^2-s'^2)}{\big(h_{\alpha\beta}(s)(s'^\alpha-s^\alpha)(s'^\beta-s^\beta)\big)^{3/2}}\sqrt{h(s)}\boldsymbol{n}(s)+O(|s-s'|^{-1})\,. \tag{2.2.25}$$

We can then integrate the leading order term in (2.2.25) and obtain an approximate (average) velocity along the interface; however, the resulting velocity field is difficult to write in terms of simple Fourier multipliers (which is our objective), and therefore maintains the computational expense of the original Birkhoff-Rott velocity. In order to derive a velocity field which takes advantage of the computational efficiency of Fourier multipliers, we must assume that the metric

h is isotropic, by which we mean that the components $h_{\alpha\beta}$ of the metric satisfy

$$h_{11} = h_{22}\,, \quad h_{12} = h_{21} = 0\,,$$

in which case

$$\frac{\sqrt{h(s)}\mu_\alpha(s')(s^\alpha - s'^\alpha)}{\big(h_{\alpha\beta}(s')(s'^\alpha - s^\alpha)(s'^\beta - s^\beta)\big)^{\frac{3}{2}}}\boldsymbol{n}(s) = \frac{\mu_\alpha(s')(s^\alpha - s'^\alpha)}{|h(s)|}\boldsymbol{n}(s)\,. \tag{2.2.26}$$

Replacing the original integrand in the Birkhoff-Rott integral (2.2.7) with the first-order term (2.2.26) in its expansion results in an approximate velocity $\widetilde{\boldsymbol{u}}$, computable in terms of *Riesz transforms* R^α:

$$\widetilde{\boldsymbol{u}} = \frac{R^\alpha\mu_\alpha}{2|h|}\boldsymbol{n}, \qquad R^\alpha f(s) = \frac{1}{2\pi}\iint\limits_{\mathbb{R}^2}\frac{(s^\alpha - s'^\alpha)f(s')}{|s-s'|^3}\mathrm{d}s'\,,\ \alpha = 1,2\,. \tag{2.2.27}$$

Riesz transforms are Fourier multipliers: $\widehat{R^\alpha f}(k) = -ik^\alpha\hat{f}(k)/|k|$, where $\hat{f}(k)$ denotes the Fourier transform of $f(x)$. These operators are the multi-dimensional generalization of the Hilbert transform used in the definition of the lower-order 2D z-model (2.2.19).

The first term of the Laurent series for $\boldsymbol{\omega}(s')\times(\boldsymbol{z}(s)-\boldsymbol{z}(s'))/|z(s)-z(s')|^3$ is given by (2.2.25) with an error which is $O(|s-s'|^{-1})$ as $s'\to s$. The $O(|s-s'|^{-1})$ term in this expansion is what remains in (2.2.24), and upon integration in s', produces a leading-order estimate for the error or *remainder* $\mathcal{R}$ between the lower order velocity $\widetilde{\boldsymbol{u}}$ and the full Birkhoff-Rott velocity $\bar{\boldsymbol{u}}$. Utilizing our isotropy assumption shows that

$$\begin{aligned}\mathcal{R} = \frac{\partial_\beta(\sqrt{h}\boldsymbol{n})R^\beta R^\alpha\mu_\alpha}{|h|^{3/2}} &- \frac{1}{2}\frac{h^{\gamma\delta}(\partial_{\alpha\beta}\boldsymbol{z}\cdot\partial_\gamma\boldsymbol{z})R^\beta R^\alpha\mu_\delta}{|h|^{3/2}}\boldsymbol{n}\\ &- \frac{1}{2}\frac{(\boldsymbol{n}\cdot\partial_{\alpha\beta}\boldsymbol{z})\big((\partial_1\boldsymbol{z}\times\boldsymbol{n})R^\alpha R^\beta\mu_2 - (\partial_2\boldsymbol{z}\times\boldsymbol{n})R^\alpha R^\beta\mu_1\big)}{|h|^{3/2}}\\ &- \frac{3}{2}\frac{(R^\alpha R^\beta R^\gamma R^\delta\mu_\alpha)(\partial_\beta\boldsymbol{z}\cdot\partial_{\gamma\delta}\boldsymbol{z})}{|h|^{5/2}}\boldsymbol{n}\,.\end{aligned} \tag{2.2.28}$$

Using the fact that the Riesz transforms have unit norm as bounded operators on L^2, Hölder's

inequality shows that

$$\left(\iint_{\mathbb{R}^2} \mathcal{R}(s)^2 ds\right)^{\frac{1}{2}} \leqslant C \left(\iint_{\mathbb{R}^2} |\mu(s)|_h^2 \mathrm{d}s\right)^{\frac{1}{2}} \sum_{\alpha,\beta=1}^{2} \sup_{s\in\mathbb{T}^2} \frac{|\partial_{\alpha\beta}\boldsymbol{z}|}{1+|h|}, \tag{2.2.29}$$

where $|\mu|_h^2 = h_{\alpha\beta}\mu^\alpha\mu^\beta$ is the magnitude of μ with respect to the metric h on $\Gamma(t)$. In more concise notation,

$$\|\mathcal{R}\|_{L^2} \leqslant \|\mu\|_{L^2} \left\| \frac{D^2 z}{|h|^{\frac{3}{2}}} \right\|_{L^\infty}. \tag{2.2.30}$$

Since the mean curvature vector on $\Gamma(t)$ is defined as

$$\kappa(s,t)\boldsymbol{n} = \frac{h^{\alpha\beta}}{\sqrt{h}} \partial_{\alpha\beta}\boldsymbol{z} \cdot (\partial_1 z \times \partial_2 \boldsymbol{z}),$$

the bound (2.2.30) becomes small when the mean curvature is very small, as $\|\mu\|_{L^2}$ remains bounded under this scenario.

Inserting $\widetilde{\boldsymbol{u}}$ into the Euler equations (2.2.17) in place of the Birkhoff-Rott velocity gets rid of the problematic time-derivative term $(\bar{\boldsymbol{u}} \cdot \partial_\alpha \boldsymbol{z})_t$, as $\widetilde{\boldsymbol{u}}$ is normal to $\Gamma(t)$, and so $\widetilde{\boldsymbol{u}} \cdot \partial_\alpha \boldsymbol{z} = 0$. This yields the following system of equations:

$$\partial_t \boldsymbol{z} = \widetilde{\boldsymbol{u}} \qquad 0 < t \leqslant T, \tag{2.2.31a}$$

$$\partial_t \mu_\alpha = A\partial_\alpha\left(|\widetilde{\boldsymbol{u}}|^2 - \tfrac{1}{4} h^{\beta\gamma}\mu_\beta\mu_\gamma - 2gz^3\right) \qquad 0 < t \leqslant T, \tag{2.2.31b}$$

$$\boldsymbol{z}(s,0) = \mathring{\boldsymbol{z}}(s), \quad \mu_\alpha(s,0) = \mathring{\mu}_\alpha(s), \tag{2.2.31c}$$

where $\mathring{\boldsymbol{z}}(s)$ and $\mathring{\mu}_\alpha(s)$ denote the initial conditions for the interface parameterization and vorticity, respectively. We refer to (2.2.31) as the *lower-order z-model*. It is an extremely efficient model, which tracks the interface accurately until about the time of turnover, after which it forms a sort of "envelope" for the roll-up in the near-symmetric regime (see Figure 2.1). This envelope behavior accurately captures the large-scale behavior of RTI for interfaces with small curvature and small anisotropy, although our medium- and higher-order z-models (which are introduced below) are better suited for capturing the small-scale structure of roll-up. In particular, the lower-order z-

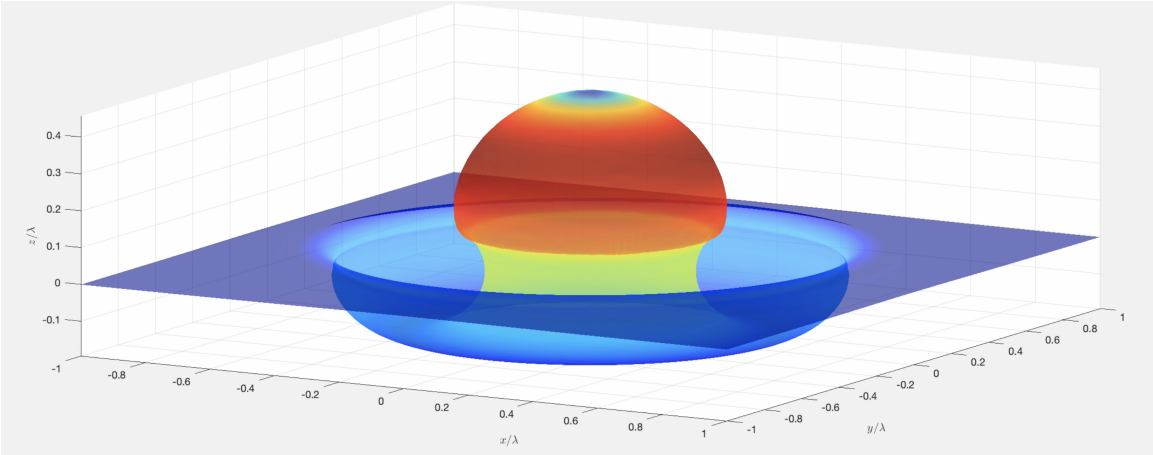


Figure 2.1: Evolution of the lower-order z-model, starting from a Gaussian perturbation of a flat interface, run on a 192×192 mesh in 18s.

model suppresses interactions between interface points which are close in space but distant in interface variables, i.e. where $|\boldsymbol{z}(s) - \boldsymbol{z}(s')| \ll |s - s'|$. This occurs precisely when the interface folds over or rolls up, which is why the model produces poorer results after interfce turnover. At a point of high curvature, where the interface folds over itself, the full Birkhoff-Rott velocity correctly gives a large velocity and causes the interface to roll-up further, whereas the lower-order velocity remains small.

We note that a convenient feature of the lower-order z-model (2.2.31) is that the velocity $\tilde{\boldsymbol{u}}$ is given by a Fourier multiplier. As such, the numerical implementation of (2.2.31) can take advantage of the Fast Fourier Transform which is both fast and easy to implement, and is one of advantages of this model in comparison to the higher-order models to be introduced next. The computational speed of the lower-order z-model creates an efficient and effective tool for determining large-scale features of RTI structures, such as interface growth rates and bubble and spike positions. On average, the lower-order z-model runs about 15,000 times faster than standard numerical schemes for 3D hydrodynamics (Reisner, 2020).

2.2.4 The 3D Medium-Order and Higher-Order z-Models

The isotropy assumption made in the derivation of the lower-order z-model is too restrictive for a large class of initial data. As such, we turn our attention to the medium-order z-model (2.2.32) and higher-order z-model (2.2.33). The medium-order z-model is obtained by replacing the localized

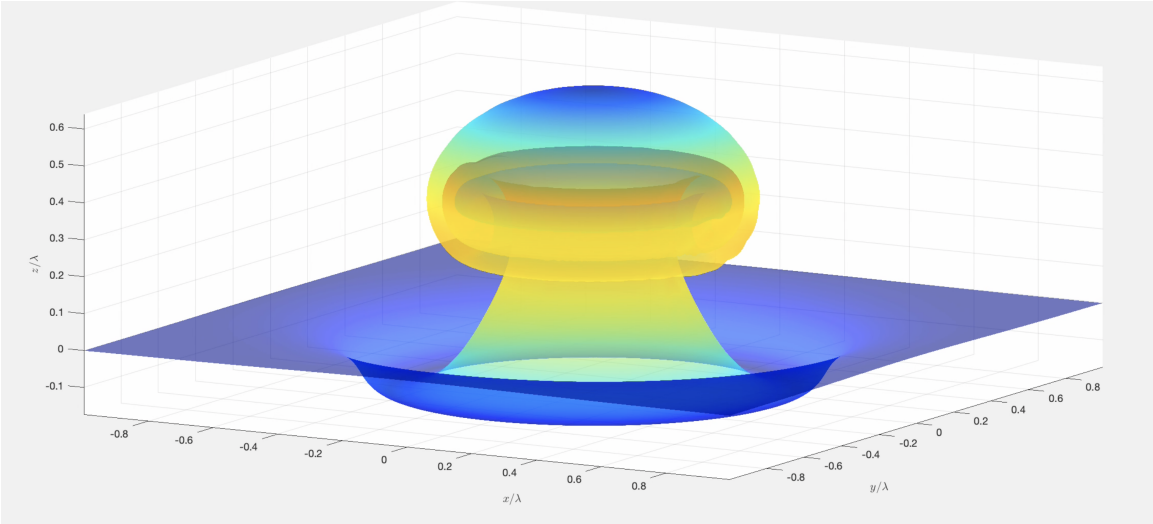


Figure 2.2: Evolution of the higher-order z-model, starting from a Gaussian perturbation of a flat interface, run on a 192×192 mesh in 420s. Note that the lower-order z-model (Figure 2.1) traces a sort of 'envelope' for the higher-order z-model.

velocity (2.2.27) with the regularized Birkhoff-Rott velocity (2.2.11) *only* in the z-evolution equation in (2.2.31a) while keeping the vorticity equation (2.2.31b) unchanged:

$$\partial_t \boldsymbol{z} = \bar{\boldsymbol{u}}^\epsilon \qquad 0 < t \leqslant T\,, \tag{2.2.32a}$$

$$\partial_t \mu_\alpha = A\partial_\alpha\big(|\tilde{\boldsymbol{u}}|^2 - \tfrac{1}{4}h^{\alpha\beta}\mu_\alpha\mu_\beta - 2gz^3\big) \qquad 0 < t \leqslant T\,, \tag{2.2.32b}$$

$$\boldsymbol{z}(s,0) = \mathring{\boldsymbol{z}}(s)\,, \quad \mu_\alpha(s,0) = \mathring{\mu}_\alpha(s)\,, \tag{2.2.32c}$$

For the higher-order z-model, we replace the localized velocity with the regularized Birkhoff-Rott velocity in both equations of (2.2.31) to obtain

$$\partial_t \boldsymbol{z} = \bar{\boldsymbol{u}}^\epsilon \qquad 0 < t \leqslant T\,, \tag{2.2.33a}$$

$$\partial_t \mu_\alpha = A\partial_\alpha\big(|\bar{\boldsymbol{u}}^\epsilon|^2 - \tfrac{1}{4}h^{\alpha\beta}\mu_\alpha\mu_\beta - 2gz^3\big) \qquad 0 < t \leqslant T\,, \tag{2.2.33b}$$

$$\boldsymbol{z}(s,0) = \mathring{\boldsymbol{z}}(s)\,, \quad \mu_\alpha(s,0) = \mathring{\mu}_\alpha(s)\,, \tag{2.2.33c}$$

The medium- and higher-order z-models are able to capture the fine-scale structures of RTI, including the Kelvin-Helmholtz roll-up regions (see Figure 2.2), but are more costly to simulate numerically than the lower-order z-model. Nevertheless, the medium- and higher-order z-models run 600 times faster than standard numerical methods for 3D gas dynamics codes (Reisner, 2020).

The evolution equations for the higher-order z-model differ from the integral form of the Euler equations by only one term. In particular, a comparison of the right-hand sides of (2.2.18b) with (2.2.33b) shows that the higher-order z-model does not have the problematic nonlinear and nonlocal time-derivative term $2A\partial_t(\bar{\boldsymbol{u}} \cdot \partial_\alpha \boldsymbol{z})$. As we will explain in Section 2.2.5, the reason that the higher-order z-model maintains accuracy is that this time-derivative term tends to be small. We note that for the numerical simulations we consider in this work, results from the medium-order z-model and the higher-order z-model are essentially indistinguishable (compare the first and second rows in Figure 2.10), but the higher-order z-model is more numerically stable. For this reason, we have chosen not to report results from the medium-order z-model (with the exception of the second row in Figure 2.10).

An important feature of Rayleigh-Taylor instability is the differing behavior of 'bubbles' of light fluid rising into the heavy fluid and 'spikes' of heavy fluid falling into the light fluid. Our model accurately captures this differing behavior with the spikes being thinner and slightly longer than the bubbles. Figure 2.3 shows the evolution of the initial conditions

$$z^1 = s^1, \qquad z^2 = s^2, \qquad z^3 = \pm 0.05 e^{-9|s|^2}, \qquad \mu_1 = \mu_2 = 0 \tag{2.2.34}$$

at two, three, and four characteristic times.

2.2.5 Dynamics of Vorticity

The relationship between the components of vorticity ω^α and the interface roll-up is quite straightforward. Each 'roll' of the interface corresponds to a sequence of successively stronger concentric 'ridges' in the magnitude of vorticity, and the vector field (ω^1, ω^2) circulates around these ridges. Figure 2.4 shows a simulation of the higher-order z-model (2.2.33) in which a single ring of vorticity (top row, pre-turnover) splits into two rings of vorticity, the inner ring stronger than the outer (bottom row, post-turnover). Figure 2.5 shows the corresponding magnitude of vorticity for the interfaces in Figure 2.4. These spikes in the vorticity are essential to the roll-up of the interface $\Gamma(t)$, but they are also a source of numerical instability. To mitigate this instability, we introduce a smooth, vorticity-scaled, nonlinear artificial viscosity, outlined in Section 2.3.1.

The lower-order z-model fails to roll-up because only one *sufficiently strong* ring of vorticity

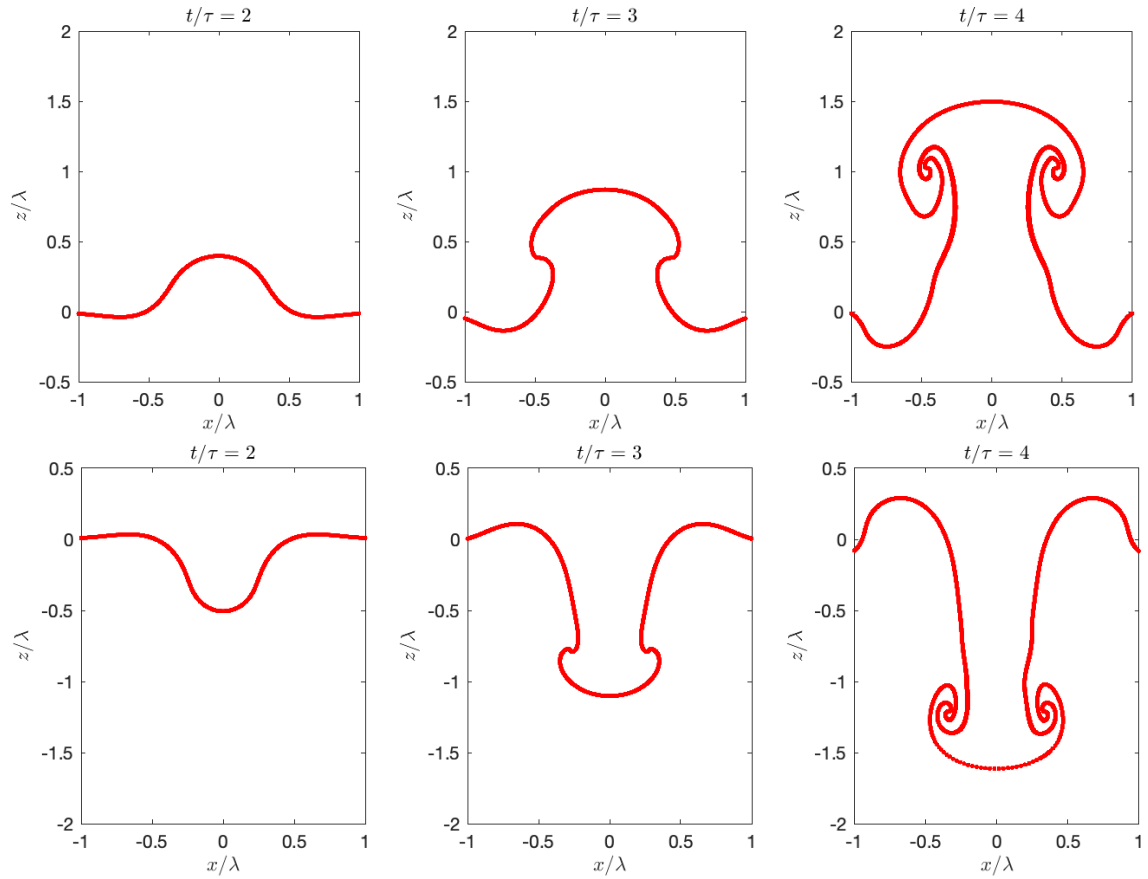


Figure 2.3: Cross-sections of the 3D higher-order z-model, run on a 64×64 grid, with Atwood number 0.7 and a runtime of 50s.

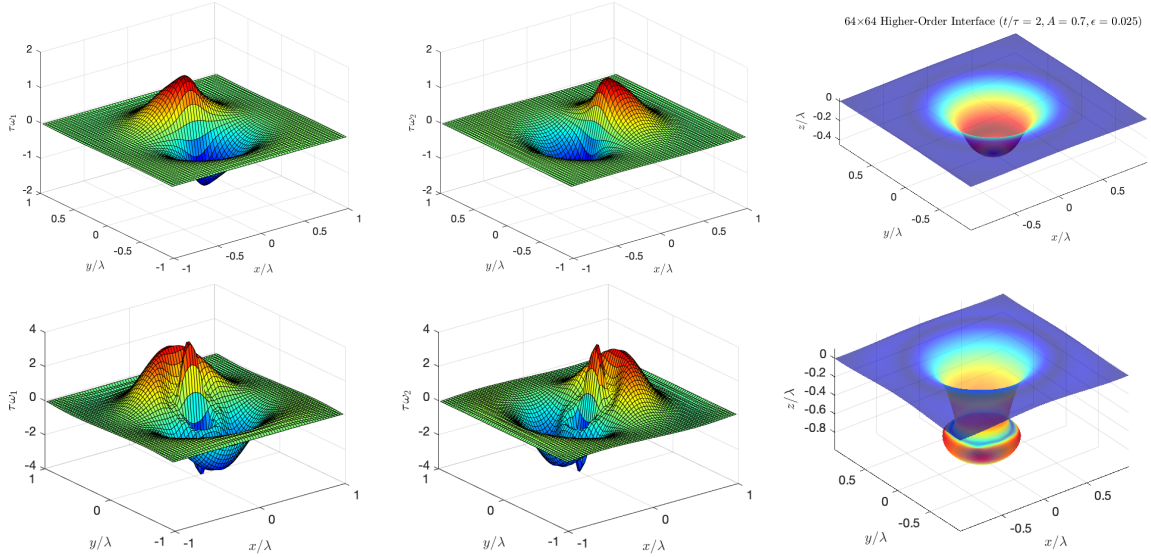


Figure 2.4: Nondimensionalized components of vorticity for the higher-order z-model, compared with the full interface. Color on the interface indicates magnitude of vorticity (red is higher, blue is lower).

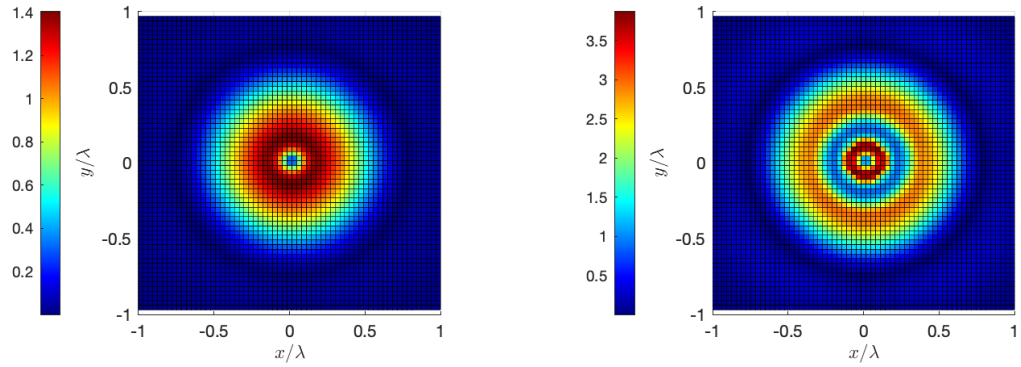


Figure 2.5: Heatmap of the nondimensionalized magnitude of vorticity for the two interfaces shown in Figure 2.4).

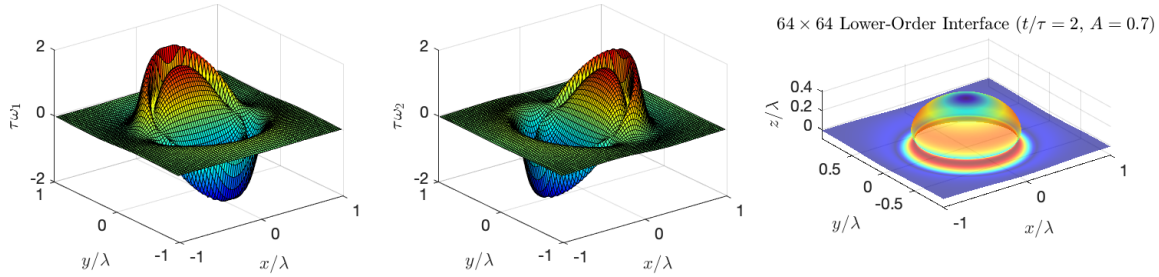


Figure 2.6: Nondimensionalized components of vorticity for the lower-order z-model, compared with the full interface. Color on the interface indicates magnitude of vorticity (red is higher, blue is lower).

can form during the entire evolution. A secondary (weaker) ring of vorticity may form inside the first, but its amplitude is too small to initiate secondary turnover. This weak secondary vorticity produced by the lower-order z-model is shown in Figure 2.6.

We can now provide a heuristic argument as to why the problematic time-derivative term $2A\partial_t(\bar{\boldsymbol{u}} \cdot \partial_\alpha \boldsymbol{z})$ on the right side of (2.2.18b) does not significantly alter the true dynamics, and thus allows for the higher-order z-model evolution to accurately simulate solutions of the Euler equations. Integrating (2.2.18b), we have that

$$\begin{aligned}\mu_\alpha(s,t) = \mathring{\mu}_\alpha(s) + A\int_0^t \partial_\alpha\big(|\bar{\boldsymbol{u}}|^2 - \tfrac{1}{4}h^{\beta\gamma}\mu_\beta\mu_\gamma - 2gz^3\big)\mathrm{d}t' \\ + 2A\big(\bar{\boldsymbol{u}}^\epsilon(s,0)\cdot\partial_\alpha\mathring{z}(s) - \bar{\boldsymbol{u}}(s,t)\cdot\partial_\alpha\boldsymbol{z}(s,t)\big)\,. \qquad (2.2.35)\end{aligned}$$

From (2.2.25) and the definition of $\bar{\boldsymbol{u}}$ given in (2.2.10), we see that for $\alpha = 1, 2$,

$$\bar{\boldsymbol{u}}\cdot\partial_\alpha\boldsymbol{z} = \iint_{\mathbb{R}^2} \frac{(s^\nu - s'^\nu)(s^\beta - s'^\beta)}{|s-s'|^3}\Big(\mu_\nu(s')\sqrt{h}\partial_\beta\boldsymbol{n} - \tfrac{1}{2}(\mu_2(s')\partial_1\boldsymbol{z}$$

$$
\begin{aligned}
&\qquad\qquad - \mu_1(s')\partial_1 \boldsymbol{z}) \times \boldsymbol{n}(\partial_{\nu\beta} z \cdot n)\Big) \cdot \partial_\alpha \boldsymbol{z} \mathrm{d}s' \\
&= -\iint_{\mathbb{R}^2} \frac{(s^\nu - s'^\nu)(s^\beta - s'^\beta)}{|s-s'|^3} \Big(\mu_\nu(s') h^{\delta\nu} \partial_\delta z \\
&\qquad\qquad + \tfrac{1}{2}(\mu_2(s')\partial_1 \boldsymbol{z} - \mu_1(s')\partial_1 \boldsymbol{z}) \times n \Big) \cdot \partial_\alpha \boldsymbol{z}\ (\partial_{\nu\beta} \boldsymbol{z} \cdot \boldsymbol{n}) \mathrm{d}s',
\end{aligned}
$$

where we have used the identity

$$
\partial_\beta \boldsymbol{n} = -h^{\delta\nu}(\partial_{\nu\beta} z \cdot \boldsymbol{n}) \partial_\delta \boldsymbol{z}\,,
$$

and the fact that

$$
|s-s'|^3 = \left(h_{\nu\beta}(s)(s^\nu - s'^\nu)(s^\beta - s'^\beta)\right)^{\frac{3}{2}}.
$$

Since the inner-product of the first-order term in (2.2.25) with $\partial_\alpha \boldsymbol{z}$ vanishes,

$$
\frac{(s^\nu - s'^\nu)}{|s-s'|^3} \mu_\nu(s') \sqrt{h(s)} \boldsymbol{n}(s) \cdot \partial_\alpha \boldsymbol{z} = 0\,,
$$

the second-order correction is thus given by

$$
\frac{(s^\nu - s'^\nu)}{|s-s'|^3}(s^\beta - s'^\beta)\Big(\mu_\nu(s') h^{\delta\nu} \partial_\delta \boldsymbol{z} + \tfrac{1}{2}(\mu_2(s')\partial_1 \boldsymbol{z} - \mu_1(s')\partial_1 \boldsymbol{z}) \times \boldsymbol{n}\Big) \cdot \partial_\alpha \boldsymbol{z}\ (\partial_{\nu\beta} \boldsymbol{z} \cdot \boldsymbol{n})\,. \tag{2.2.36}
$$

Now, either the curvature of $\Gamma(t)$ is small in which case $\partial_{\nu\beta} \boldsymbol{z} \cdot \boldsymbol{n}$ is small and hence $\bar{\boldsymbol{u}} \cdot \partial_\alpha \boldsymbol{z}$ is small, or the curvature is large, in which case the vorticity measure forms highly concentrated peaks (as seen in Figure 2.4), in which the support of the peaks, which is a good approximation for $|s^\beta - s'^\beta|$, is very small. Hence, we see from (2.2.36) that either small curvature or strongly concentrated vorticity peaks produces small tangential velocity components.

2.3 Numerical Simulation and Validation against Experiments

In this section we describe the numerical method for solving the z-models, simulate a variety of classical test problems in the Rayleigh-Taylor instability, and validate our higher-order z-model to against experimental data of single-mode and random multi-mode RTI.

2.3.1 Numerical Approximation of the z-Model

The boundary integral formulation of the Euler equations, relying on a parametrization of the material interface, has several attractive features for simulating RTI. It is naturally adaptive, concentrating grid points near regions of physical interest, it avoids the numerical diffusion of grid-based methods, and it involves fewer independent variables. However, these benefits come at a significant computational cost, due to the nonlinear and nonlocal form of the time derivatives in this formulation. The use of standard time-stepping algorithms for evolution equations in which the time-derivatives are linear and isolated cannot be used. Rather, simulating such equations requires either the solution of a nonlinear Fredholm integral equation of the second kind for the time-derivatives, or the use of an iterative predictor-corrector method to evolve forward in time. Additionally, because the nonlocal expression requires $O(N^2)$ operation to evaluate (where N is the number of interface points), such predictor-corrector methods extremely expensive. The higher-order z-model has nearly all the aforementioned benefits of the full Euler equations in boundary integral form, and can be solved numerically with straightforward finite differencing in space and Runge-Kutta integration in time, with only a small cost in accuracy (see Section 2.2.5).

Geometric complexity is an essential feature of RTI, especially in three space dimensions, so accurately simulating such behavior requires maintaining a sharp discontinuity in density across the interface, while at the same time faithfully representing the interface geometry at a subgrid scale. The rectangular cells of Eulerian differencing schemes are ill-suited to the highly curved geometry of RTI problems, and often introduce spurious KHI spirals which obscure the form of the primary instability. Indeed, a look at the bewildering variety of behaviors observed in the excellent comparative study of Liska and Wendroff (2003) demonstrates that high-order methods such as WENO and PPM, set on structured Cartesian meshes, can be susceptible to spurious small-scale KHI. Nonetheless, for problems which must take into account many physical effects, such as compressibility, thermodynamics, combustion, or electromagnetism, methods such as these provide the best available numerical methods. See Zhou et al. (2021) §5-6 for a recent overview of numerical approaches to RTI. Methods such as marker-and-cell (Daly, 1967) and volume-of-fluid (Hirt and Nichols, 1981) use either marker particles or a marker function in addition to an Eulerian grid to track the interface. Similarly, front-tracking methods, which use a triangular mesh that

advects with the fluid velocity, have shown considerable success (Unverdi and Tryggvason, 1992; Glimm et al., 1998).

We now describe our numerical method for the z-models. All computations are set on a uniform spatial grid $\{(i\delta, j\delta) : i, j = -n, \ldots, n-1, n\}$, and the dynamical variables are stored as matrices of values on this grid, e.g.,

$$\boldsymbol{z}_{ij}(t) = \boldsymbol{z}(i\delta, j\delta, t), \qquad\qquad i, j = -n, \ldots, n-1, n.$$

Spatial derivatives are computed using fourth-order centered-difference operators $(\boldsymbol{D}_1, \boldsymbol{D}_2)$. These are used to compute the discretized form of the normal vector $\boldsymbol{N} = (\boldsymbol{D}_1\boldsymbol{z}) \times (\boldsymbol{D}_2\boldsymbol{z})$ and the metric determinant $|h| = |\boldsymbol{N}|^2$.

For the lower-order z-model, we compute $\widetilde{\boldsymbol{u}}$ via the fast Fourier transform:

$$\widetilde{\boldsymbol{u}}_{jk} = \mathscr{F}^{-1}\left(\frac{\mathrm{i}l(\mathscr{F}\mu_1)_{lm} + \mathrm{i}m(\mathscr{F}\mu_2)_{lm}}{(l^2+m^2)^{1/2}}\right)_{jk} \frac{\boldsymbol{N}_{jk}}{|h|_{jk}^{3/2}}\,.$$

This still leaves $(\mathscr{F}\widetilde{\boldsymbol{u}})_{00}$ undefined, so we set it to zero. To mitigate the large spikes in vorticity discussed in Section 2.2.5, we introduce a nonlinear artificial viscosity operator $\nu\boldsymbol{\nabla}\cdot\left(c\boldsymbol{\nabla}/\sup c\right)$ on the right side of the vorticity equations, where

$$c = (1 - \nu\delta^2\Delta)^{-1}|\boldsymbol{\omega}|\,,$$

where δ is the grid size and $\nu > 0$ denote the artificial viscosity parameter. The function c is a smoothed version of the magnitude of vorticity $|\boldsymbol{\omega}|$, which provides a smooth localization for the addition of nonlinear artificial viscosity, motivated by the nonlinear (space-time smooth) artificial viscosity method introduced in Reisner et al. (2013) and utilized in Ramani et al. (2019a,b) but employing an elliptic solver at each time-step rather than the solution of a parabolic reaction-diffusion equation. This yields the following set of ODEs for the discretized lower-order z-model:

$$\begin{aligned}
\frac{\mathrm{d}\boldsymbol{z}_{jk}}{\mathrm{d}t} &= \widetilde{\boldsymbol{u}}_{jk}\,,\\
\frac{\mathrm{d}\mu_{jk}}{\mathrm{d}t} &= A\left[\begin{pmatrix}\boldsymbol{D}_1\\ \boldsymbol{D}_2\end{pmatrix}\left(|\widetilde{\boldsymbol{u}}|^2 - \tfrac{1}{4}h^{\alpha\beta}\mu_\alpha\mu_\beta - 2gz^3\right)\right]_{jk} + \nu\left[\sum_{\alpha=1}^{2}\boldsymbol{D}_\alpha\left(\frac{c\boldsymbol{D}_\alpha\mu}{\sup c}\right)\right]_{jk},
\end{aligned}$$

which are solved using a total variation decreasing (TVD) third-order Runge-Kutta method in time. For a generic system of ODEs $d\boldsymbol{x}/dt = \boldsymbol{f}(\boldsymbol{x}, t)$, the three-step Runge-Kutta method we use to advance the solution from $\boldsymbol{x}_n = \boldsymbol{x}(t)$ to $\boldsymbol{x}_{n+1} = \boldsymbol{x}(t + \Delta t)$ is given by

$$\begin{aligned}
\boldsymbol{k}_1 &= \boldsymbol{x}_n + \Delta t \boldsymbol{f}(\boldsymbol{x}_n, t) \\
\boldsymbol{k}_2 &= \frac{3}{4}\boldsymbol{x}_n + \frac{1}{4}\boldsymbol{k}_1 + \frac{\Delta t}{4}\boldsymbol{f}(\boldsymbol{k}_1, t) \\
\boldsymbol{x}_{n+1} &= \frac{1}{3}\boldsymbol{x}_n + \frac{2}{3}\boldsymbol{k}_2 + \frac{2\Delta t}{3}\boldsymbol{f}\left(\boldsymbol{k}_2, t + \tfrac{1}{2}\Delta t\right)
\end{aligned}$$

For both the medium and higher-order z-models, we compute the Birkhoff-Rott velocity $\bar{\boldsymbol{u}}$ using a Simpson's rule quadrature, which has the form

$$\bar{\boldsymbol{u}}^{\epsilon}_{ij} = \tfrac{1}{4\pi}\sum_k\sum_l M_{kl}\boldsymbol{\omega}_{kl} \times \frac{\boldsymbol{z}_{ij} - \boldsymbol{z}_{kl}}{(\epsilon^2 + |\boldsymbol{z}_{ij} - \boldsymbol{z}_{kl}|^2)^{3/2}}, \qquad \boldsymbol{\omega}_{kl} = \left(\mu_{2,kl}(\boldsymbol{D}_1\boldsymbol{z})_{kl} - \mu_{1,kl}(\boldsymbol{D}_2\boldsymbol{z})_{kl}\right),$$

for some matrix of weights $\boldsymbol{M} = (M_{ij})$. The discretized medium-order z-model is given by

$$\begin{aligned}
\frac{\mathrm{d}\boldsymbol{z}_{jk}}{\mathrm{d}t} &= \bar{\boldsymbol{u}}^{\epsilon}_{jk}, \\
\frac{\mathrm{d}\mu_{jk}}{\mathrm{d}t} &= A\left[\begin{pmatrix}\boldsymbol{D}_1\\ \boldsymbol{D}_2\end{pmatrix}\left(|\tilde{\boldsymbol{u}}|^2 - \tfrac{1}{4}h^{\alpha\beta}\mu_\alpha\mu_\beta - 2gz^3\right)\right]_{jk} + \nu\left[\sum_{\alpha=1}^{2}\boldsymbol{D}_\alpha\left(\frac{c\boldsymbol{D}_\alpha\mu}{\sup c}\right)\right]_{jk},
\end{aligned}$$

and the discretized higher-order z-model is

$$\begin{aligned}
\frac{\mathrm{d}z_{jk}}{\mathrm{d}t} &= \bar{\boldsymbol{u}}^{\epsilon}_{jk}, \\
\frac{\mathrm{d}\mu_{jk}}{\mathrm{d}t} &= A\left[\begin{pmatrix}\boldsymbol{D}_1\\ \boldsymbol{D}_2\end{pmatrix}\left(|\bar{\boldsymbol{u}}^{\epsilon}|^2 - \tfrac{1}{4}h^{\alpha\beta}\mu_\alpha\mu_\beta - 2gz^3\right)\right]_{jk} + \nu\left[\sum_{\alpha=1}^{2}\boldsymbol{D}_\alpha\left(\frac{c\boldsymbol{D}_\alpha\mu}{\sup c}\right)\right]_{jk}.
\end{aligned}$$

The time required for the computation of the Birkhoff-Rott velocity $\bar{\boldsymbol{u}}$ can be drastically shortened with the use of the fast multipole method. Evaluating $\bar{\boldsymbol{u}}^{\epsilon}_{jk}$ for all j and k requires $O(N^2)$ operations, where $N = (2n+1)^2$ is the total number of grid points in the simulation. In contrast, the fast multipole method evaluates in $O(N)$ operations, given a fixed relative accuracy goal. As shown in Figure 2.7, we have verified this performance for interface grid resolutions up to size

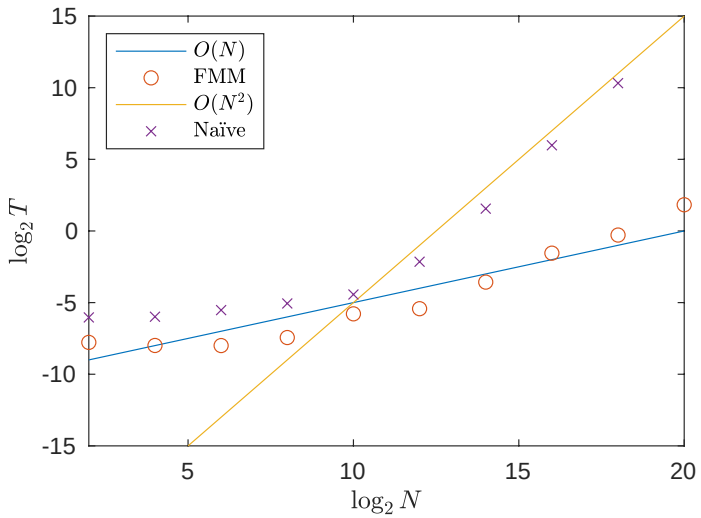


Figure 2.7: Measured computation times for the Birkhoff-Rott velocity.

$N = 1024 \times 1024$ using the open-source package `fmm3d`.[1]

2.3.2 Convergence of the z-Model

We note that existence of solutions to the incompressible Euler equations with general vortex sheet initial data is not known, and for certain types of vortex sheet data for which weak solutions can be constructed, such solutions are not unique (see, for example Székelyhidi, 2011). As such different regularizations of the Euler equations will lead to sequences of approximate solutions which, such that if these sequences converge, they may not all converge to the same solution. Sequences of approximate Euler solutions, obtained by using a regularized Birkhoff-Rott velocity, have been shown to converge to (possibly non-unique) solutions of the Euler equations in, for example, Beale and Majda (1982); Liu and Xin (1995, 2001). In particular, numerical simulations suggest that the limiting weak solution depends upon the choice of the velocity regularization (see Baker and Pham, 2006; Lopes-Filho et al., 2006; Ramani and Shkoller, 2020).

On the other hand, as was shown in Ramani and Shkoller (2020, Figures 8-10), the 2D z-model exhibits convergence of large-scale averaged quantities such as the spiral roll-up center, the roll-up radius, the location of the bubble and spike tips, and the bubble and spike amplitudes. It is likely that such convergence of large-scale features is independent of the numerical approximation

[1] https://github.com/flatironinstitute/FMM3D

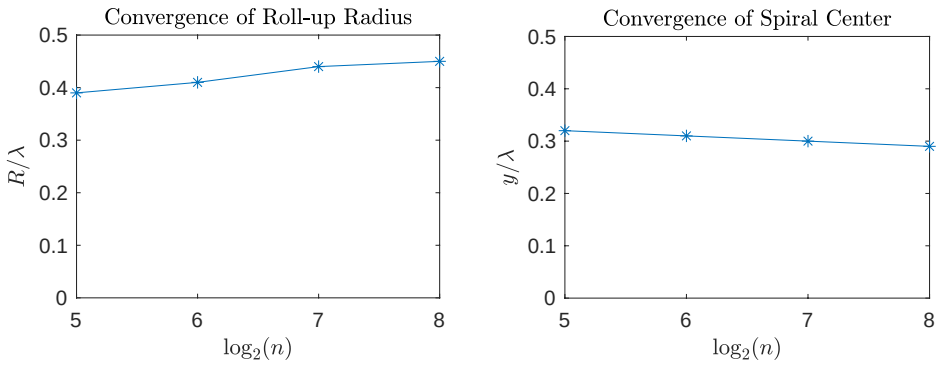


Figure 2.8: Convergence of roll-up radius and spiral centers for the 3D higher-order z-model, as the mesh is refined.

employed, and in this section we show that the 3D higher-order z-model converges in this large-scale sense, in the limit as the desingularization and mesh spacing are taken to zero simultaneously.

Figure 2.8 demonstrates this large-scale convergence for the 3D higher-order z-model , using the initial data 2.2.34. As can be seen, there is convergence of the roll-up radius and the location of the spiral centers on a sequence of $n \times n$ meshes with $n = 32, 64, 128, 256$, and with regularization parameter ϵ proportional to the mesh size.

2.3.3 Single-Mode Initial Data

Sinusoidal perturbations of a flat interface were the first to be studied in the context of RTI, and much of the analytical and experimental study of RTI has focused on understanding the evolution of single-mode initial data beyond the linear regime (see, for instance, Emmons et al., 1960; Cole and Tankin, 1973; Baker et al., 1984; Goncharov, 2002). Of course, in most application scenarios, the interface is perturbed with many different frequencies, but to understand the single-mode problem is the first step towards understanding the more general problem.

For our first test, we use our higher-order z-model to simulate Wilkinson/Jacobs' isopropyl alcohol/water experiment ($A = 0.15$). We initialize our z-model with initial conditions of the form

$$z^1 = s^1, \quad z^2 = s^2, \quad z^3 = a_0 \cos(\pi k s^1/\lambda) \cos(\pi k s^2/\lambda), \quad \mu_1 = \mu_2 = 0, \tag{2.3.1}$$

where $-\lambda \leqslant s^1, s^2 \leqslant \lambda$ and k is a positive integer. We may regard λ as a characteristic length for this problem, and the corresponding characteristic time scale is given by $\tau = (\lambda/Ag)^{1/2}$. This type

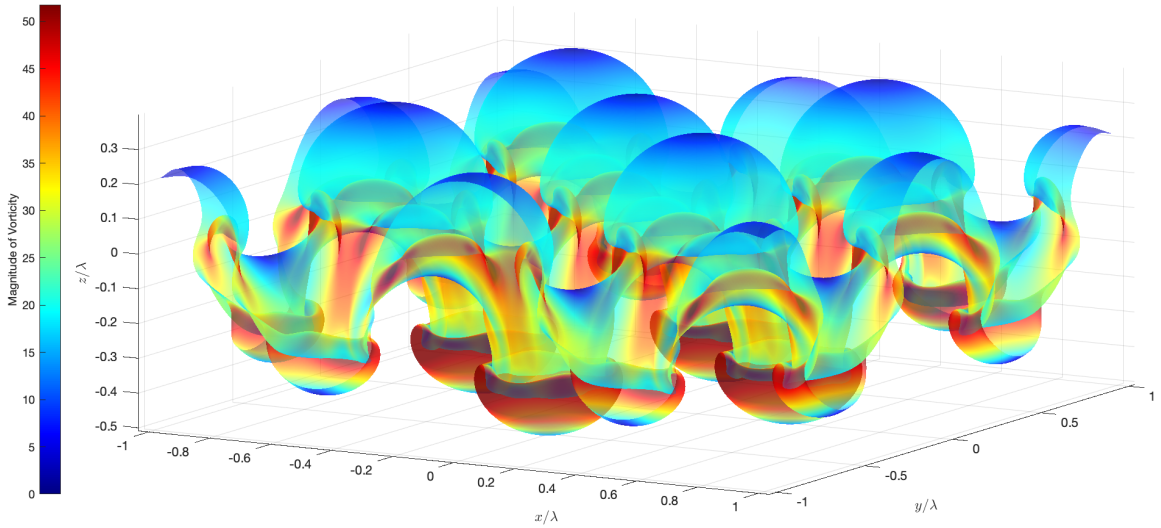


Figure 2.9: Single-mode initial data with two wavelengths along each side of the tank, run using the higher-order z-model on a 192×192 grid, with Atwood number 0.15 and a computation time of 380s.

of initial data was studied experimentally by Wilkinson and Jacobs, who used planar laser-induced fluorescence (PLIF) to visualize a diagonal cross-section of the fluid as it evolved, showing the *double roll-up* which distinguishes 3D Rayleigh-Taylor instability from 2D (Wilkinson and Jacobs, 2007). Results for the case $k = 2$ are shown in Figure 2.9.

Starting from a single-mode perturbation of a flat interface, 3D RTI forms a periodic pattern of bubbles and spikes in such a way that *two* vortices form on the side of each bubble or spike. In 2D, single-mode RTI produces a stationary row of counter-rotating vortices, which manifests as a single row of roll-up regions. However, in 3D, single-mode RTI produces two grids of counter-rotating vortex *rings*, which move apart from each other at roughly constant speed. Upon taking a cross-section along the diagonal of the tank, we obtain the double-spiral pattern seen here. See Chapman and Jacobs (2006) Figures 8 and 16 for a helpful illustration of single vs. double roll-up regions.

Using the parameters from their experiments and matching the wavelength of the initial data as best we could, we were able to achieve remarkably good agreement between our higher- and medium-order z-models and their experimental data – see Figure 2.10. As shown in Figure 2.11, the lower-order z-model matches the experiments quite well at early times. At later times, however, the lower-order z-model cannot capture the full extent of the roll-up, as discussed in Section 2.2.5.

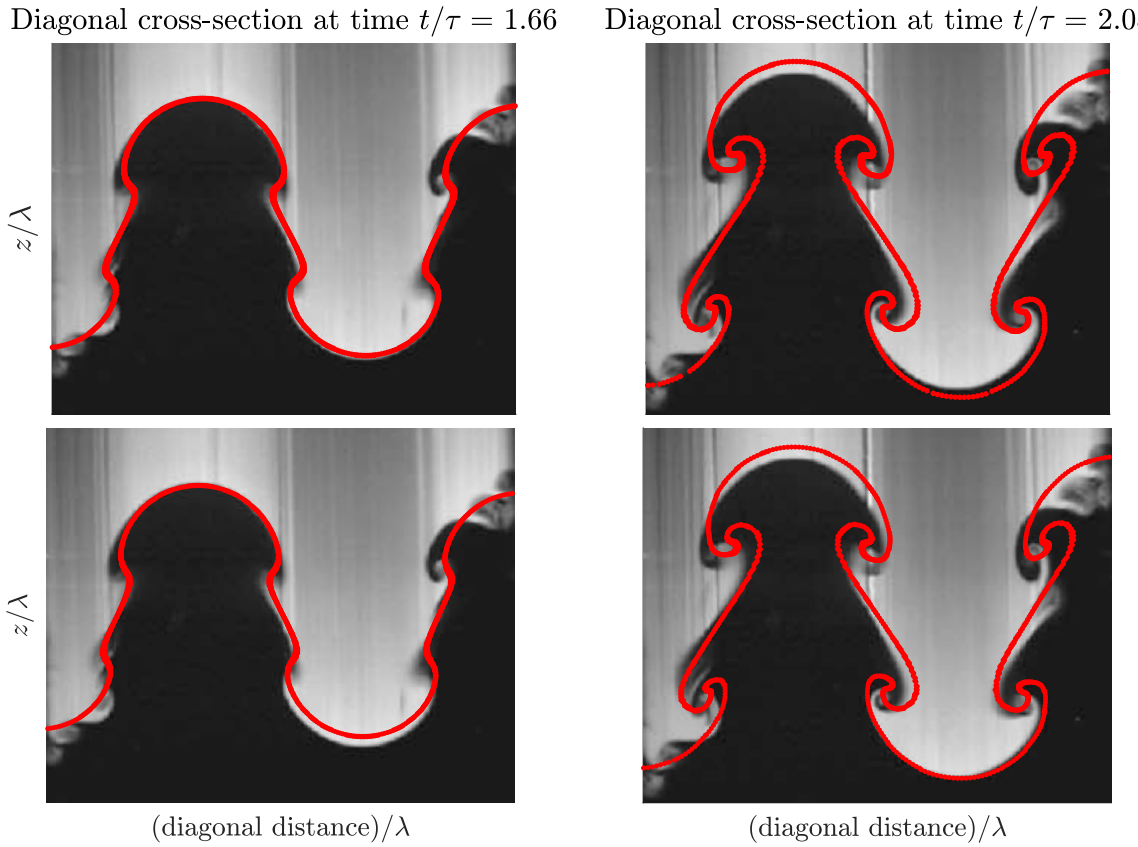


Figure 2.10: *Top:* Higher-order z-model. *Bottom:* Medium-order z-model. Both were run on 160×160 meshes, with Atwood number 0.15 and a runtime of 270s. Experimental photographs from Wilkinson and Jacobs (2007). Copyright 2007, AIP Publishing. Reproduced with permission.

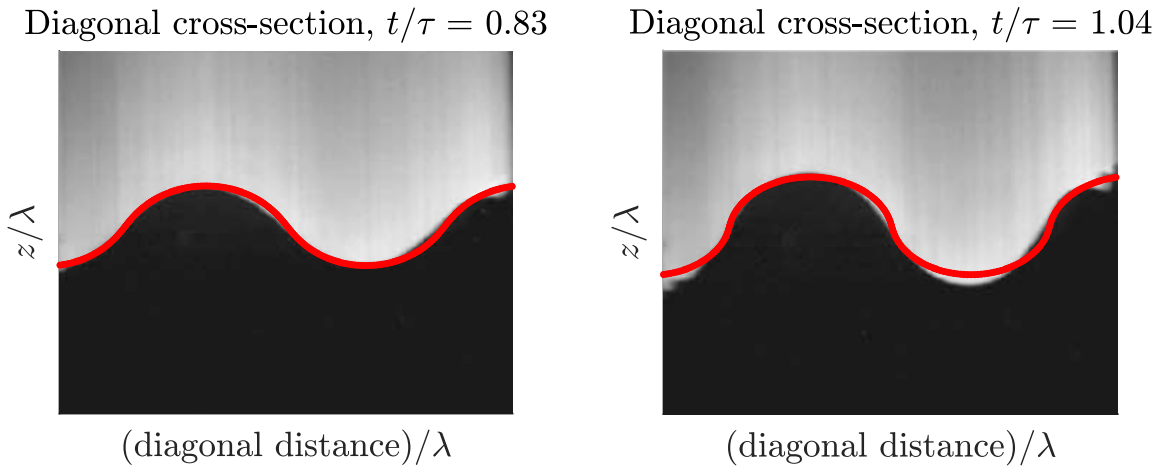


Figure 2.11: Lower-order z-model, run on a 130×130 grid, with Atwood number 0.15 and a runtime of 9s. Experimental photographs from Wilkinson and Jacobs (2007). Copyright 2007, AIP Publishing. Reproduced with permission.

The amplitude of 3D single-mode Rayleigh-Taylor instability initially follows the exponential growth rate $a \sim \cosh(\sqrt{Agk}t)$ predicted by the linear theory, before slowing to approximately constant velocity. The single-mode model of Goncharov (2002) predicts asymptotic bubble and spike velocities of

$$U_b = \sqrt{\frac{2Ag}{(1+A)k}}, \qquad U_s = \sqrt{\frac{2Ag}{(1-A)k}},$$

respectively, where k is the wavenumber of the initial perturbation. However, an asymptotically constant velocity has been called into question by numerical calculations of Ramaprabhu et al. (2006). Nonetheless, the single-mode experiments of Wilkinson and Jacobs (2007) show a period of linear growth in amplitude near Goncharov's predicted value, before accelerating once again. In Figure 2.12 we have plotted the Froude number (non-dimensional bubble velocity) for the bubbles and spikes in our single-mode experiments,

$$\mathrm{Fr}_b = \frac{\dot{a}_b}{\sqrt{\pi}U_b}, \qquad \mathrm{Fr}_s = \frac{\dot{a}_s}{\sqrt{\pi}U_s}$$

against the normalized bubble and spike amplitudes a_b and a_s. Although our simulations do not run for as long as Wilkinson and Jacobs' experiments, the Froude numbers are in agreement with the experimental results for the simulated range of amplitudes, showing an increase to slightly above the predicted asymptotic value $\mathrm{Fr} \sim \pi^{-1/2}$ (compare our Figure 2.12 with Figures 15-17 in Wilkinson and Jacobs, 2007).

2.3.4 The 3D Rocket Rig Experiment

The growth rate of the mixing layer between two fluids subjected to random multi-mode perturbations has been the subject of significant interest and study, and it forms a useful benchmark for our z-models. Starting with a small perturbation of amplitude h_0 of a flat interface, theory predicts that the amplitude $h(t)$ of the resulting mixing layer has the form

$$\frac{h - h_0}{\lambda} = \alpha \left(\frac{t}{\tau}\right)^2,$$

where α is a universal growth rate constant. The growth rate of the interface was tested experimentally by Read (1984) and Youngs (1989), and numerically by Youngs (1984, 1989). Their

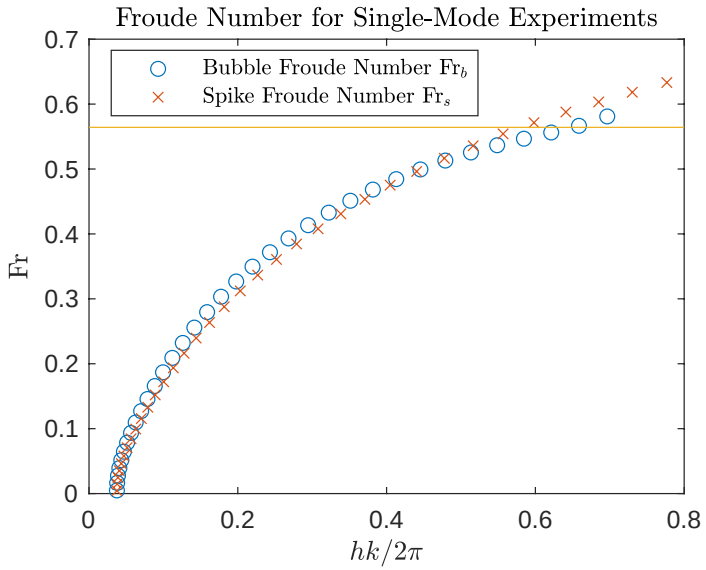


Figure 2.12: Plot of bubble and spike Froude numbers against normalized amplitude for our single-mode RTI simulations. Horizontal line shows asymptotic prediction Fr $\sim \pi^{-1/2}$. Compare with Figs 15 and 16 in Wilkinson and Jacobs (2007).

experimental setup consists of a $150 \times 150\text{mm}^2$ tank on a vertical sled, accelerated downward using rocket motors, which gives this experimental setup the nickname "rocket rig". Read's results suggest that α is between 0.06 and 0.07, although individual experiments have given values as low as 0.058 and as high as 0.077. To test the higher-order z-model in this scenario, we simulate Read's experiment using sodium iodide (NaI) solution ($\rho^+ = 1.9$ g/cm^3) and pentane ($\rho^- = 0.63$ g/cm^3) , which results in an Atwood number $A \approx 0.5$. More recently, Ristorcelli and Clark (2004) and Cook et al. (2004) independently discovered a new governing equation for the mixing layer amplitude,

$$\dot{h}^2 = C_0 A g h.$$

At large times, the solution to this ODE grows like $h \sim \frac{1}{4} C_0 t^2$, so that $C_0 = 4\alpha$. However, it was found by Cabot and Cook (2006) that the ratio $\dot{h}^2/4Agh$ approaches α only at very long times (around $t =$ 6-7τ, more than double the runtime of the experiments of Read and Youngs). The numerical experiments of Cabot and Cook (2006) ran until $t = 30\tau$, or more than eleven times the runtime of Read's experiments, and found that α stabilized at a value around 0.025. Our numerical experiments were run only for the length of Read's experiments, but the timeseries plot of $\dot{h}^2/4Agh$ from our experiments matched that of Cabot & Cook for the length of our experiments.

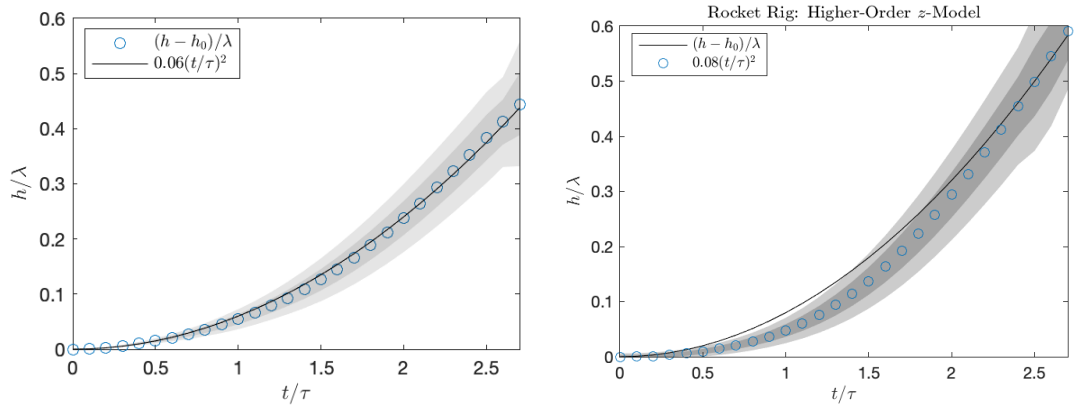


Figure 2.13: Comparison of higher-order z-model with theoretical growth rate, Case A (*Left*) and Case B (*Right*). The markers show the amplitude growth of the interface, averaged over 100 randomly initialized runs, and the gray bands show one and two standard deviations.

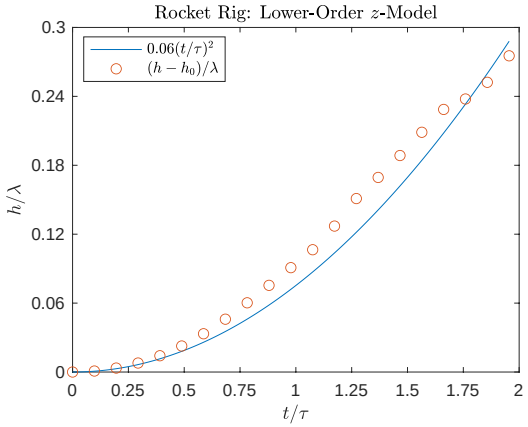


Figure 2.14: Comparison of lower-order z-model with theoretical growth rate, initialized in Case B.

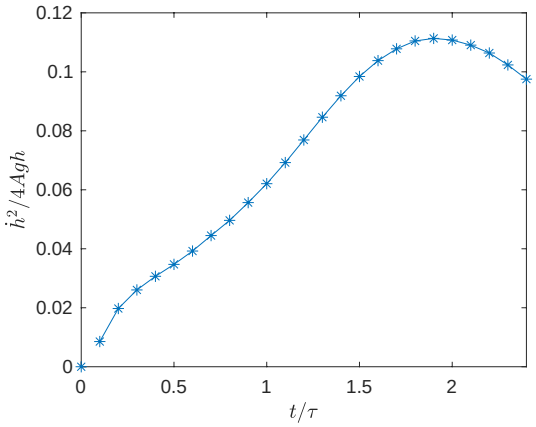


Figure 2.15: Plot of the time-dependent growth rate $\dot{h}^2/4Agh$, averaged over 100 rocket rig runs.

In this article we have simulated the rocket rig using parameter values from Read's NaI/Pentane experiment. Two main strategies are possible to initialize the rocket rig for numerical simulations, representing two distinct regimes of instability. The first strategy, Case A, is to initialize the instability with a random combination of short-wavelength perturbations, and allow larger scale disturbances to develop from the nonlinear interaction of the short-wavelength perturbations. The second strategy, Case B, is for long-wavelength perturbations to be present in the initial condition, causing the mixing layer to grow more rapidly at early times. See Youngs (2013) for a more detailed discussion and comparison of the different initialization strategies for the rocket rig. In Case A, we initialize our model with a random perturbation of a flat interface, of the form

$$z_1 = s_1, \qquad z_2 = s_2, \qquad z_3 = A_0 \mathrm{Re} \sum_{j_1=-n}^{n} \sum_{j_2=-n}^{n} a_{j_1,j_2} e^{\mathrm{i}(j_1 s_1 + j_2 s_2)}$$

where the complex coefficients $a_{\boldsymbol{j}} = a_{j_1,j_2}$ are drawn from a standard normal distribution when $|\boldsymbol{j}| > n/2$ and zero otherwise, and A_0 is chosen so that $(\iint |z_3(s,0)|^2 \mathrm{d}s)^{1/2} = 0.05$. In Case B, we instead draw the coefficients $a_{\boldsymbol{j}}$ from a normal distribution with variance $\sigma^2(\boldsymbol{j}) \propto |\boldsymbol{j}|^{-3}$.

Figure 2.13 shows results from 100 simulations of the higher-order z-model, using high-frequency initial perturbations (Case A, left panel) or the 'enhanced mixing' nonuniform variance (Case B, right panel). Both the experiment and the simulation were run for 67.4ms, or 2.7τ. The Case A runs show excellent agreement with the value $\alpha = 0.06$ suggested by Read's experiments. The computation time was 100s/run, using 100×100 meshes. The lower-order model does reasonably

well also, but the rate of interface growth slows after about two characteristic times, because the lower order z-model is not able to fully capture interface roll-up. This is shown in Figure 2.14. All models achieve growth rates around the range found in Read's experiments ($0.058 \leqslant \alpha \leqslant 0.077$). We note that although our simulations do not run long enough to see the stabilization of growth rate $\dot{h}^2/4Agh \sim \alpha$, they qualitatively match the plot of $\dot{h}^2/4Agh$ shown in Cabot & Cook up to the runtime of our simulation, showing an increase up to a peak of about 0.1 followed by steady decrease (compare Figure 2.15 to Cabot and Cook, 2006, Figure 4). To our knowledge, these are the first interface models which can accurately reproduce the growth rate of disordered RT mixing layers.

2.3.5 Fluid mixing in the Rocket Rig experiment

In addition to measuring the growth rate of the mixing layer, the speed of our high-order z-model simulations makes it feasible to compute ensemble averages of density for randomized initial data as shown in Figure 2.16 for the case of an ensemble of 100 runs. When computing ensembles using the invariant (Gibbs) measure associated to the Euler equations, it is known (Albeverio and Cruzeiro, 1990) that ensemble averaging of runs with data using (Gaussian) random frequency fluctuations of the interface produce viscous effects (whose size is inversely proportional to the frequency of perturbation). Such viscous effects can be computed from a uniform ensemble[2] of runs, and our results for such ensembles (see Figure 2.16) is in good agreement with traditional simulations of RTI using the Navier-Stokes equations.

The horizontally-averaged density as a function of the vertical coordinate and time, which we will denote $\bar{\rho}(z,t)$, is a useful measurement of the large-scale phenomenology of Rayleigh-Taylor turbulence. While it is expensive to compute this function using direct numerical simulation (DNS), Boffetta et al. (2010) showed that the solution to a simple parabolic model equation for $\bar{\rho}$ using the so-called Prandtl closure model closely matches results from DNS. Our objective is to demonstrate that the ensemble-averaged density field computed from 100 z-model runs reproduces results obtained from the Prandtl closure model, and thus also reproduces results from DNS. In particular, we shall demonstrate that the z-model, even at low resolution, captures the statistical qualities of

[2]For the purpose of numerical simulations, it is much easier to compute the uniform ensemble than the ensemble averaging using the invariant measure, but the viscous effects are extremely similar.

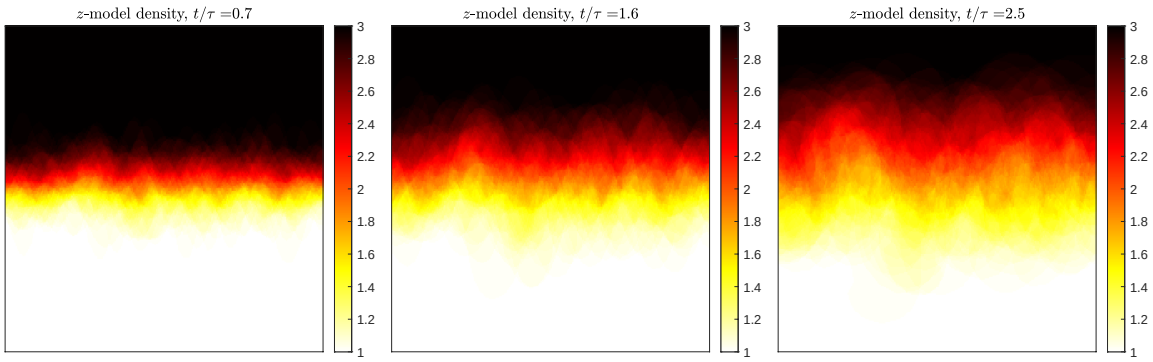


Figure 2.16: Ensemble averaged density for the 100 runs of the rocket rig analyzed above, showing a cross-section at $y = 0$.

turbulent mixing quite accurately and reproduces the remarkable self-similarity of the horizontally-averaged density.

Averaging the density transport equation $\partial_t \rho + \partial_x(\rho u) + \partial_y(\rho v) + \partial_z(\rho w) = 0$ over the horizontal (x and y) coordinates results in the equation $\partial_t \bar{\rho} + \partial_z \overline{\rho w} = 0$, where $\bar{\rho}$ is the horizontally averaged density field given by

$$\bar{\rho}(z,t) = \fint_{\mathbb{R}^2} \rho(x,y,z,t)dxdy,$$

and $\overline{\rho w}$ is the horizontally averaged vertical mass flux. To close the equation for $\bar{\rho}$, the Prandtl closure model assumes that $\overline{\rho w} = \kappa \partial_z \bar{\rho}$, where κ is known as the "eddy diffusivity". This eddy diffusivity has units of length^2/time, so it is natural to take $\kappa \propto h\dot{h}$, where h is a characteristic length and $\dot{h}$ is a characteristic velocity for the turbulent flow. In our case, $h \propto Agt^2$ is the characteristic mixing layer height in the rocket rig, so that

$$\kappa \propto (Ag)^2 t^3 \,.$$

Letting β^2 denote the dimensionless constant of proportionality, the following evolution equation for $\bar{\rho}$ is obtained (Boffetta et al., 2010):

$$\partial_t \bar{\rho} = (\beta Ag)^2 t^3 \partial_z^2 \bar{\rho} \,. \tag{2.3.2}$$

This equation has the similarity variable $\xi = z/(Agt^2)$, which results in a self-similar solution of

the form $\bar{\rho}(z,t) = P(\xi)$ for the density field in the rocket rig experiment given by

$$P(\xi) = \rho^- + \frac{\rho^+ - \rho^-}{2}\left(1 + \operatorname{erf}\left(\frac{\xi}{\beta}\right)\right). \tag{2.3.3}$$

Note that as $t \to 0^+$, $P(\xi)$ approaches the step-function initial density

$$\bar{\rho}(z,0) = \begin{cases} \rho^+, & z > 0, \\ \rho^-, & z \leqslant 0. \end{cases}$$

As noted above, Boffetta et al. (2010) have shown that the self-similar solution $P(\xi)$ to (2.3.2) is an accurate approximation to the density field $\bar{\rho}(z,t)$ computed from fully resolved DNS.

In order to determine if the z-model can capture the self-similar solution of the Prandtl closure model, we shall use the ensemble-averaged density field ρ computed from 100 z-model simulations, and then calculate the horizontally-averaged density field $\bar{\rho}(z,t)$. We note that the mass associated to the horizontally averaged density field, given by $\int_{-0.5\lambda}^{0.5\lambda} \bar{\rho}(z,t)dz$, is approximately conserved; in particular, on the full time-interval $0 \leqslant t \leqslant 2.5\tau$ of the numerical experiment, we have verified that mass deviates from its initial value by less than 1%. A series of time snapshots $\bar{\rho}(\cdot,t)$ are plotted in Figure 2.17 at various times between $t = 1.3\tau$ and $t = 2.5\tau$, at intervals $\Delta t = 0.2\tau$. To compare against the self-similar solution $P(\xi)$ in 2.3.3, we have plotted the curves $\bar{\rho}(z,t) = \bar{\rho}(Agt^2\xi, t)$ (for various values of t) as a function of ξ in Figure 2.18. Here β is chosen to be the "best-fit" value for the data, which we found to be approximately $\beta = 0.017$. As can be seen in Figure 2.18, the z-model horizontally-averaged density profiles $\bar{\rho}(z,t)$ enjoy the self-similar profile of the solution $P(\xi)$ produced by the Prandtl closure model, and are thereby compare well with fully resolved DNS.

We next demonstrate that the ensemble averaging of the z-model density field reproduces optimal mixing rates. As explained in Lin et al. (2011) and Thiffeault (2012), the mixing of a passive scalar (in our case the density ρ), advected by a velocity field $\boldsymbol{u}$, can be measured quantitatively using the homogeneous Sobolev norms

$$\|\rho\|_{\dot{H}^s} = \left(\int_{\mathbb{R}^3} |\boldsymbol{k}|^{2s} |\hat{\rho}(\boldsymbol{k})|^2 \mathrm{d}\boldsymbol{k}\right)^{1/2}$$

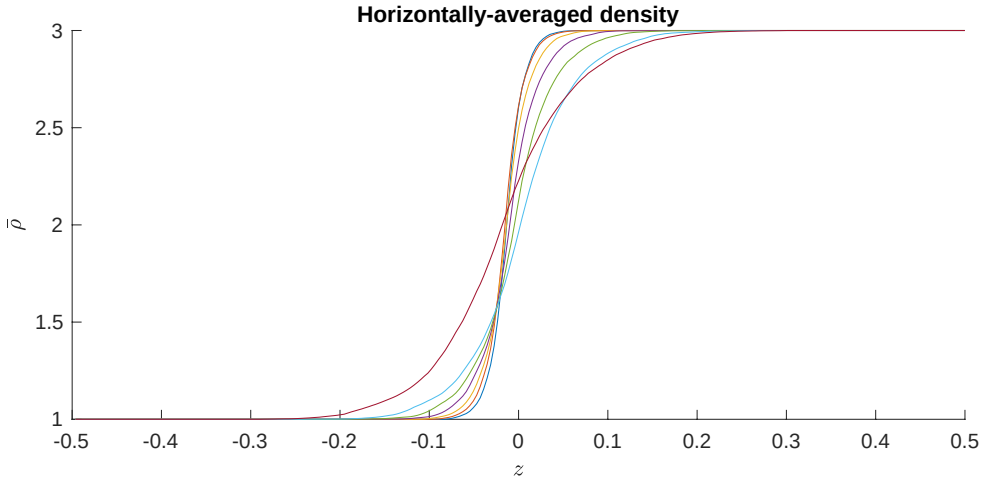


Figure 2.17: Horizontally averaged density field $\bar{\rho}(z,t)$ for the rocket rig experiment, computed from the ensemble-averaged z-model density, plotted at times between $t = 1.3\tau$ and $t = 2.5\tau$, with time intervals $\Delta t = 0.2\tau$.

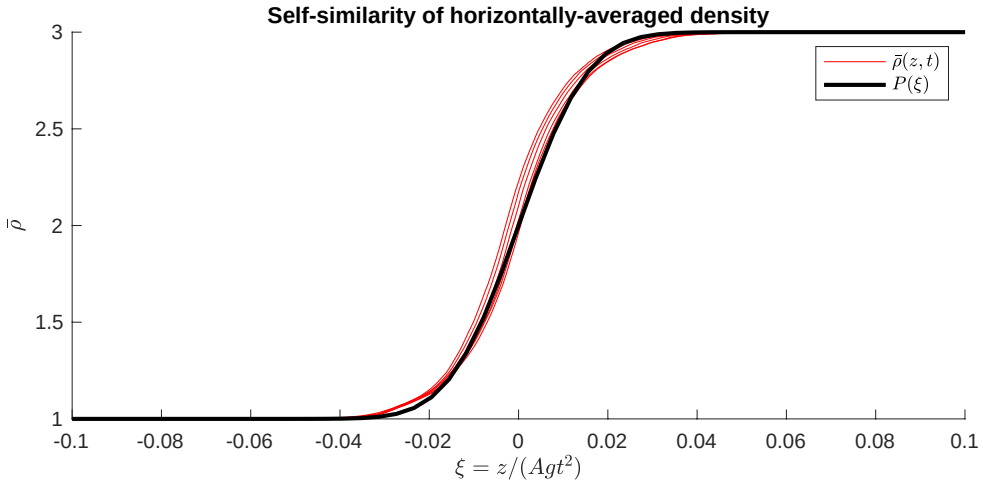


Figure 2.18: The same density profiles as in Figure 2.17, plotted as a function of the similarity variable $\xi = z/(Agt^2)$ and compared against the theoretical solution $P(\xi)$.

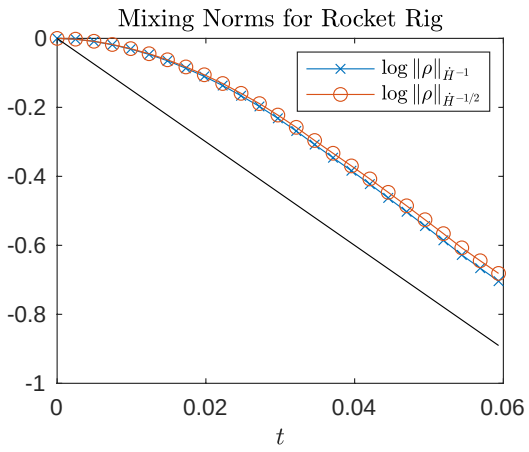


Figure 2.19: Mixing norms of the ensemble-averaged density shown in Figure 2.16, plotted on a log scale.

with $s < 0$. Of particular interest are the so-called *mixing norms* corresponding to the exponents $s = -1$ and $s = -1/2$. A fluid becomes molecularly mixed when the varying density field $\rho(x, y, z, t)$ converges to its spatial average $\langle\rho\rangle = \fint_{\mathbb{R}^3} \rho(x, y, z, t)dxdydz$. Lin et al. (2011) showed that $\rho(\cdot, t)$ can converge at most exponentially fast to its average in one of these mixing norms, and showed that optimal mixing is achieved if the density is advected by one of a few simple, explicit "stirring" velocity fields $\boldsymbol{u}(\boldsymbol{x}, t)$. However, it is unknown whether optimal mixing is achieved for more general velocity fields, such as those satisfying the Euler or Navier-Stokes equations. That is, optimal mixing occurs if

$$\|\rho(\cdot, t) - \langle\rho\rangle\|_{\dot{H}^s} \sim e^{-rt}, \quad s = -1 \text{ or } s = -\tfrac{1}{2}$$

for some constant $r > 0$ as time $t \to \infty$ (see Thiffeault, 2012). By computing the $\dot{H}^{-\frac{1}{2}}$ and $\dot{H}^{-1}$ norms of the ensemble-averaged rocket rig density in a small strip around the plane $z = 0$, we find that the Sobolev norms decay exponentially (Figure 2.19). In other words, the ensemble average of z-model simulations with randomly perturbed initial data is consistent with optimal mixing of the two fluids. While a single z-model simulation approximates the motion a fluid interface separating two inviscid fluids, the ensemble average of many simulations successfully models viscous mixing at the length scales of the random fluctuations of the data. A more in-depth study of mixing rates in Rayleigh-Taylor problems, and in particular whether they achieve optimal mixing, is an objective of our future studies.

2.3.6 Fluid Mixing in Complex Stratifications

In multiphase fluid problem, in which the interface exhibits significant roll-up and small-scale structure formation, the interface can "squeeze" a fluid into a very thin configuration, as the distance between portions of the fluid interface becomes smaller and smaller. The resulting small distance between portions of the interface creates (super-exponential) growth of the density gradient and ensures that traditional numerical schemes, based upon a multi-dimensional discretization of the fluid domains, can become prohibitively expensive due to severe small-scale resolution requirements. Such small-scale formation occurs in many situations when significant Kelvin-Helmholtz instability is allowed to develop, or when the fluid becomes turbulent. Our interface z-model is designed specifically for this small-scale scenario, in which the use of conventional numerics would not be feasible.

Unstable stratified flows with more than two fluid layers provide an interesting example of such small-scale structure formation. We shall consider the problem of two fluid interfaces separating three fluids, and our initial data is chosen as

$$\boldsymbol{u}_0(x,y,z) = \mathbf{0}, \qquad \rho_0(x,y,z) = \begin{cases} \rho_3, & z > h_2(x,y) \\ \rho_2, & h_1(x,y) \leqslant z \leqslant h_2(x,y) \\ \rho_1, & z < h_1(x,y) \end{cases}$$

where $\rho_1 < \rho_2 < \rho_3$ denote the initial densities of the three fluids, and h_1 and h_2 are given functions which represent the initial position of the two fluid interfaces. Our z-model is easily generalized to simulate such problems by introducing two interfaces $\Gamma_i(t)$, parametrized by $\boldsymbol{z}_i(s,t)$ and carrying vortex sheet densities $\boldsymbol{\mu}_i(s,t)$, $i = 1, 2$. Following our derivation of the standard z-model, we obtain that for $i = 1, 2$,

$$\partial_t \boldsymbol{z}_i(s,t) = \bar{\boldsymbol{u}}_i(s,t) := \frac{1}{4\pi} \sum_{j=1}^{2} \iint_{\mathbb{R}^2} \frac{\mu_{j2}(s',t)\partial_1 z_j(s',t) - \mu_{j1}(s',t)\partial_2 z_j(s',t)}{|z_i(s,t) - z_j(s',t)|^3} ds' \,,$$

$$\partial_t \mu_i(s,t) = A\nabla_s \left(|\bar{\boldsymbol{u}}_i(s,t)|^2 - \frac{1}{4} g_i^{jk}(s,t)\mu_{ij}(s,t)\mu_{ik}(s,t) - 2g z_i^3(s,t) \right) .$$

When the two fluid interfaces roll-up inside one another and the separation distance becomes ex-

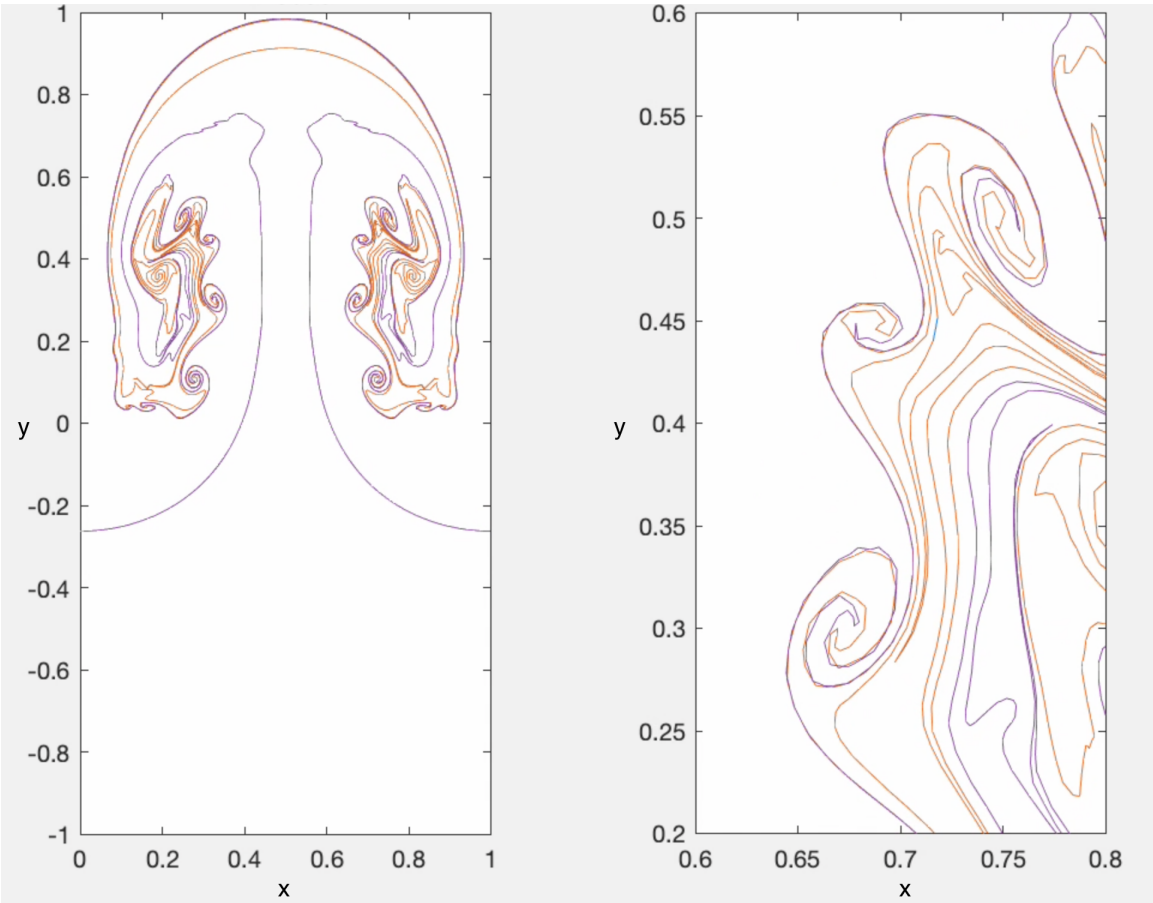


Figure 2.20: Simulation of an unstably stratified flow with densities $\rho_1 = 1.8$, $\rho_2 = 3$, $\rho_3 = 5$, with a sinusoidal initial perturbation of the lower interface. (*Left*) The full domain. (*Right*) Zoomed-in view of the Kelvin-Helmholtz instability.

ceedingly small, the density gradient grows exceedingly large, and traditional numerical schemes based on multi-dimensional grids require enormous resolution to accurately capture the small-scale features of the interface and maintain stability. On the other hand, a small interface separation distance does not impair the numerical stability of our interface model, and a two-interface interaction is used to demonstrate stability under small-scale formation. We consider a two-dimensional unstably stratified three-fluid flow with densities $\rho_1 = 1.8$, $\rho_2 = 3$, $\rho_3 = 5$, and with the two interfaces given a sinusoidal perturbation of wavelength λ and amplitude 0.01λ, separated by a distance 0.05λ. As shown in Figure 2.20, the unstable stratification accelerates the development of Rayleigh-Taylor instability, resulting in strong Kelvin-Helmholtz roll-up with the distance between the two interfaces becoming very small.

We next use our multiple-interface z-model to study the problem of fluid entrainment. Of

interest are the experiments of Jacobs and Dalziel (2005), who studied fluid mixing in the case where a layer of light fluid (density ρ^-) is initially sandwiched between two layers of heavy fluid (density ρ^+). For short times, this results in standard RTI in the top interface and stability in the bottom interface; at long times, the turbulent flow in the mixing layer becomes strong enough to disturb the lower interface and entrain some of the heavy fluid in the bottom layer. One of the hypotheses tested by Jacobs and Dalziel is that the horizontally-averaged species fraction of light fluid, given by

$$f(z,t) = \int_{\mathbb{R}^2} \frac{\rho^+ - \rho(x,y,z,t)}{\rho^+ - \rho^-} dxdy, \tag{2.3.4}$$

exhibits an asymptotically self-similar distribution at large times, analogous to the self-similarity of the density field shown in figure 2.18. [3] However, unlike for the standard rocket rig, the simple Prandtl closure model will not suffice, erroneously predicting vertically symmetric growth in the concentration profile. Instead, one finds that

$$\frac{f(z,t)}{f_{max}(t)} = F(\zeta), \qquad \zeta = \frac{z - z_c(t)}{w_{1/2}(t)},$$

where $z_c(t)$ is the centroid of the distribution $f(z,t)$, $w_{1/2}(t)$ is the width-at-half-height of $f(z,t)$, and $f_{max}(t) = \max f(\cdot,t)$. Moreover, it was shown by dimensional arguments and verified experimentally by Jacobs and Dalziel (2005) that

$$f_{max} \sim \frac{1}{t}, \qquad w_{1/2} \sim t$$

as $t \to \infty$. We use our multi-interface z-model to compute the concentration curves $f(z,t)$. In particular, we compute the ensemble-averaged density field from 25 z-model runs, and compute the horizontally-averaged species fraction using the formula (2.3.4). A selection of the resulting species fraction curves $f(z,t)$, as well as their rescaled counterparts, are shown in Figure 2.21. As can be seen in Figure 2.22, solutions of the z-model verify the long-time growth prediction for the functions $w_{1/2}(t)$ and $1/f_{max}(t)$ given by Jacobs and Dalziel. As seen in Figure 2.22, our computation of the functions $w_{1/2}(t)$ and $1/f_{max}(t)$ indeed demonstrate long-time linear growth. Thus the presence

[3] Note that the species fraction differs from the density by an affine transformation. We simply choose to model the species fraction in this section to match the experimental results of Jacobs and Dalziel (2005).

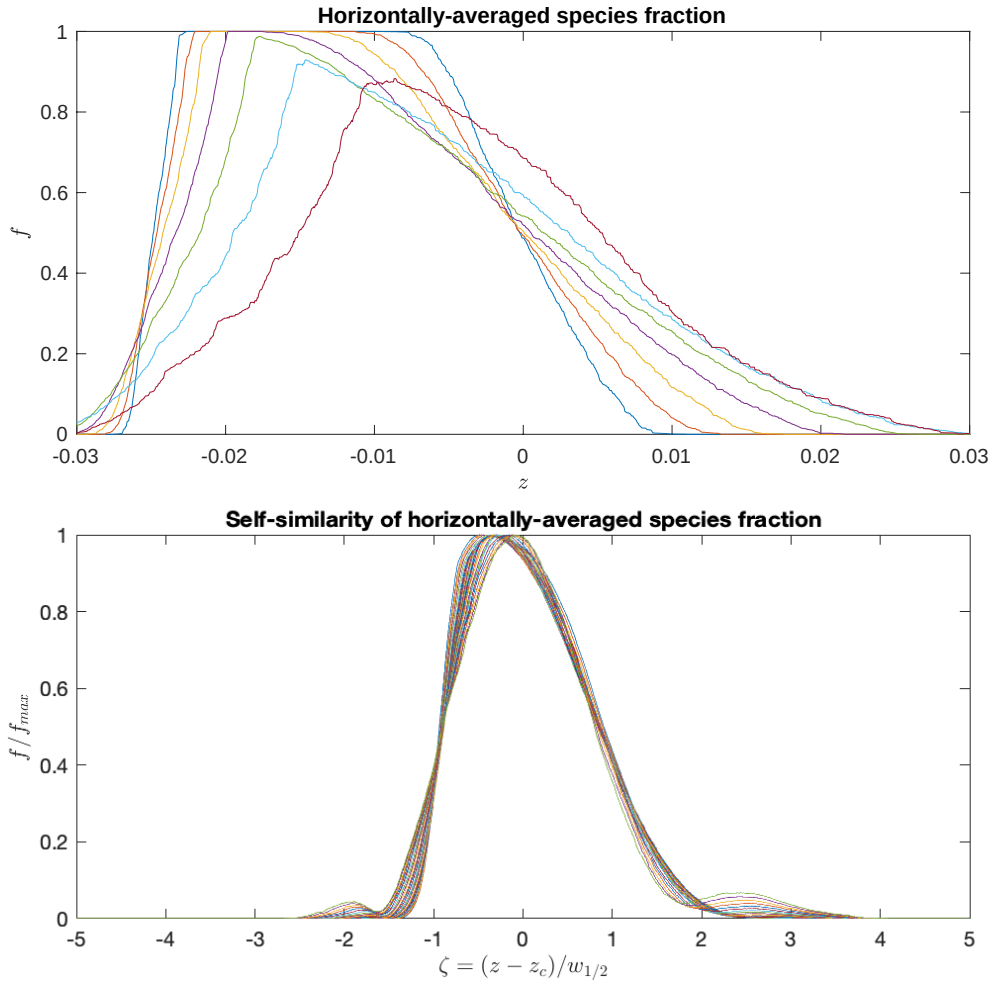


Figure 2.21: (*Top*) Mean species fraction $f(\cdot, t)$, plotted at various times. (*Bottom*) Mean species fraction, plotted in rescaled coordinates to highlight self-similarity of concentration profiles.

of a layer of heavy fluid below an unstably stratified density field serves to stabilize the resulting Rayleigh-Taylor instability, resulting in linear rather than quadratic growth of the mixing layer.

2.4 Conclusions

We have derived and tested our interface z-model for Rayleigh-Taylor instability where the material interface is represented by a parametrized surface in 3D, and the velocity is reconstructed using a boundary integral method, by assuming potential flow in the fluid bulk. Using our models, we have studied several classical problems in Rayleigh-Taylor instability, including single-mode and random multi-mode initial data. We have demonstrated that ensemble averages of inviscid RTI with random multi-mode initial data reproduce the self-similar vertical density distribution predicted by a simple

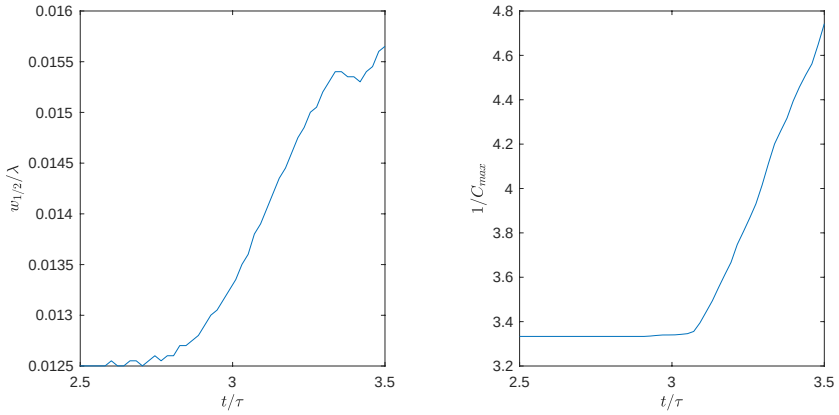


Figure 2.22: Time evolution of the width-at-half-height $w_{1/2}(t)$ (*Left*) and the reciprocal of the maximum concentration $1/f_{max}(t)$ (*Right*), showing linear growth after $t/\tau = 3$.

Prandtl closure model, and achieves the theoretically optimal exponential mixing rate for passive scalar fields. Additionally, the derivation of our one-interface model has been generalized to allow for multiple fluid interfaces, thus permitting the study of unstably stratified fluid flow. We have demonstrated self-similarity of the species fraction profile for a heavy-light-heavy initial distribution of densities, and corroborated the similarity exponents measured experimentally by Jacobs and Dalziel (2005). These three-phase fluid problems provide a significant numerical challenge for conventional numerical methods, as the distance between the two interfaces becomes extremely small and the gradient of density becomes extremely large, which our model is able to simulate stably. The idea of dimension reduction via the Birkhoff-Rott integral is now classical, but after more than six decades of simulation efforts, few competitive results exist for three-dimensional dynamics. We have been able to identify the appropriate modifications for the evolution of the amplitude of vorticity which allow our interface model to avoid severe numerical difficulties and retain high accuracy of the location of vorticity spikes that initial interface roll-up. We have demonstrated the efficacy of these models for single-mode initial data and random multi-mode initial data when compared against experimental data, which shows that two-phase potential flow is sufficiently rich to capture the complexity of 3D RTI. This makes our model a stable and accurate alternative to the challenging simulations of the full two-phase irrotational and incompressible Euler equations. In the future, we hope to extend this model to include topological transitions in the interface, so we can test the efficacy of our model in late-stage RTI and turbulent mixing, and

perform a more detailed study of optimal mixing rates in RTI-driven turbulence.

Chapter 3

A multiscale vortex method for compressible flow

3.1 Introduction

Compressible, vortex-dominated flows present a formidable challenge for numerical simulation due to the presence of fast-moving acoustic waves, sharp density gradients, and instabilities at many scales. In many physically relevant regimes—such as Rayleigh–Taylor and Richtmyer–Meshkov instabilities—vorticity is concentrated near material interfaces, which then roll up at finer and finer scales and create extremely complex vortical structures. Numerically resolving these structures with traditional grid-based solvers quickly becomes prohibitively expensive, and therefore we seek an efficient subgrid-scale model to capture these instabilities.

Incompressible interface models have proven remarkably effective for capturing the complex vortex dynamics of contact discontinuities in fluid flows dominated by shear, as demonstrated by Ramani and Shkoller (2020), Canfield et al. (2020), and Pandya and Shkoller (2023), among others. However, many physical phenomena involving RT/RM instabilities involve compressible effects that classical incompressible models cannot capture. In this chapter, we present a multiscale framework that couples an interface model for contact discontinuities, based on a generalization of the z-model, to a compressible background flow. Our approach builds on the multiscale methodology introduced by Ramani and Shkoller (2020), which employs a novel decomposition of the velocity field into a coarse-scale compressible part and fine-scale incompressible part. However, they used a highly restrictive model for the fine scale velocity—known as the z-model—which assumed constant density ratio across the material interface. Using a novel derivation, we introduce a new version of the z-model which allows for a variable density ratio, and extending the multiscale method to allow interfacial dynamics in a compressible regime with highly oscillatory density ratio across the material interface. Notably, our model avoids reliance on Bernoulli's equation or a velocity potential, which allows the underlying vortex method to accommodate shock-induced density gradients and interfacial density ratios which change in space and time. Our method also introduces a new algorithm for numerically computing jumps and averages across the contact, and corrects the weak baroclinic torque term used in Ramani and Shkoller (2020) for shock-contact interaction.

After reviewing the governing equations for compressible and incompressible flows, we discuss how to adapt the z-model to the 2d setting, and how a novel 'continuous-singular decomposition' of the vorticity equation allows us to extend the z-model into the compressible regime. We derive

a multiscale model that can accommodate variable density ratios and couples naturally to a background compressible solver. We implement this multiscale z-model in a hybrid numerical scheme that couples a WENO-based compressible background solver with a high-order discretization of the interface dynamics. Numerical results on RTI, RMI, and a perturbed radial explosion problem confirm that the method accurately captures small-scale vortical structures more effectively than the multiscale model of Ramani and Shkoller (2020), especially for problems with highly variable density ratio across the contact.

3.2 Governing equations

In this section, we describe the basic equations governing compressible and incompressible flow, and the challenges associated with their numerical solution.

3.2.1 The compressible Euler equations

The motion of a two-dimensional compressible fluid under the influence of gravity is modeled by the compressible Euler equations with gravity, which are a system of nonlinear partial differential equations, representing conservation of mass, momentum, and energy. They are written

$$\partial_t \boldsymbol{Q} + \partial_x \boldsymbol{F}(\boldsymbol{Q}) + \partial_y \boldsymbol{G}(\boldsymbol{Q}) = \boldsymbol{f}, \tag{3.2.1}$$

where

$$\boldsymbol{Q} = \begin{pmatrix} \rho \\ \rho u \\ \rho v \\ \rho e \end{pmatrix}, \qquad \boldsymbol{F}(\boldsymbol{Q}) = \begin{pmatrix} \rho u \\ \rho u^2 + p \\ \rho uv \\ (\rho e + p)u \end{pmatrix}, \qquad \boldsymbol{G}(\boldsymbol{Q}) = \begin{pmatrix} \rho v \\ \rho uv \\ \rho v^2 + p \\ (\rho e + p)v \end{pmatrix}, \qquad \boldsymbol{f} = \begin{pmatrix} 0 \\ 0 \\ -\rho g \\ -\rho g v \end{pmatrix}$$

We will denote the spatial variables in vectorial form as $\boldsymbol{x} = (x, y)$ and the velocity as $\boldsymbol{u} = (u, v)$. The system is closed by an *equation of state*, relating the pressure p to the fundamental variables $(\rho, \boldsymbol{u}, e)$. In our case, we will assume the equation of state of a perfect gas with adiabatic index γ,

$$p = (\gamma - 1)\rho(e - \tfrac{1}{2}|\boldsymbol{u}|^2).$$

We define a *classical solution* to (3.2.1) as a function $\boldsymbol{Q} \in C^1(\mathbb{R}^2 \times [0,T))$ which satisfies (3.2.1) pointwise, and a *weak solution* to (3.2.1) as a function $\boldsymbol{Q} \in L^1_{loc}(\mathbb{R}^2 \times [0,T))$ such that

$$\int_0^T \int_{\mathbb{R}^2} [\boldsymbol{Q}\partial_t\phi + \boldsymbol{F}(\boldsymbol{Q})\partial_x\phi + \boldsymbol{G}(\boldsymbol{Q})\partial_y\phi - \boldsymbol{f}\phi]d\boldsymbol{x}dt = \int_{\mathbb{R}^2\times\{t=0\}} \boldsymbol{Q}\phi\, d\boldsymbol{x},$$

for all test functions $\phi \in C_c^\infty(\mathbb{R}^2 \times [0,T))$.

Suppose that $\boldsymbol{Q}(\boldsymbol{x},t)$ is a weak solution to (3.2.1), and that $\boldsymbol{Q}$ is smooth away from a surface $\Gamma \subseteq \mathbb{R}^2 \times [0,T)$. Along Γ, the state variables may be discontinuous, and thus we refer to Γ as a *surface of discontinuity*. For $t \in [0,T)$, let $\Gamma(t)$ denote the intersection of Γ with the plane $\mathbb{R}^2 \times \{t\}$, and let $V(\boldsymbol{x},t)$ denote the normal velocity of the point $\boldsymbol{x} \in \Gamma(t)$. The *jump* of a quantity $f(\boldsymbol{x},t)$ across Γ is given by

$$[\![f]\!](\boldsymbol{x},t) := \lim_{h\to 0}[f(\boldsymbol{x}+h\boldsymbol{n},t) - f(\boldsymbol{x}-h\boldsymbol{n},t)], \qquad (\boldsymbol{x},t) \in \Gamma, \tag{3.2.2}$$

where $\boldsymbol{n} = (n_x, n_y)$ is the unit normal vector to $\Gamma(t)$ at the point $\boldsymbol{x}$. It is easy to show that the jump in the state variables across the interface must satisfy the *Rankine-Hugoniot conditions*,

$$V[\![\boldsymbol{Q}]\!] = [\![\boldsymbol{F}(\boldsymbol{Q})n_x + \boldsymbol{G}(\boldsymbol{Q})n_y]\!], \tag{3.2.3}$$

or in components,

$$V[\![\rho]\!] = [\![\rho\boldsymbol{u}\cdot\boldsymbol{n}]\!], \qquad V[\![\rho\boldsymbol{u}]\!] = [\![\rho\boldsymbol{u}(\boldsymbol{u}\cdot\boldsymbol{n}) + p\boldsymbol{n}]\!], \qquad V[\![\rho e]\!] = [\![(\rho e + p)\boldsymbol{u}\cdot\boldsymbol{n}]\!].$$

If the normal velocity $\boldsymbol{u}\cdot\boldsymbol{n}$ experiences a nonzero jump across the surface of discontinuity, $\Gamma(t)$ represents a *shock wave*. On the other hand, if $[\![\boldsymbol{u}\cdot\boldsymbol{n}]\!] = 0$, then the Rankine-Hugoniot conditions simplify to

$$V = \boldsymbol{u}\cdot\boldsymbol{n}, \qquad [\![\boldsymbol{u}\cdot\boldsymbol{n}]\!] = 0, \qquad [\![p]\!] = 0.$$

In this case $\Gamma(t)$ represents a *contact discontinuity*. Although we will consider flows containing shock waves, our attention will be focused on contact discontinuities because they carry intense

vorticity and are responsible for the creation of small-scale structures and mixing.

3.2.2 The incompressible Euler equations

In nondimensional form, the compressible Euler system in the absence of external forces may be rewritten solely in terms of the pressure p, velocity u, and entropy s as

$$\frac{1}{\rho}\frac{\partial \rho}{\partial p}(\partial_t p + \boldsymbol{u}\cdot\nabla p) + \nabla\cdot\boldsymbol{u} = 0, \tag{3.2.4a}$$

$$\rho(\partial_t \boldsymbol{u} + \boldsymbol{u}\cdot\nabla\boldsymbol{u}) + \frac{1}{\varepsilon}\nabla p = 0, \tag{3.2.4b}$$

$$\partial_t s + \boldsymbol{u}\cdot\nabla s = 0, \tag{3.2.4c}$$

where $\rho = \rho(p, s)$ is the equation of state, and ε is the square of some reference Mach number. We shall refer to asymptotic solution of (3.2.4) as $\varepsilon \to 0$ as the *incompressible limit* of the Euler equations. In the incompressible limit, the pressure converges to a constant,

$$p^\varepsilon(\boldsymbol{x}, t) \to p^*,$$

and the velocity and entropy $(\boldsymbol{u}^\varepsilon, s^\varepsilon)$ converge to solutions of the incompressible system

$$\nabla\cdot\bar{\boldsymbol{u}} = 0, \tag{3.2.5a}$$

$$\rho(\partial_t \bar{\boldsymbol{u}} + \bar{\boldsymbol{u}}\cdot\nabla\bar{\boldsymbol{u}}) + \nabla\bar{p} = 0, \tag{3.2.5b}$$

$$\partial_t \bar{s} + \bar{\boldsymbol{u}}\cdot\nabla\bar{s} = 0, \tag{3.2.5c}$$

where $\rho = \rho(p^*, s)$. Note that the density ρ is also transported, as it is now a function of entropy alone. The first results on the incompressible limit were by Ebin, who showed using techniques from global analysis that for an isentropic perfect gas on the torus $\mathbb{T}^d$, the solution $(\rho^\varepsilon, \boldsymbol{u}^\varepsilon)$ of the compressible Euler equations with incompressible initial data (i.e. ρ_0 constant, $\boldsymbol{u}_0$ divergence-free) converged in Sobolev spaces to a solution $(\bar{\rho}, \bar{\boldsymbol{u}})$ of the incompressible Euler equations with the same initial data (Ebin, 1975),

$$\lim_{\varepsilon\to 0} \|\rho^\varepsilon - \bar{\rho}\|_{C^0_t H^k_x} = 0, \qquad \lim_{\varepsilon\to 0} \|\boldsymbol{u}^\varepsilon - \bar{\boldsymbol{u}}\|_{C^t_0 H^k_x} = 0, \qquad k > 1 + \tfrac{d}{2}.$$

3.3 Review of the 2d z-model

The z-models are a suite of interface models for contact discontinuities in 2d and 3d incompressible flow based on a novel asymptotic expansion in the *nonlocality* of the fluid flow. These models take the form of coupled evolution equations for the interface position $\boldsymbol{Z}(s,t)$ and the *amplitude of vorticity* $\mu(s,t)$ representing the vortex sheet density (or equivalently, the tangential velocity jump). The equations are derived by expanding the Birkhoff–Rott kernel in powers of interfacial distance and truncating at leading order, resulting in what we term the *lower-order z-model*. Reintroducing the full Birkhoff-Rott velocity into one or both of the z-model equations results in the *medium-order* and *higher-order* z-models. The 2d lower-order z-model was first introduced in Granero-Belinchón and Shkoller (2017), and the 2d medium-order variant was introduced in Ramani and Shkoller (2020); the higher-order z-model was introduced in Pandya and Shkoller (2023), in which all three models were derived in 3d.

Divide the plane $\mathbb{R}^2$ into two regions $\Omega^+(t)$ and $\Omega^-(t)$, separated by a free surface $\Gamma(t)$. The original z-model begins with the two-phase incompressible, irrotational Euler equations with gravity,

$$\rho^\pm(\partial_t \boldsymbol{u}^\pm + \boldsymbol{u}^\pm \cdot \nabla \boldsymbol{u}^\pm) + \nabla p^\pm = -\rho^\pm g \boldsymbol{e}_y, \qquad \boldsymbol{x} \in \Omega^\pm(t), \tag{3.3.1a}$$

$$\nabla \cdot \boldsymbol{u}^\pm = \nabla \times \boldsymbol{u}^\pm = 0, \qquad \boldsymbol{x} \in \Omega^\pm(t), \tag{3.3.1b}$$

together with the continuity conditions at the free surface $\Gamma(t)$,

$$[\![\boldsymbol{u} \cdot \boldsymbol{n}]\!] = 0, \qquad [\![p]\!] = 0, \qquad \boldsymbol{x} \in \Gamma(t). \tag{3.3.2}$$

Here $\boldsymbol{u}^\pm = (u^\pm, v^\pm)$ is the fluid velocity, $p^\pm$ is the pressure, and $\rho^\pm$ is the density, which is assumed to be constant in each phase, and the double brackets denote the *jump* across the interface,

$$[\![f]\!](\boldsymbol{x},t) := \lim_{h \to 0} \big[f^+(\boldsymbol{x} + h\boldsymbol{n}, t) - f^-(\boldsymbol{x} - h\boldsymbol{n}, t) \big], \qquad \boldsymbol{x} \in \Gamma(t), \tag{3.3.3}$$

where $\boldsymbol{n}$ is the unit normal vector to $\Gamma(t)$ at $\boldsymbol{x}$. Suppose the velocity $\boldsymbol{u}(\boldsymbol{x},t)$ is regarded as a

piecewise function defined a.e. on $\mathbb{R}^2$,

$$\boldsymbol{u}(\boldsymbol{x},t) = \begin{cases} \boldsymbol{u}^+(\boldsymbol{x},t), & \boldsymbol{x} \in \Omega^+(t), \\ \boldsymbol{u}^-(\boldsymbol{x},t), & \boldsymbol{x} \in \Omega^-(t). \end{cases}$$

Although no vorticity is present in each phase, the discontinuity in tangential velocity induces a distributional vorticity supported on $\Gamma(t)$,

$$\nabla \times \boldsymbol{u}(\boldsymbol{x},t) = -\int_{\Gamma(t)} [\![\boldsymbol{u}\cdot\boldsymbol{\tau}]\!](\boldsymbol{x}',t)\delta(\boldsymbol{x}-\boldsymbol{x}')d\boldsymbol{x}'.$$

More precisely, this means that for any test function $\phi \in C_c^\infty(\mathbb{R}^2)$, one has

$$\langle \nabla \times \boldsymbol{u}, \phi \rangle := -\int_{\mathbb{R}^2} \boldsymbol{u}\cdot\nabla^\perp\phi = -\int_\Gamma [\![\boldsymbol{u}\cdot\boldsymbol{\tau}]\!]\phi$$

We proceed by introducing a velocity potential $\phi^\pm$ in each phase, which allows us to rewrite the momentum equation as a total gradient and integrate once to obtain *Bernoulli's equation*,

$$\partial_t\phi^\pm + \tfrac{1}{2}|\nabla\phi^\pm|^2 + p^\pm/\rho^\pm = 0, \qquad \boldsymbol{x} \in \Omega^\pm(t). \tag{3.3.4}$$

Introducing a parametrization of the interface $\boldsymbol{Z}(s,t) = (X(s,t), Y(s,t))$ such that

$$\partial_t\boldsymbol{Z}(s,t) = \tfrac{1}{2}(\nabla\phi^+ + \nabla\phi^-)\circ\boldsymbol{Z},$$

we define the *amplitude of vorticity*

$$\mu(s,t) := \partial_s\boldsymbol{Z}(s,t)\cdot[\![\boldsymbol{u}]\!](\boldsymbol{Z}(s,t),t).$$

After a straightforward manipulation of Bernoulli's equation, one finds that

$$\partial_t\mu + 2A\partial_t(\partial_t\boldsymbol{Z}\cdot\partial_s\boldsymbol{Z}) = A\partial_s(|\partial_t\boldsymbol{Z}|^2 - \tfrac{1}{4}|\partial_s\boldsymbol{Z}|^{-2}\mu^2 - 2gY), \tag{3.3.5}$$

where $A = (\rho^+ - \rho^-)/(\rho^+ + \rho^-)$ is the *Atwood number*. Finally, the interfacial velocity is recon-

structed using the Birkhoff-Rott integrl,

$$\partial_t \boldsymbol{Z}(s,t) = \frac{1}{2\pi}\int_{\mathbb{R}} \frac{[\boldsymbol{Z}(s,t)-\boldsymbol{Z}(s',t)]^{\perp}}{|\boldsymbol{Z}(s,t)-\boldsymbol{Z}(s',t)|^2}\mu(s',t)ds'. \tag{3.3.6}$$

Equations (3.3.6) and (3.3.5) give a completely equivalent description of the incompressible, irrotational Euler equations (3.3.1), using a boundary integral equation.

The z-model is obtained from (3.3.6) and (3.3.5) by two simple modifications: first, by regularizing the Birkhoff-Rott integral to avoid numerical instability, using Krasny's desingularization method Krasny (1986a); and second, by dropping the time-derivative term $2A\partial_t(\partial_t \boldsymbol{Z}\cdot\partial_s \boldsymbol{Z})$. It was argued in Pandya and Shkoller (2023) that these modifications are justified, and that they provide an accurate approximation to the Euler equations. To be precise, the z-model is the system of equations

$$\partial_t \boldsymbol{Z}(s,t) = \frac{1}{2\pi}\int_{\mathbb{R}} \frac{[\boldsymbol{Z}(s,t)-\boldsymbol{Z}(s',t)]^{\perp}}{\delta^2+|\boldsymbol{Z}(s,t)-\boldsymbol{Z}(s',t)|^2}\mu(s',t)ds', \tag{3.3.7a}$$

$$\partial_t \mu = A\partial_s(|\partial_t \boldsymbol{Z}|^2 - \tfrac{1}{4}|\partial_s \boldsymbol{Z}|^{-2}\mu^2 - 2gY) \tag{3.3.7b}$$

3.4 Review of the multiscale model of Ramani and Shkoller

Ramani and Shkoller propose a novel multiscale framework for simulating Rayleigh–Taylor (RTI) and Richtmyer–Meshkov (RMI) instabilities in two-dimensional, inviscid, compressible flows with vorticity. The core of their approach is a decomposition of the velocity field $\boldsymbol{u}$ into compressible and incompressible components:

$$\boldsymbol{u} = \bar{\boldsymbol{u}} + \tilde{\boldsymbol{u}},$$

where $\bar{\boldsymbol{u}}$ is an incompressible, irrotational component capturing small-scale, interfacial vortex dynamics, and $\tilde{\boldsymbol{u}}$ is a compressible component resolved on a coarser grid. This decomposition is based on a two-phase elliptic system of Hodge type, allowing each velocity component to be evolved on

different scales tailored to their physical roles:

$$\begin{cases} \nabla \cdot \bar{\boldsymbol{u}}^{\pm} = 0, & \boldsymbol{x} \in \Omega^{\pm}(t) \\ \nabla \times \bar{\boldsymbol{u}}^{\pm} = 0, & \boldsymbol{x} \in \Omega^{\pm}(t) \\ [\![\bar{\boldsymbol{u}} \cdot \boldsymbol{n}]\!] = 0, & \boldsymbol{x} \in \Gamma(t) \\ [\![\bar{\boldsymbol{u}} \cdot \boldsymbol{\tau}]\!] = [\![\boldsymbol{u} \cdot \boldsymbol{\tau}]\!], & x \in \Gamma(t) \end{cases} \qquad \begin{cases} \nabla \cdot \tilde{\boldsymbol{u}}^{\pm} = \nabla \cdot \boldsymbol{u}^{\pm}, & \boldsymbol{x} \in \Omega^{\pm}(t) \\ \nabla \times \tilde{\boldsymbol{u}}^{\pm} = \nabla \times \boldsymbol{u}^{\pm}, & \boldsymbol{x} \in \Omega^{\pm}(t) \\ [\![\tilde{\boldsymbol{u}} \cdot \boldsymbol{n}]\!] = 0, & \boldsymbol{x} \in \Gamma(t) \\ [\![\tilde{\boldsymbol{u}} \cdot \boldsymbol{\tau}]\!] = 0, & x \in \Gamma(t) \end{cases}$$

To compute the incompressible velocity $\bar{\boldsymbol{u}}$, the authors employ the 2d z-model described in the previous section, approximating the solution of the incompressible Euler equations

$$\begin{aligned} \bar{\rho}^{\pm}(\partial_t \bar{\boldsymbol{u}}^{\pm} + \bar{\boldsymbol{u}}^{\pm} \cdot \nabla \bar{\boldsymbol{u}}^{\pm}) + \nabla \bar{p}^{\pm} = 0, & \qquad \boldsymbol{x} \in \Omega^{\pm}(t) \\ \nabla \times \bar{\boldsymbol{u}}^{\pm} = \nabla \cdot \bar{\boldsymbol{u}}^{\pm} = 0, & \qquad \boldsymbol{x} \in \Omega^{\pm}(t) \\ [\![\bar{\boldsymbol{u}} \cdot \boldsymbol{n}]\!] = 0, & \qquad \boldsymbol{x} \in \Gamma(t) \\ [\![\bar{p}]\!] = 0, & \qquad x \in \Gamma(t) \end{aligned}$$

where $\bar{\rho}^{\pm}$ are constants which are chosen to approximate the density on either side of the interface, and $\bar{p}$ is an incompressible pressure field enforcing the incompressibility of $\bar{\boldsymbol{u}}$. The compressible component $\tilde{\boldsymbol{u}}$ is computed using a simplified finite-difference WENO scheme with a localized, spacetime smooth artificial viscosity (via the so-called C-method of Ramani et al., 2019a,b), and it incorporates forcing from the incompressible component $\bar{\boldsymbol{u}}$:

$$\begin{aligned} \partial_t \rho + \nabla \cdot (\rho \tilde{\boldsymbol{u}}) &= -\nabla \cdot (\rho \bar{\boldsymbol{u}}) \\ \partial_t (\rho \tilde{\boldsymbol{u}}) + \nabla \cdot (\rho \tilde{\boldsymbol{u}} \otimes \tilde{\boldsymbol{u}}) + \nabla p &= -\partial_t (\rho \bar{\boldsymbol{u}}) - \nabla \cdot (\rho \bar{\boldsymbol{u}} \otimes \bar{\boldsymbol{u}} + \rho \bar{\boldsymbol{u}} \otimes \tilde{\boldsymbol{u}} + \rho \tilde{\boldsymbol{u}} \otimes \bar{\boldsymbol{u}}) \\ \partial_t (\rho e) + \nabla \cdot ((\rho e + p) \tilde{\boldsymbol{u}}) &= -\nabla \cdot ((\rho e + p) \bar{\boldsymbol{u}}) \end{aligned}$$

Importantly, these equations are solved in conservation form, so that the total mass $\int_\Omega \rho$, momentum $\int_\Omega \rho(\bar{\boldsymbol{u}} + \tilde{\boldsymbol{u}})$, and energy $\int_\Omega \rho e$ are conserved. The coupling ensures that subgrid-scale information from the interface dynamics informs the evolution of the larger-scale compressible flow, and the large-scale compressible flow corrects for the effects of bulk compression and vorticity.

The resulting multiscale model achieves significant computational efficiency by resolving small-

scale structure only along a one-dimensional interface, rather than across the full two-dimensional domain. This makes it well-suited for problems where the dominant dynamics are interfacial, as in RTI and RMI.

3.5 The multiscale z-model

Extending the z-model to compressible flow presents several theoretical and practical obstacles. The classical z-model is built upon the incompressible Euler equations and fundamentally relies on assumptions that do not hold in compressible regimes. First, the Biot–Savart integral formulation, which underlies the z-model's representation of interface-induced velocity, is valid only for incompressible flows. This is because the Biot–Savart law yields divergence-free velocity fields, and thus cannot represent the compressible dynamics or acoustic wave propagation present in real gas dynamics. Second, the derivation of the z-model invokes Bernoulli's equation, which assumes the existence of a velocity potential in each phase, and thus requires the flow to be irrotational in both $\Omega^+(t)$ and $\Omega^-(t)$. However, compressible flows often exhibit bulk compression and vorticity, rendering this assumption invalid. Third, the original z-model requires prescribing a constant Atwood number $A = (\rho^+ - \rho^-)/(\rho^+ + \rho^-)$ to close the evolution equations. While this is a reasonable simplification in idealized settings, it fails to account for the spatial and temporal variations in density ratios that naturally arise in compressible systems—particularly along contact discontinuities subject to shock compression, rarefaction, or stratification.

To address these issues, we introduce a new derivation based on what we term a *continuous-singular decomposition* of the vorticity equation in the compressible Euler system. Our multiscale method uses a compressible-incompressible decomposition of the velocity field similar to Ramani and Shkoller (2020), but the fine-scale incompressible velocity is found by decomposing the curl of the momentum equation in the sense of distributions. This yields two distinct contributions: a *bulk* vorticity equation governing the evolution in the fluid interiors, and a *singular* interface condition that captures the compatibility of vorticity generation across a sharp interface. This decomposition reveals a natural generalization of the z-model that does not rely on Bernoulli's equation and can accommodate variable density ratios along the interface. The singular part leads to an evolution equation for the vortex sheet strength $\mu(s,t)$, which closely resembles the classical z-

model but features coefficients that explicitly depend on the local density values on either side of the interface. Crucially, the resulting compressible z-model is not self-contained: it requires knowledge of the background velocity and density fields along the interface, evaluated from the compressible solution in the bulk. However, within the multiscale framework introduced by Ramani and Shkoller Ramani and Shkoller (2020), this is a feature rather than a limitation.

This perspective offers two significant advantages. First, it allows us to retain the computational efficiency of the classical z-model while coupling it to a fully compressible simulation capable of capturing the effects of bulk compression and vorticity. Second, it enables accurate modeling of flows with strong variation in density—such as Richtmyer–Meshkov instability or stratified Rayleigh-Taylor instability—without imposing artificial constraints on the interface properties.

3.5.1 The two-phase compressible Euler equations

Let $\Omega^+(t)$ and $\Omega^-(t)$ be open, bounded domains in $\mathbb{R}^2$, separated by a free surface $\Gamma(t)$. Consider the two-phase compressible Euler system with gravity,

$$\partial_t \rho^\pm + \nabla \cdot (\rho^\pm \boldsymbol{u}^\pm) = 0, \qquad \boldsymbol{x} \in \Omega^\pm(t) \tag{3.5.1a}$$

$$\partial_t (\rho^\pm \boldsymbol{u}^\pm) + \nabla \cdot (\rho^\pm \boldsymbol{u}^\pm \otimes \boldsymbol{u}^\pm) + \nabla p^\pm = -\rho^\pm g \boldsymbol{e}_y, \qquad \boldsymbol{x} \in \Omega^\pm(t) \tag{3.5.1b}$$

$$\partial_t (\rho^\pm e^\pm) + \nabla \cdot ((\rho^\pm e^\pm + p^\pm)\boldsymbol{u}^\pm) = -\rho^\pm g v^\pm, \qquad \boldsymbol{x} \in \Omega^\pm(t) \tag{3.5.1c}$$

where $\rho^\pm$ is the density of the gas, $\boldsymbol{u}^\pm = (u^\pm, v^\pm)$ the velocity, $e^\pm$ the specific energy, and $p^\pm$ is the pressure, given by the ideal gas law,

$$p = (\gamma - 1)\rho(e - \tfrac{1}{2}|\boldsymbol{u}|^2).$$

We will assume that $(\rho^\pm, u^\pm, v^\pm, p^\pm, e^\pm)$ are in $C^2(\Omega^\pm)$ and satisfy the system (3.5.1) classically in $\Omega^\pm$. Additionally, we impose the continuity conditions

$$[\![\boldsymbol{u} \cdot \boldsymbol{n}]\!] = 0, \qquad [\![p]\!] = 0, \qquad \boldsymbol{x} \in \Gamma(t), \tag{3.5.2}$$

where $\boldsymbol{n}$ is the unit normal vector to $\Gamma(t)$, and the double brackets $[\![\cdot]\!]$ denote the *jump* across the free surface $\Gamma(t)$,

$$[\![f]\!](\boldsymbol{x},t) = f^+(\boldsymbol{x},t) - f^-(\boldsymbol{x},t), \qquad \boldsymbol{x} \in \Gamma(t). \tag{3.5.3}$$

We will apply this to problems in which $\Gamma(t)$ is a contact discontinuity, i.e. for which the density and tangential velocity may experience a nonzero jump across the interface:

$$[\![\rho]\!] \neq 0, \qquad [\![\boldsymbol{u}\cdot\boldsymbol{\tau}]\!] \neq 0. \tag{3.5.4}$$

Let $\boldsymbol{Z}(s,t) = (X(s,t), Y(s,t))$, $s \in \mathbb{R}$, be a regular parametrization of the interface $\Gamma(t)$, and define

$$\mu(s,t) = \partial_s \boldsymbol{Z}(s,t)\cdot[\![\boldsymbol{u}]\!](\boldsymbol{Z}(s,t),t), \qquad \boldsymbol{U}(s,t) = \tfrac{1}{2}(\boldsymbol{u}^+ + \boldsymbol{u}^-)(\boldsymbol{Z}(s,t),t),$$
$$\alpha(s,t) = [\![\rho]\!](\boldsymbol{Z}(s,t),t), \qquad \bar{\rho}(s,t) = \tfrac{1}{2}(\rho^+ + \rho^-)(\boldsymbol{Z}(s,t),t).$$

3.5.2 The continuous-singular decomposition

Suppose once again that the velocity $\boldsymbol{u}(\boldsymbol{x},t)$ is regarded as a piecewise function defined a.e. on $\mathbb{R}^2$,

$$\boldsymbol{u}(\boldsymbol{x},t) = \begin{cases} \boldsymbol{u}^+(\boldsymbol{x},t), & \boldsymbol{x} \in \Omega^+(t), \\ \boldsymbol{u}^-(\boldsymbol{x},t), & \boldsymbol{x} \in \Omega^-(t), \end{cases}$$

and similarly for density $\rho(\boldsymbol{x},t)$, energy $e(\boldsymbol{x},t)$, and pressure $p(\boldsymbol{x},t)$. The continuity conditions (3.5.2) ensure that the Euler equations (3.5.1) are satisfied weakly in $\mathbb{R}^2$, but the jumps in density and tangential velocity cause derivatives of the state variables to contain distributional singularities. For example, the vorticity $\nabla\times\boldsymbol{u}$ can be computed classically in each phase,

$$\omega^\pm = \nabla\times\boldsymbol{u}^\pm, \qquad \boldsymbol{x} \in \Omega^\pm(t),$$

but exhibits a distributional part supported on the free surface $\Gamma(t)$: for any test function $\phi \in C_c^\infty(\mathbb{R}^2)$, one has

$$\begin{aligned}\langle \nabla \times \boldsymbol{u}, \phi \rangle &= -\int_{\mathbb{R}^2} \boldsymbol{u} \cdot \nabla^\perp \phi \\ &= -\int_{\Omega^+} \boldsymbol{u}^+ \cdot \nabla^\perp \phi - \int_{\Omega^-} \boldsymbol{u}^- \cdot \nabla^\perp \phi \\ &= \int_{\Omega^+} \omega^+ \phi - \int_\Gamma \boldsymbol{u}^+ \cdot \boldsymbol{\tau} \phi + \int_{\Omega^-} \omega^- \phi + \int_\Gamma \boldsymbol{u}^- \cdot \boldsymbol{\tau} \phi, \\ &= \int_{\Omega^+} \omega^+ \phi + \int_{\Omega^-} \omega^- \phi - \int_\Gamma [\![\boldsymbol{u} \cdot \boldsymbol{\tau}]\!] \phi.\end{aligned}$$

We may write this as

$$\nabla \times \boldsymbol{u}(\boldsymbol{x}, t) = \omega(\boldsymbol{x}, t) - \int_{\mathbb{R}} \mu(s, t) \delta[\boldsymbol{x} - \boldsymbol{Z}(s, t)] ds, \tag{3.5.5}$$

where ω is the piecewise-defined classical vorticity from each phase,

$$\omega(\boldsymbol{x}, t) = \begin{cases} \omega^+(\boldsymbol{x}, t), & \boldsymbol{x} \in \Omega^+(t), \\ \omega^-(\boldsymbol{x}, t), & \boldsymbol{x} \in \Omega^-(t), \end{cases}$$

and δ is the Dirac distribution. Let us compute the curl of the momentum equation (3.5.1b) by integrating against a test function of the form $\boldsymbol{\phi} = \nabla^\perp f$, where $\nabla^\perp = (\partial_y, -\partial_x)$ and $f \in C_c^\infty(\mathbb{R}^2)$:

$$\begin{aligned}0 &= \int_{\mathbb{R}^2} \big(\partial_t(\rho \boldsymbol{u}) + \nabla \cdot (\rho \boldsymbol{u} \otimes \boldsymbol{u}) + \nabla p\big) \cdot \boldsymbol{\phi} \\ &= \int_{\Omega^+} \big(\partial_t(\rho^+ \boldsymbol{u}^+) + \nabla \cdot (\rho^+ \boldsymbol{u}^+ \otimes \boldsymbol{u}^+) + \nabla p^+\big) \cdot \boldsymbol{\phi} \\ &\qquad + \int_{\Omega^-} \big(\partial_t(\rho^- \boldsymbol{u}^-) + \nabla \cdot (\rho^- \boldsymbol{u}^- \otimes \boldsymbol{u}^-) + \nabla p^-\big) \cdot \boldsymbol{\phi} \\ &= \int_\Gamma \big(\partial_t(\rho^+ \boldsymbol{u}^+) + \nabla \cdot (\rho^+ \boldsymbol{u}^+ \otimes \boldsymbol{u}^+) + \nabla p^+\big) \cdot \boldsymbol{\tau} f \\ &\qquad - \int_{\Omega^+} \rho^+ \big(\partial_t \omega^+ + \boldsymbol{u}^+ \cdot \nabla \boldsymbol{\omega}^+ + \boldsymbol{\omega}^+ \operatorname{div} \boldsymbol{u}^+ + \tfrac{\nabla \rho^+ \times \nabla p^+}{(\rho^+)^2}\big) f \\ &\qquad - \int_\Gamma \big(\partial_t(\rho^+ \boldsymbol{u}^+) + \nabla \cdot (\rho^+ \boldsymbol{u}^+ \otimes \boldsymbol{u}^+) + \nabla p^+\big) \cdot \boldsymbol{\tau} f \\ &\qquad - \int_{\Omega^-} \rho^- \big(\partial_t \omega^- + \boldsymbol{u}^- \cdot \nabla \omega^- + \omega^- \operatorname{div} \boldsymbol{u}^- + \tfrac{\nabla \rho^- \times \nabla p^-}{(\rho^-)^2}\big) f\end{aligned}$$

$$= \int_\Gamma [\![\rho(\partial_t \boldsymbol{u} + \boldsymbol{u}\cdot\nabla\boldsymbol{u}) + \nabla p]\!]\cdot\boldsymbol{\tau} f - \int_{\mathbb{R}^2} \rho\big(\partial_t\omega + \boldsymbol{u}\cdot\nabla\omega + \omega\,\mathrm{div}\,\boldsymbol{u} + \tfrac{\nabla\rho\times\nabla p}{\rho^2}\big) f$$

This yields the standard vorticity equation—the 'continuous part'—in each bulk,

$$\partial_t\omega^\pm + \boldsymbol{u}^\pm\cdot\nabla\omega^\pm + \omega^\pm\,\mathrm{div}\,\boldsymbol{u}^\pm + \frac{\nabla\rho^\pm\times\nabla p^\pm}{(\rho^\pm)^2} = 0, \qquad \boldsymbol{x}\in\Omega^\pm(t), \tag{3.5.6}$$

and the continuity condition—the 'singular part'—on the free surface $\Gamma(t)$,

$$[\![\rho(\partial_t\boldsymbol{u} + \boldsymbol{u}\cdot\nabla\boldsymbol{u})\cdot\boldsymbol{\tau} + \partial_\tau p]\!] = 0, \qquad \boldsymbol{x}\in\Gamma(t).$$

The singular part simplifies to

$$\bar\rho[\![(\partial_t\boldsymbol{u} + \boldsymbol{u}\cdot\nabla\boldsymbol{u})\cdot\boldsymbol{\tau}]\!]\circ\boldsymbol{Z} + \alpha\overline{(\partial_t\boldsymbol{u} + \boldsymbol{u}\cdot\nabla\boldsymbol{u})\cdot\boldsymbol{\tau}}\circ\boldsymbol{Z} + [\![\partial_\tau p]\!]\circ\boldsymbol{Z} = 0,$$

where the overbar denotes the average value on $\Gamma(t)$. After a tedious but straightforward computation, we find that

$$\begin{aligned}
&[\![(\partial_t\boldsymbol{u} + \boldsymbol{u}\cdot\nabla\boldsymbol{u})\cdot\boldsymbol{\tau}]\!]\circ\boldsymbol{Z} = \partial_t\mu,\\
&\overline{(\partial_t\boldsymbol{u} + \boldsymbol{u}\cdot\nabla\boldsymbol{u})\cdot\boldsymbol{\tau}}\circ\boldsymbol{Z} = \partial_t(\boldsymbol{U}\cdot\partial_s\boldsymbol{Z}) - \tfrac{1}{2}|\boldsymbol{U}|^2 + \tfrac{1}{8}|\partial_s\boldsymbol{Z}|^{-2}\mu^2.
\end{aligned}$$

Hence, the evolution equation for μ takes the form

$$\partial_t\mu = \left(\frac{\rho^+-\rho^-}{\rho^++\rho^-}\circ\boldsymbol{Z}\right)\left(-\partial_t(\boldsymbol{U}\cdot\partial_s\boldsymbol{Z}) + |\boldsymbol{U}|^2 - \tfrac{1}{4}\frac{\mu^2}{|\partial_s\boldsymbol{Z}|^2}\right) - \frac{2[\![\partial_\tau p]\!]}{\rho^++\rho^-}\circ\boldsymbol{Z} \tag{3.5.7}$$

We then define the *Atwood number*,

$$A = \frac{\rho^+-\rho^-}{\rho^++\rho^-}\circ\boldsymbol{Z} = \frac{\alpha}{2\bar\rho},$$

which is now a function of space and time.

3.5.3 The full multiscale system

The continuous-singular decomposition of vorticity yields a corresponding decomposition of velocity. In particular, following Ramani and Shkoller (2020) we decompose the velocity into an incompressible, irrotational field $\bar{\boldsymbol{u}}$, and a compressible velocity field $\tilde{\boldsymbol{u}}$. The incompressible velocity satisfies the elliptic problem

$$\nabla \cdot \bar{\boldsymbol{u}} = 0, \qquad \nabla \times \bar{\boldsymbol{u}} = \int_{\mathbb{R}} \mu(s,t)\delta_{\boldsymbol{Z}(s,t)} ds, \tag{3.5.8}$$

where $\delta_{\boldsymbol{x}_0}(\boldsymbol{x}) = \delta(\boldsymbol{x} - \boldsymbol{x}_0)$, which is solved via the Birkhoff-Rott integral. We shall solve for the Eulerian variables $(\rho, \tilde{\boldsymbol{u}}, e)$, and the interfacial variables $(\boldsymbol{Z}, \mu)$. They satisfy the evolution equations

$$\partial_t \rho + \nabla \cdot (\rho \tilde{\boldsymbol{u}}) = -\nabla \cdot (\rho \bar{\boldsymbol{u}}) \tag{3.5.9a}$$

$$\partial_t(\rho \tilde{\boldsymbol{u}}) + \nabla \cdot (\rho \tilde{\boldsymbol{u}} \otimes \tilde{\boldsymbol{u}}) + \nabla p = -\partial_t(\rho \bar{\boldsymbol{u}}) - \nabla \cdot (\rho \bar{\boldsymbol{u}} \otimes \bar{\boldsymbol{u}} + \rho \bar{\boldsymbol{u}} \otimes \tilde{\boldsymbol{u}} + \rho \tilde{\boldsymbol{u}} \otimes \bar{\boldsymbol{u}}) \tag{3.5.9b}$$

$$\partial_t(\rho e) + \nabla \cdot ((\rho e + p)\tilde{\boldsymbol{u}}) = -\nabla \cdot ((\rho e + p)\bar{\boldsymbol{u}}) \tag{3.5.9c}$$

$$\partial_t \mu = A \partial_s (|\boldsymbol{U}|^2 - \tfrac{1}{4}|\partial_s \boldsymbol{Z}|^{-2}\mu^2) + \tfrac{2}{\bar{\rho}}[\![\partial_\tau p]\!] \tag{3.5.9d}$$

$$\partial_t \boldsymbol{Z} = \boldsymbol{U}, \tag{3.5.9e}$$

where

$$\boldsymbol{U}(s,t) = \frac{1}{2\pi} \int_{\mathbb{R}} \frac{[\boldsymbol{Z}(s',t) - \boldsymbol{Z}(s,t)]^\perp}{\delta^2 + |\boldsymbol{Z}(s',t) - \boldsymbol{Z}(s,t)|^2} \mu(s',t) ds' + \tilde{\boldsymbol{u}}(\boldsymbol{Z}(s,t),t)$$

and

$$A(s,t) = \frac{\rho^+(\boldsymbol{Z}(s,t),t) - \rho^-(\boldsymbol{Z}(s,t),t)}{\rho^+(\boldsymbol{Z}(s,t),t) + \rho^-(\boldsymbol{Z}(s,t),t)}.$$

Allowing the Atwood number to vary in space and time is the key feature of our method which yields modeling improvements over the multiscale method of Ramani and Shkoller (2020). We have provided a straightforward and rigorous derivation of (3.5.9) from the full compressible Euler equations,

3.5.4 Boundary conditions for the Birkhoff-Rott integral

The integral kernel $K(\boldsymbol{x}) = \frac{1}{2\pi}\frac{\boldsymbol{x}^\perp}{|\boldsymbol{x}|^2}$ gives the velocity generated by a single point vortex of unit strength placed at the origin in $\mathbb{R}^2$. A continuum of point vortices placed along the curve $\Gamma(t)$ with density $\mu(s,t)$ results in the Birkhoff-Rott velocity,

$$\bar{\boldsymbol{u}}(\boldsymbol{x},t) = \int_{\mathbb{R}} K[\boldsymbol{x} - \boldsymbol{Z}(s,t)]\mu(s,t)ds.$$

The effect of solid boundaries in the domain is computed using the method of images. For example, a point vortex of unit strength at a point $\boldsymbol{x}_0 = (x_0, y_0)$ in the right half-plane $\{x \geqslant 0\}$ with a solid boundary at $x = 0$ generates the velocity

$$K(\boldsymbol{x}, \boldsymbol{x}_0) = \frac{1}{2\pi}\frac{(\boldsymbol{x} - \boldsymbol{x}_0)^\perp}{|\boldsymbol{x} - \boldsymbol{x}_0|^2} - \frac{1}{2\pi}\frac{(\boldsymbol{x} - \boldsymbol{x}_0')^\perp}{|\boldsymbol{x} - \boldsymbol{x}_0'|^2},$$

where $\boldsymbol{x}_0' = (-x_0, y_0)$ is the reflection of $\boldsymbol{x}_0$ across the line $\{x = 0\}$. In this work, we will only consider rectangular domains of the form $\Omega = [0, L_x] \times [0, L_y]$, with each edge of the rectangle subject to either reflecting (no-penetration) boundary conditions or nonreflecting (free-flow) boundary conditions.

For planar RT and RM instability problems, we impose reflecting boundary conditions on the side boundaries, and nonreflecting boundary conditions at the top and bottom boundaries. Computing the velocity from a point vortex located at $\boldsymbol{x}_0 \in \Omega$ therefore requires the summation of infinitely many periodic images:

$$K(\boldsymbol{x}, \boldsymbol{x}_0) = \frac{1}{2\pi}\sum_{n\in\mathbb{Z}} \frac{(\boldsymbol{x} - \boldsymbol{x}_n)^\perp}{|\boldsymbol{x} - \boldsymbol{x}_n|^2} - \frac{(\boldsymbol{x} - \boldsymbol{x}_n')^\perp}{|\boldsymbol{x} - \boldsymbol{x}_n'|^2},$$

where $\boldsymbol{x}_n = (x_0 + 2nL_x, y_0)$ and $\boldsymbol{x}_n' = (-x_0 + 2nL_x, y_0)$. This summation can be performed analytically, resulting in

$$\begin{aligned} K(\boldsymbol{x}, \boldsymbol{x}_0) = &\frac{1}{4L_x}\frac{\sinh(\pi(y - y_0)/L_x)\boldsymbol{e}_x - \sin(\pi(x - x_0)/L_x)\boldsymbol{e}_y}{\cosh(\pi(y - y_0)/L_x) - \cos(\pi(x - x_0)/L_x)} \\ &- \frac{1}{4L_x}\frac{\sinh(\pi(y - y_0)/L_x)\boldsymbol{e}_x - \sin(\pi(x + x_0)/L_x)\boldsymbol{e}_y}{\cosh(\pi(y - y_0)/L_x) - \cos(\pi(x + x_0)/L_x)}. \end{aligned}$$

For the radial Sod explosion problem, we employ no-penetration boundary conditions at the left and bottom edges ($x = 0$ and $y = 0$) and free-flow boundary conditions at the right and top edges. This results in a four-term kernel,

$$K(\boldsymbol{x}, \boldsymbol{x}_0) = \frac{1}{2\pi}\frac{(\boldsymbol{x}-\boldsymbol{x}_0)^\perp}{|\boldsymbol{x}-\boldsymbol{x}_0|^2} - \frac{1}{2\pi}\frac{(\boldsymbol{x}-\boldsymbol{x}_0')^\perp}{|\boldsymbol{x}-\boldsymbol{x}_0'|^2} + \frac{1}{2\pi}\frac{(\boldsymbol{x}+\boldsymbol{x}_0)^\perp}{|\boldsymbol{x}+\boldsymbol{x}_0|^2} - \frac{1}{2\pi}\frac{(\boldsymbol{x}+\boldsymbol{x}_0')^\perp}{|\boldsymbol{x}+\boldsymbol{x}_0'|^2},$$

where $\boldsymbol{x}_0' = (-x_0, y_0)$.

With the appropriate kernel in hand, we can compute the Birkhoff-Rott velocity as

$$\bar{\boldsymbol{u}}(\boldsymbol{x}, t) = \int_0^{L_x} K\big(\boldsymbol{x}, \boldsymbol{Z}(s,t)\big)\mu(s,t)ds,$$

where $\{\boldsymbol{Z}(s,t) : 0 \leqslant s \leqslant L_x\}$ parametrizes the material interface $\Gamma(t) \subseteq \Omega$. For numerical computations, we regularize the free-space kernel and its images by introducing a small positive number δ, and defining

$$K^\delta(\boldsymbol{x}) = \frac{1}{2\pi}\frac{\boldsymbol{x}^\perp}{\delta^2 + |\boldsymbol{x}|^2}.$$

For the periodized kernel, the regularizeation is given by

$$\begin{aligned} K^\delta(\boldsymbol{x}, \boldsymbol{x}_0) = &\frac{1}{4L_x}\frac{\sinh(\pi(y-y_0)/L_x)\boldsymbol{e}_x - \sin(\pi(x-x_0)/L_x)\boldsymbol{e}_y}{\delta^2 + \cosh(\pi(y-y_0)/L_x) - \cos(\pi(x-x_0)/L_x)} \\ &- \frac{1}{4L_x}\frac{\sinh(\pi(y-y_0)/L_x)\boldsymbol{e}_x - \sin(\pi(x+x_0)/L_x)\boldsymbol{e}_y}{\delta^2 + \cosh(\pi(y-y_0)/L_x) - \cos(\pi(x+x_0)/L_x)}. \end{aligned}$$

3.6 Numerical Method

The multiscale system is discretized using a simplified WENO scheme for the background compressible flow, and a fourth-order finite difference method for the interfacial dynamics. The presence of sharp gradients in the flow necessitate the use of some form of artificial viscosity to maintain numerical stability in the background flow. We employ the so-called *C-method* artificial viscosity of Ramani et al. (2019a,b), which couples the Euler equations to a system of reaction-diffusion equations which localize the diffusion to small regions where the density gradients are large (e.g. shocks and contacts). Moreover, we employ the *anisotropic C-method* to smooth out tangential oscillations along contact discontinuities without smearing them out. The compressible part of the

multiscale system can be written in conservation form as

$$\partial_t \boldsymbol{Q} + \partial_x \boldsymbol{F}(\boldsymbol{Q}) + \partial_y \boldsymbol{G}(\boldsymbol{Q}) = \boldsymbol{f} + \boldsymbol{D},$$

where the state variables and fluxes are given by,

$$\boldsymbol{Q} = \begin{pmatrix} \rho \\ \rho\tilde{u} \\ \rho\tilde{v} \\ \rho e \end{pmatrix}, \qquad \boldsymbol{F} = \begin{pmatrix} \rho(\bar{u}+\tilde{u}) \\ \rho(\bar{u}+\tilde{u})^2 + p \\ \rho(\bar{u}+\tilde{u})(\bar{v}+\tilde{v}) \\ (\rho e + p)(\bar{u}+\tilde{u}) \end{pmatrix}, \qquad \boldsymbol{G} = \begin{pmatrix} \rho(\bar{v}+\tilde{v}) \\ \rho(\bar{u}+\tilde{u})(\bar{v}+\tilde{v}) \\ \rho(\bar{v}+\tilde{v})^2 + p \\ (\rho e + p)(\bar{v}+\tilde{v}) \end{pmatrix},$$

and the forcing functions are

$$\boldsymbol{f} = \begin{pmatrix} 0 \\ -\partial_t(\rho\bar{u}) \\ -\partial_t(\rho\bar{v}) - \rho g \\ -\rho g(\bar{v}+\tilde{v}) \end{pmatrix}, \qquad \boldsymbol{D} = \begin{pmatrix} 0 \\ \tilde{\beta}_u \nabla\cdot(\rho C \nabla u) + \tilde{\alpha}\nabla\cdot(\rho(\boldsymbol{C}\otimes\boldsymbol{C})\nabla u) \\ \tilde{\beta}_u \nabla\cdot(\rho C \nabla u) + \tilde{\alpha}\nabla\cdot(\rho(\boldsymbol{C}\otimes\boldsymbol{C})\nabla v) \\ \tilde{\beta}_e \nabla\cdot(\rho C \nabla e) \end{pmatrix}.$$

The scalar and vector C-functions, C and $\boldsymbol{C} = (C^x, C^y)$, satisfy the parabolic equations

$$\begin{aligned} \tfrac{1}{S(\boldsymbol{Q})}\partial_t C + \tfrac{1}{\varepsilon\Delta x} C - \kappa(\partial_x^2 C + \partial_y^2 C) &= |\nabla\rho|\chi_{\{\operatorname{div} u<0\}}, \\ \tfrac{1}{S(\boldsymbol{Q})}\partial_t \boldsymbol{C} + \tfrac{1}{\varepsilon\Delta x} \boldsymbol{C} - \kappa(\partial_x^2 \boldsymbol{C} + \partial_y^2 \boldsymbol{C}) &= \nabla\rho^{\perp}, \end{aligned}$$

where $S(\boldsymbol{Q}) = \max(|\boldsymbol{u}| + c)$ is the maximum wave speed of the flow, and the parameters $(\tilde{\alpha}, \tilde{\beta}_u, \tilde{\beta}_e)$ are given by

$$\tilde{\alpha} = \frac{\alpha\Delta x^2}{\max|\boldsymbol{C}|}, \qquad \tilde{\beta}_u = \frac{\beta_u \Delta x^2}{\max C}, \qquad \tilde{\beta}_e = \frac{\beta_e \Delta x^2}{\max C},$$

with α, β_u, β_e constant and independent of Δx. The compression switch $\chi_{\{\operatorname{div} u<0\}}$ ensures that the isotropic diffusion is only active near shock waves, keeping contact discontinuities sharp.

3.6.1 Spatial discretization

Let $\Omega = [0, L_x] \times [0, L_y]$ denote our computational domain, and define

$$\boldsymbol{x}_{i,j} = (x_i, y_j) = (i\Delta x, j\Delta y)\,, \qquad\qquad 0 \leqslant i < N_x,\, 0 \leqslant j < N_y,$$

where $\Delta x = \frac{L_x}{N_x - 1}$ and $\Delta y = \frac{L_y}{N_y - 1}$. The conservative variables $\boldsymbol{Q}(\boldsymbol{x}, t)$ are discretized on this two-dimensional grid as

$$\boldsymbol{Q}_{i,j}(t) = \boldsymbol{Q}(\boldsymbol{x}_{i,j}, t).$$

Similarly, we define $s_k = k\Delta s$ for $k = 0, 1, \ldots, N_z - 1$, where $\Delta s = \frac{L_x}{N_z - 1}$. The interfacial variables are discretized on this one-dimensional grid as

$$\boldsymbol{Z}_k(t) = \boldsymbol{Z}(s_k, t), \qquad\qquad \mu_k(t) = \mu(s_k, t), \qquad\qquad 0 \leqslant k < N_z.$$

3.6.2 The continuous part

A semidiscrete approximation for the conservative variables $\boldsymbol{Q}_{i,j}$ is given by

$$\frac{d}{dt}\boldsymbol{Q}_{i,j} + \frac{\boldsymbol{F}_{i+\frac{1}{2},j} - \boldsymbol{F}_{i-\frac{1}{2},j}}{\Delta x} + \frac{\boldsymbol{G}_{i,j+\frac{1}{2}} - \boldsymbol{G}_{i,j-\frac{1}{2}}}{\Delta y} = \boldsymbol{f}_{i,j} + \boldsymbol{D}_{i,j}, \tag{3.6.1}$$

where $\boldsymbol{F}_{i\pm\frac{1}{2},j}$ is a simplified fifth-order WENO reconstruction of the horizontal flux $\boldsymbol{F}(\boldsymbol{Q})$ at the cell edge $(x_i \pm \frac{1}{2}\Delta x, y_j)$, and similarly for $\boldsymbol{G}_{i,j\pm\frac{1}{2}}$. We refer the reader to Ramani et al. (2019b) for a detailed description of the flux reconstruction and the discretization of the diffusive terms. At the boundary of the domain, ghost nodes are employed to enforce reflective (no-penetration) boundary conditions, or nonreflective (free-flow) boundary conditions. The incompressible velocity $\bar{\boldsymbol{u}}$ is computed using a trapezoid rule,

$$\bar{\boldsymbol{u}}_{i,j} = \left(\tfrac{1}{2} K^{\delta}\big(\boldsymbol{x}_{i,j}, \boldsymbol{Z}_0\big)\mu_0 + \sum_{k=1}^{N_z-2} K^{\delta}\big(\boldsymbol{x}_{i,j}, \boldsymbol{Z}_k\big)\mu_k + \tfrac{1}{2} K^{\delta}\big(\boldsymbol{x}_{i,j}, \boldsymbol{Z}_{N_z-1}\big)\mu_{N_z-1} \right) \Delta s,$$

where $K(\boldsymbol{x}, \boldsymbol{x}_0)$ is the appropriate integral kernel adapted to the problem geometry (see Section 3.5.4). This quadrature is in general only second-order accurate, but achieves spectral accuracy when the integrand is periodic (which occurs when we use the periodized Birkhoff-Rott kernel).

3.6.3 Computation of the Atwood number

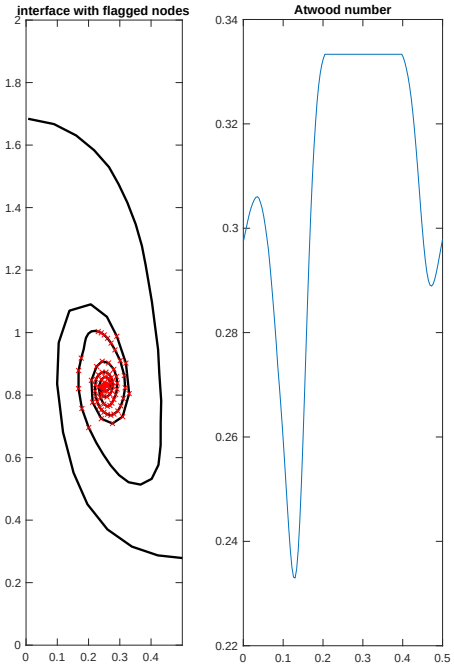
Given a quantity $f(\boldsymbol{x}, t)$ which has a nonzero jump across the material interface $\Gamma(t)$, we approximate the values of f^+ and f^- at the interface point $\boldsymbol{Z}_k(t)$ by

$$f_k^{\pm}(t) := f(\boldsymbol{Z}_k(t) + \boldsymbol{n}_k(t)\Delta x, t),$$

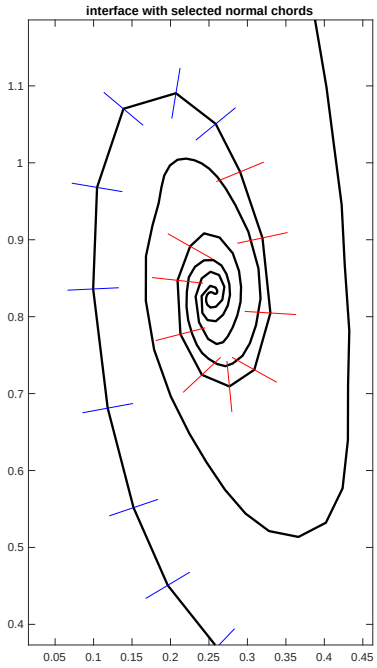
where $\boldsymbol{n}_k = \frac{\partial_s \boldsymbol{Z}_k^{\perp}}{|\partial_s \boldsymbol{Z}_k|}$ is the unit normal vector to $\Gamma(t)$ at $\boldsymbol{Z}_k$, and the evaluation of f is performed using MATLAB's bicubic interpolation routine `interp2`. This procedure is done for the density ρ, to compute the average density $\bar{\rho}_k = \frac{1}{2}(\rho_k^+ + \rho_k^-)$ and the Atwood number $A_k = (\rho_k^+ - \rho_k^-)/(\rho_k^+ + \rho_k^-)$. However, near spiral centers the background density field is not sufficiently resolved to compute an accurate density jump via interpolation, resulting in nonphysical computed Atwood number. In particular, when the interface turns over at least once inside of a computational cell, the need for subgrid-scale geometric information necessitates a novel subgrid modeling approach to compute small-scale density gradients.

Our solution is as follows: for each index $k \in \{1, 2, \ldots, N_z\}$, we test to see if the chord between $\boldsymbol{Z}_k - 2\boldsymbol{n}_k\Delta x$ and $\boldsymbol{Z}_k + 2\boldsymbol{n}_k\Delta x$ intersects the interface Γ at any point other than $\boldsymbol{Z}_k$, and if it does the Atwood number A_k is set to some user-specified value $\bar{A}$. In the case of Rayleigh-Taylor problems, this is set to the initial Atwood number across the interface, and for Richtmyer-Meshkov problems it is set to the post-shock Atwood number. We then apply a simple Gaussian smoothing to the Atwood number to avoid discontinuities. Using coarse-mesh interpolation to compute density jumps when the interface does not exhibit subgrid scale geometry is a significant improvement over the old constant-Atwood number method (see Figures 3.3–3.11), but it is only one intermediate step towards a physically accurate subgrid-scale model for compressible contact discontinuities (Pandya and Shkoller, 2025).

See Figure 3.1 for an example of the numerically computed Atwood number for the single-mode RT problem described in section 3.7.1. Figure 3.1a shows the z-model interface with red x's indicating the nodes flagged for Atwood number reassignment and the resulting computed Atwood number. Figure 3.1b shows the normal chords $(\boldsymbol{Z}_k - 2\boldsymbol{n}_k\Delta x, \boldsymbol{Z}_k + 2\boldsymbol{n}_k\Delta x)$ for selected interface points $\boldsymbol{Z}_k$. The normal chords which intersect the interface anywhere except $\boldsymbol{Z}_k$ are flagged for Atwood number reassignment, shown in red in Figure 3.1b.



(a) Interface and computed Atwood number. The red x's mark the interface points $\boldsymbol{Z}_k$ which are flagged for Atwood number reassignment ($A_k = \bar{A}$).



(b) Detail of interface showing selected normal chords ($\boldsymbol{Z}_k - 2\boldsymbol{n}_k\Delta x, \boldsymbol{Z}_k + 2\boldsymbol{n}_k\Delta x$). Chords which intersect the interface are colored in red, and those which do not are colored in blue.

Figure 3.1: Interface and Atwood number for multiscale simulation of the single-mode RT problem described in Section 3.7.1.

3.6.4 The singular part

The interfacial velocity $\boldsymbol{U}(s,t)$ is the sum of an incompressible part $\bar{\boldsymbol{U}}(s,t)$ and a compressible part $\tilde{\boldsymbol{U}}(s,t) = \tilde{\boldsymbol{u}}(\boldsymbol{Z}(s,t),t)$. The incompressible part is discretized in the same way as above, namely

$$\bar{\boldsymbol{U}}_k = \left(\tfrac{1}{2} K^\delta(\boldsymbol{Z}_k, \boldsymbol{Z}_0)\mu_0 + \sum_{l=1}^{N_z-2} K^\delta(\boldsymbol{Z}_k, \boldsymbol{Z}_l)\mu_l + \tfrac{1}{2} K^\delta(\boldsymbol{Z}_k, \boldsymbol{Z}_{N_z-1})\mu_{N_z-1} \right) \Delta s.$$

The compressible part $\tilde{\boldsymbol{U}}_k$ is computed by interpolating the background velocity $\tilde{\boldsymbol{u}}_{i,j}$ onto the interface point $\boldsymbol{Z}_k$ using MATLAB's bicubic interpolation routine `interp2`. The semidiscrete z-model equations are

$$\frac{d}{dt}\boldsymbol{Z}_k = \boldsymbol{U}_k, \qquad \frac{d}{dt}\mu_k = A_k \partial_s (|\boldsymbol{U}_k|^2 - \tfrac{1}{4}\tilde{\gamma}_k^2 - 2gY_k)_k - \tfrac{2}{\bar{\rho}_k}[\![\partial_\tau p]\!]_k + \nu \Delta x^2 \partial_s^2 \mu_k,$$

where

$$\tilde{\gamma} = (1 - \nu\Delta x\partial_s^2)^{-1}\frac{\mu}{|\partial_s \boldsymbol{Z}|}.$$

The interfacial derivative operators ∂_s and ∂_s^2 are discretized by fourth- and second-order centered difference approximations, respectively:

$$\partial_s f_k = \frac{f_{k-2} - 8f_{k-1} + 8f_{k+1} - f_{k+2}}{12\Delta s}, \qquad \partial_s^2 f_k = \frac{f_{k-1} - 2f_k + f_{k+1}}{\Delta s^2}.$$

3.6.5 Temporal discretization

The temporal domain $[0, T)$ is approximated by a sequence of times $0 = t^0 < t^1 < \cdots < t^N = T$, where each timestep $\Delta t^n = t^{n+1} - t^n$ is chosen adaptively according to the CFL condition of the background compressible flow. For the conservative background flow, we employ a standard third-order TVD Runge-Kutta method for timestepping:

$$\begin{aligned}
\boldsymbol{Q}_{i,j}^{n,1} &= \boldsymbol{Q}_{i,j}^n + \Delta t^n \left(-\frac{\boldsymbol{F}_{i+\frac{1}{2},j}^n - \boldsymbol{F}_{i-\frac{1}{2},j}^n}{\Delta x} - \frac{\boldsymbol{G}_{i,j+\frac{1}{2}}^n - \boldsymbol{G}_{i,j-\frac{1}{2}}^n}{\Delta y} + \boldsymbol{f}_{i,j}^n + \boldsymbol{D}_{i,j}^n \right) \\
\boldsymbol{Q}_{i,j}^{n,2} &= \tfrac{3}{4}\boldsymbol{Q}_{i,j}^n + \tfrac{1}{4}\boldsymbol{Q}_{i,j}^{n,1} + \tfrac{1}{4}\Delta t^n \left(-\frac{\boldsymbol{F}_{i+\frac{1}{2},j}^{n,1} - \boldsymbol{F}_{i-\frac{1}{2},j}^{n,1}}{\Delta x} - \frac{\boldsymbol{G}_{i,j+\frac{1}{2}}^{n,1} - \boldsymbol{G}_{i,j-\frac{1}{2}}^{n,1}}{\Delta y} + \boldsymbol{f}_{i,j}^{n,1} + \boldsymbol{D}_{i,j}^{n,1} \right) \\
\boldsymbol{Q}_{i,j}^{n+1} &= \tfrac{1}{3}\boldsymbol{Q}_{i,j}^n + \tfrac{2}{3}\boldsymbol{Q}_{i,j}^{n,2} + \tfrac{2}{3}\Delta t^n \left(-\frac{\boldsymbol{F}_{i+\frac{1}{2},j}^{n,2} - \boldsymbol{F}_{i-\frac{1}{2},j}^{n,2}}{\Delta x} - \frac{\boldsymbol{G}_{i,j+\frac{1}{2}}^{n,2} - \boldsymbol{G}_{i,j-\frac{1}{2}}^{n,2}}{\Delta y} + \boldsymbol{f}_{i,j}^{n,2} + \boldsymbol{D}_{i,j}^{n,2} \right)
\end{aligned}$$

The fluxes and diffusive terms are recomputed at each substep, while the forcing term from the expensive Birkhoff-Rott velocity is computed only once per timestep:

$$\boldsymbol{f}_{i,j}^{n,m} = \begin{pmatrix} 0 \\ -\frac{\rho_{i,j}^n \bar{u}_{i,j}^n - \rho_{i,j}^{n-1}\bar{u}_{i,j}^{n-1}}{\Delta t} \\ -\frac{\rho_{i,j}^n \bar{v}_{i,j}^n - \rho_{i,j}^{n-1}\bar{v}_{i,j}^{n-1}}{\Delta t} - \rho_{i,j}^{n,m} g \\ -\rho_{i,j}^{n,m} g(\bar{v}_{i,j}^n + \tilde{v}_{i,j}^{n,m}) \end{pmatrix}, \qquad m = 1, 2.$$

Once the conservative variables have been updated, the interfacial variables are updated via a simple forward Euler method,

$$\begin{aligned}
\boldsymbol{Z}_k^{n+1} &= \boldsymbol{Z}_k^n + \Delta t^n \, \boldsymbol{U}_k^n, \\
\mu_k^{n+1} &= \mu_j^n + \Delta t^n \left(A_k^n \partial_s (|\boldsymbol{U}_k^n|^2 - \tfrac{1}{4}(\tilde{\gamma}_k^n)^2 - 2gY_k^n)_k - \tfrac{2}{\bar{\rho}_k^n} [\![\partial_\tau p^n]\!]_k + \nu \Delta x^2 \partial_s^2 \mu_k^n \right).
\end{aligned}$$

Note that the values of the conservative variables from the beginning of the timestep, $\boldsymbol{Q}_{i,j}^n$, are used for interpolation onto the interface. The full algorithm to obtain $(\boldsymbol{Q}_{i,j}^{n+1}, \boldsymbol{Z}_k^{n+1}, \mu_k^{n+1})$ from $(\boldsymbol{Q}_{i,j}^n, \boldsymbol{Z}_k^n, \mu_k^n)$ can be summarized as follows:

1. Compute the Birkhoff-Rott velocity $\bar{\boldsymbol{u}}_{i,j}^n$, and the time-derivative

$$\partial_t (\rho \bar{\boldsymbol{u}})_{i,j}^n = \frac{\rho_{i,j}^n \bar{\boldsymbol{u}}_{i,j}^n - \rho_{i,j}^{n-1} \bar{\boldsymbol{u}}_{i,j}^{n-1}}{\Delta t_{n-1}}.$$

2. Choose the timestep Δt^n based on the CFL condition,

$$\Delta t^n = \mathrm{CFL} \left(\frac{\Delta x}{\lambda_x} + \frac{\Delta y}{\lambda_y} \right), \qquad \lambda_x = \max(|u| + c), \; \lambda_y = \max(|v| + c).$$

3. Compute $\boldsymbol{Q}_{i,j}^{n+1}$ using a third-order Runge-Kutta step,

$$\begin{aligned}
\boldsymbol{Q}_{i,j}^{n,1} &= \boldsymbol{Q}_{i,j}^n + \Delta t^n \left(-\frac{\boldsymbol{F}_{i+\frac{1}{2},j}^n - \boldsymbol{F}_{i-\frac{1}{2},j}^n}{\Delta x} - \frac{\boldsymbol{G}_{i,j+\frac{1}{2}}^n - \boldsymbol{G}_{i,j-\frac{1}{2}}^n}{\Delta y} + \boldsymbol{f}_{i,j}^n + \boldsymbol{D}_{i,j}^n \right) \\
\boldsymbol{Q}_{i,j}^{n,2} &= \tfrac{3}{4} \boldsymbol{Q}_{i,j}^n + \tfrac{1}{4} \boldsymbol{Q}_{i,j}^{n,1} + \tfrac{1}{4} \Delta t^n \left(-\frac{\boldsymbol{F}_{i+\frac{1}{2},j}^{n,1} - \boldsymbol{F}_{i-\frac{1}{2},j}^{n,1}}{\Delta x} - \frac{\boldsymbol{G}_{i,j+\frac{1}{2}}^{n,1} - \boldsymbol{G}_{i,j-\frac{1}{2}}^{n,1}}{\Delta y} + \boldsymbol{f}_{i,j}^{n,1} + \boldsymbol{D}_{i,j}^{n,1} \right) \\
\boldsymbol{Q}_{i,j}^{n+1} &= \tfrac{1}{3} \boldsymbol{Q}_{i,j}^n + \tfrac{2}{3} \boldsymbol{Q}_{i,j}^{n,2} + \tfrac{2}{3} \Delta t^n \left(-\frac{\boldsymbol{F}_{i+\frac{1}{2},j}^{n,2} - \boldsymbol{F}_{i-\frac{1}{2},j}^{n,2}}{\Delta x} - \frac{\boldsymbol{G}_{i,j+\frac{1}{2}}^{n,2} - \boldsymbol{G}_{i,j-\frac{1}{2}}^{n,2}}{\Delta y} + \boldsymbol{f}_{i,j}^{n,2} + \boldsymbol{D}_{i,j}^{n,2} \right)
\end{aligned}$$

4. Compute the interfacial quantities A_k^n, $\bar{\rho}_k^n$, and $[\![\partial_\tau p]\!]_k^n$ from the background conserved variables $\boldsymbol{Q}_{i,j}^n$ using cubic spline interpolation (MATLAB's `interp2` routine), and use a tridiagonal solve to get $\tilde{\gamma}_k^n$ from $\mu_k^n / |\partial_s \boldsymbol{Z}_k^n|$.

5. Compute $\boldsymbol{Z}_k^{n+1}$ and μ_k^{n+1} using a forward Euler step,

$$\begin{aligned}
\boldsymbol{Z}_k^{n+1} &= \boldsymbol{Z}_k^n + \Delta t^n \, \boldsymbol{U}_k^n, \\
\mu_k^{n+1} &= \mu_j^n + \Delta t^n \left(A_k^n \partial_s (|\boldsymbol{U}_k^n|^2 - \tfrac{1}{4}(\tilde{\gamma}_k^n)^2 - 2gY_k^n)_k - \tfrac{2}{\overline{\rho}_k^n} [\![\partial_\tau p^n]\!]_k + \nu \Delta x^2 \partial_s^2 \mu_k^n \right).
\end{aligned}$$

3.7 Examples

We present a number of important numerical examples of Rayleigh-Taylor and Richtmyer-Meshkov instability using our multiscale model.

3.7.1 Single-mode Rayleigh-Taylor instability

Our first test problem is a compressible Rayleigh-Taylor problem, with a density ratio of $2:1$ and an initially sinusoidal interface. The domain size is $L_x = 0.5$ by $L_y = 2$, and the fluid is initialized at rest with density and energy given by

$$\rho_0(\boldsymbol{x}) = \begin{cases} 1, & y < h(x) \\ 2, & y \geqslant h(x) \end{cases} \qquad e_0(\boldsymbol{x}) = \frac{1}{(\gamma - 1)\rho_0(\boldsymbol{x})} \begin{cases} p_0 + g(2L_y - h(x) - y), & y < h(x) \\ p_0 + 2g(L_y - y), & y \geqslant h(x) \end{cases}$$

where the initial interface is located at $h(x) = 1 + 0.03\cos(2\pi x)$. The adiabatic index is $\gamma = 1.4$, the reference pressure is $p_0 = 2.4$, and the gravitational acceleration is $g = 0.3$. No-penetration boundary conditions are imposed at the right and left boundaries, and free-flow boundary conditions are imposed at the top and bottom. This problem is relatively low Mach number (maxing out at around $M = 0.15$) but compressible effects are still important enough to render an incompressible run inaccurate. We run up to the final time $T = 8$.

As a benchmark, we compute a high-resolution solution using just the compressible C-method code with 64×256 cells. The following table shows the parameters used for a variety of runs, and the resulting computational time.

	N_x	N_y	α	β_u	β_e	ε	κ	N_z	$\bar{A}$	δ	ν	T_{CPU}
8×32 C-method	8	32	5	0	0	2	10	–	–	–	–	6s
16×64 C-method	16	64	5	0	0	2	10	–	–	–	–	17s
64×256 C-method	64	256	5	0	0	2	10	–	–	–	–	722s
8×32 multiscale	8	32	5	0	0	2	10	64	$\frac{1}{3}$	$\frac{5}{16}$	$\frac{1}{16}$	11s
16×64 multiscale	16	64	5	0	0	2	10	128	$\frac{1}{3}$	$\frac{5}{32}$	$\frac{1}{32}$	59s

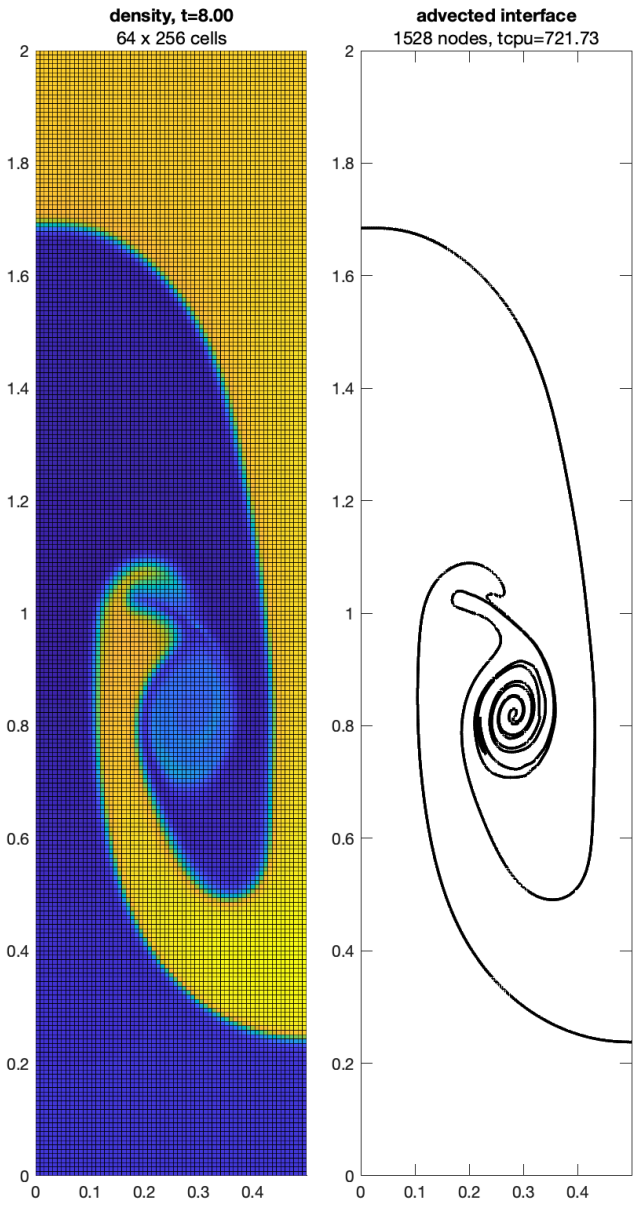
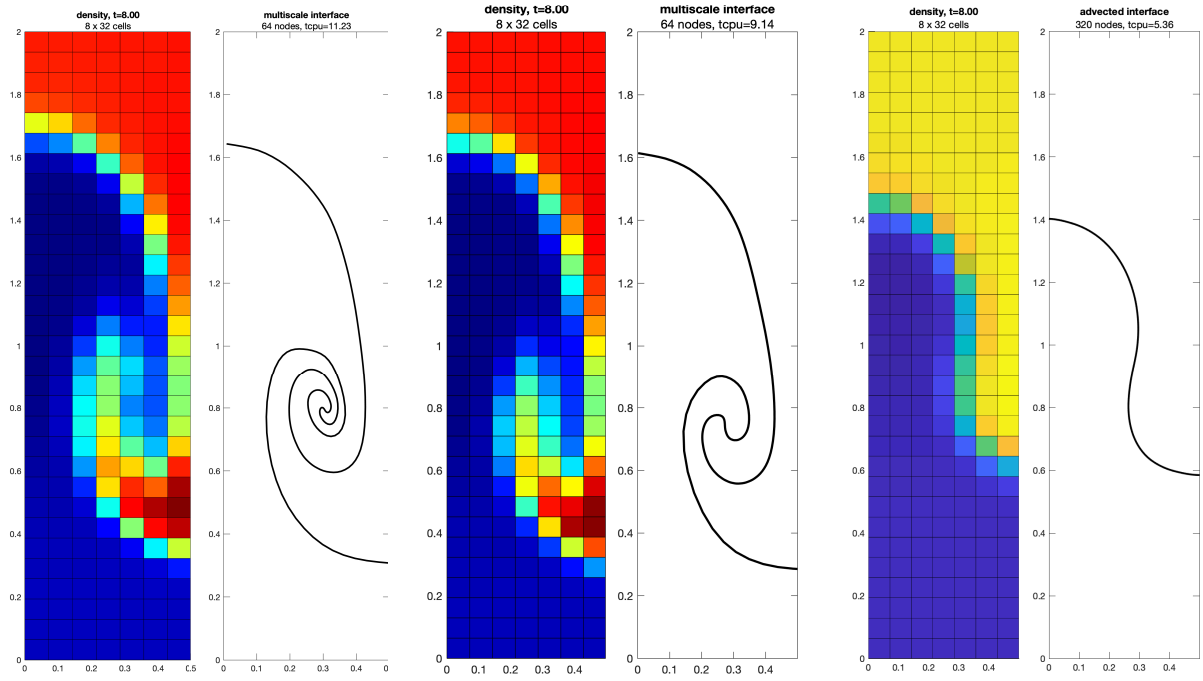


Figure 3.2: High-resolution benchmark solution for the single-mode RT problem, computed using the C-method on a 64×256 grid. The interface shown in the right-hand panel is simply advected with the fluid velocity: $\partial_t \boldsymbol{Z} = \boldsymbol{u} \circ \boldsymbol{Z}$.

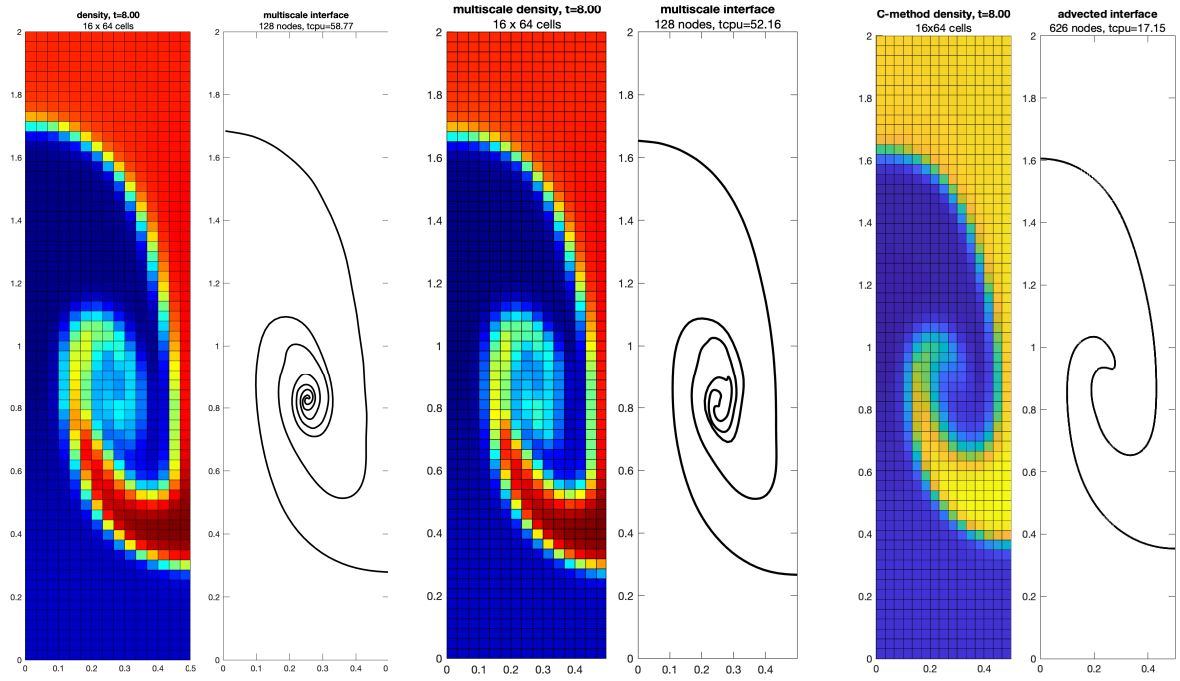


(a) Multiscale RTI simulation with variable Atwood number

(b) Multiscale RTI simulation with constant Atwood number

(c) C-method RTI simulation with no subgrid scale model

Figure 3.3: (a) Multiscale solution for the single-mode RT problem, computed using a 8×32 background grid and a 64-node interface. (b) Solution for the same problem using the method of Ramani and Shkoller. (c) C-method solution for the same problem, using the same 8×32 grid and identical parameters.



(a) Multiscale RTI simulation with variable Atwood number

(b) Multiscale RTI simulation with constant Atwood number

(c) C-method RTI simulation with no subgrid scale model

Figure 3.4: (a) Multiscale solution for the single-mode RT problem, computed using a 16×64 background grid and a 64-node interface. (b) Solution for the same problem using the method of Ramani and Shkoller. (c) C-method solution for the same problem, using the same 16×64 grid and identical parameters.

The z-model consistently underestimates the amplitude of the instability, as does the C-method at low resolution. The multiscale model with 16×64 cells accurately computes the amplitude, while also capturing the small-scale structure present in the 64×256 C-method simulation and delivering a 12x reduction in computational expense over the high-resolution benchmark. We remark that Ramani and Shkoller demonstrated that this problem can be done using their multiscale compressible-incompressible methodology, since the density varies by only around 10% from a constant on each side of the interface. They report comparable results to ours, with the exception that their high-resolution benchmark was computed with a small CFL number of 0.1, due to the presence of instabilities at higher CFL numbers. Perhaps due to different choices of artificial viscosity parameters, we did not observe such instability, and consequently were able to run all our simulations with CFL number 0.5.

3.7.2 Single-mode Richtmyer-Meshkov instability

Next, we simulate a classical shock tube Richtmyer-Meshkov problem, where a planar shock moving down the domain impacts a sinusoidal contact discontinuity. This generates vorticity at the contact, causing the contact to roll up. The domain size is $L_x = 0.5$ by $L_y = 4$, and the initial density and velocity are given by

$$\rho_0(\boldsymbol{x}) = \begin{cases} 5.04, & y > h(x) \\ 1, & y \leqslant h(x) \end{cases} \qquad \boldsymbol{u}_0(\boldsymbol{x}) = \begin{cases} -0.55063\boldsymbol{e}_y, & y > h_s \\ 0, & y \leqslant h_s \end{cases}$$

where the initial contact is located at $h(x) = 3.5 - 0.1\cos(2\pi x)$, and the initial shock is located at $h_s = 3.8$. The initial pressure is

$$p_0(\boldsymbol{x}) \begin{cases} 1.628, & y > h_s \\ 1, & y \leqslant h_s \end{cases},$$

and the initial energy is computed from the pressure, density, and velocity as

$$e_0(\boldsymbol{x}) = \frac{p_0(\boldsymbol{x})}{(\gamma - 1)\rho_0(\boldsymbol{x})} + \tfrac{1}{2}|\boldsymbol{u}_0(\boldsymbol{x})|^2.$$

The adiabatic index is $\gamma = 1.276$, and the gravitational acceleration is zero. No-penetration boundary conditions are imposed at the right and left boundaries, and free-flow boundary conditions are imposed at the top and bottom.

As a benchmark, we compute a high-resolution solution using just the compressible C-method code with 64×512 cells. The following table shows the parameters used for a variety of runs, and the resulting computational time. The 32×256 multiscale run (Figure 3.6a) exhibits equal or greater small-scale structure compared with the high-resolution64×512 C-method run (Figure 3.5), at 30% the computational expense. Moreover, the multiscale method of Ramani and Shkoller at the same resolution (Figure 3.6b) slightly underpredicts the level of interface rollup.

	N_x	N_y	α	β_u	β_e	ε	κ	N_z	$\bar{A}$	δ	ν	T_{CPU}
16×128 C-method	16	128	2	5	5	2	10	–	–	–	–	18s
32×256 C-method	32	256	2	5	5	2	10	–	–	–	–	162s
64×512 C-method	64	512	5	5	5	2	10	–	–	–	–	846s
16×128 multiscale	16	128	2	5	5	2	10	64	0.7	$\frac{1}{8}$	$\frac{1}{32}$	38s
32×256 multiscale	32	256	2	5	5	2	10	128	0.7	$\frac{1}{16}$	$\frac{1}{64}$	267s

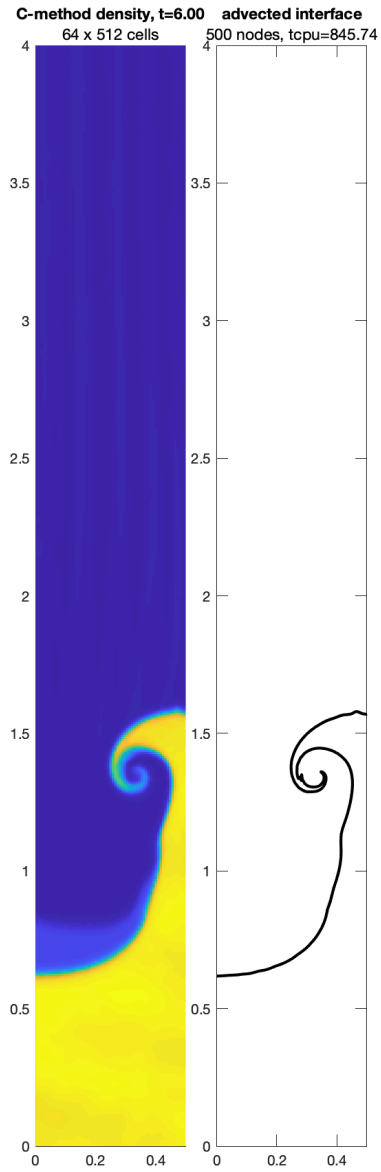
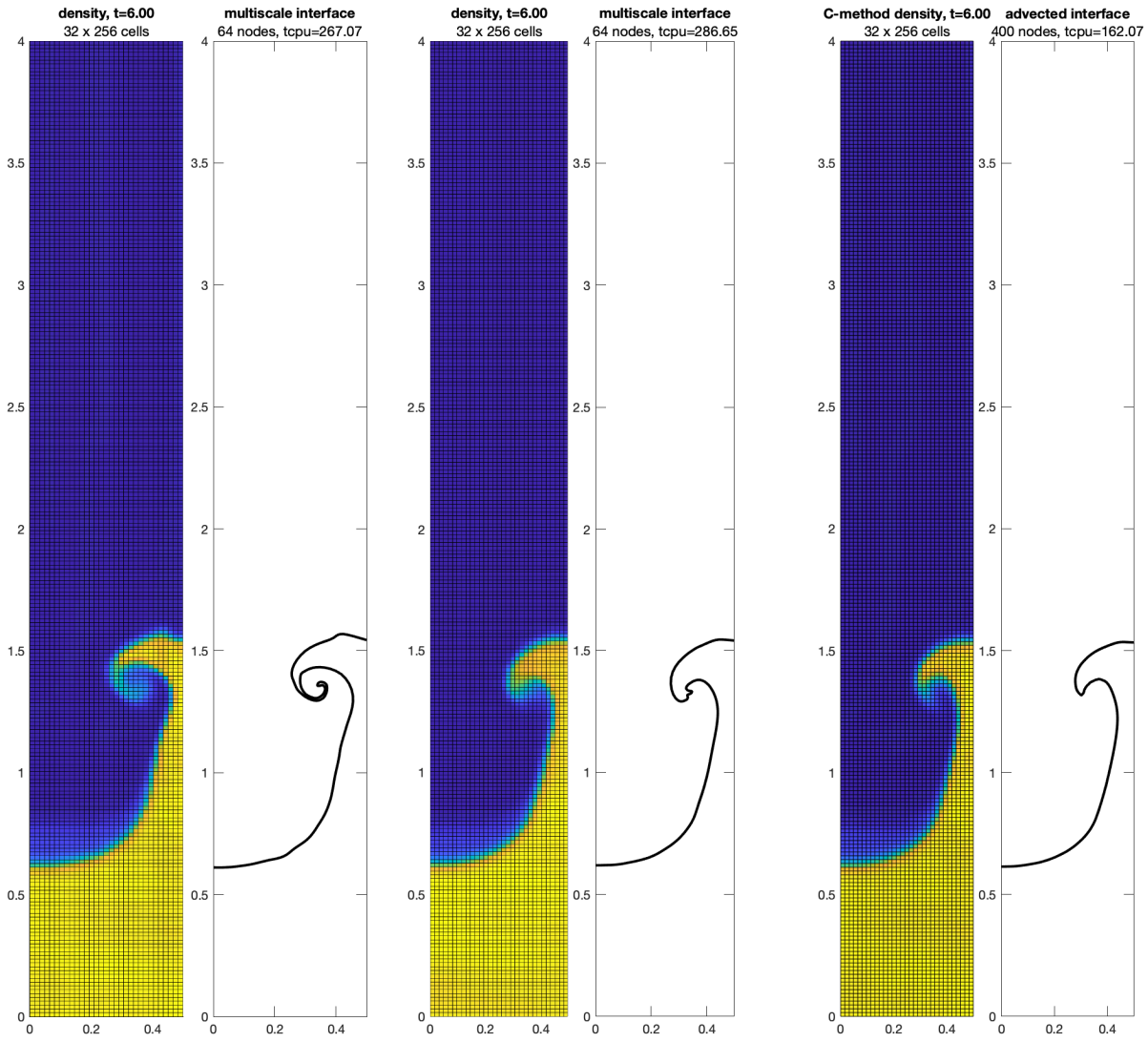


Figure 3.5: High-resolution benchmark solution for the single-mode RM problem, computed using the C-method on a 64×512 grid. The interface shown in the right-hand panel is simply advected with the fluid velocity: $\partial_t \boldsymbol{Z} = \boldsymbol{u} \circ \boldsymbol{Z}$.



(a) Multiscale RMI simulation.

(b) Multiscale RM simulation, using the method of Ramani and Shkoller.

(c) C-method RMI simulation

Figure 3.6: (a) Multiscale solution for the single-mode RM problem, computed using a 32×256 background grid and a 64-node interface. (b) Multiscale solution for the single-model RM problem, using a 32×256 background grid and a 64-node interface. (c) C-method solution for the same problem, using the same 32×256 grid and identical parameters.

3.7.3 Radial implosion/explosion problem

Our final test problem is a perturbed version of the radial Sod explosion problem. The Sod problem is a classical 1d Riemann problem with initial data

$$\rho_0(x) = \begin{cases} 1, & x < 0.4 \\ 0.125, & x \geqslant 0.4 \end{cases} \qquad u_0(x) = 0, \qquad e_0(x) = \begin{cases} 2.5, & x < 0.4 \\ 2, & x \geqslant 0.4 \end{cases}$$

with adiabatic exponent $\gamma = 1.4$. The solution consists of a shock wave and a contact discontinuity moving to the right, and a rarefaction wave moving to the left. Tracking the location and amplitude of these features is a common benchmark for one-dimensional gas dynamics codes.

We are interested in a version of this problem posed in two-dimensional cylindrical geometry:

$$\rho_0(\boldsymbol{x}) = \begin{cases} 1, & r < 0.4 \\ 0.125, & r \geqslant 0.4 \end{cases} \qquad \boldsymbol{u}_0(\boldsymbol{x}) = 0, \qquad e_0(\boldsymbol{x}) = \begin{cases} 2.5, & r < 0.4 \\ 2, & r \geqslant 0.4 \end{cases}$$

where $r = |\boldsymbol{x}|$ is the radial coordinate. Our domain is a square in the first quadrant of side length $L_x = L_y = 1.5$, with reflective boundary conditions at $x = 0$ and $y = 0$, and free-flow boundaries at $x = 1.5$ and $y = 1.5$. The solution consists of a shock wave and contact discontinuity moving radially outward from the initial discontinuity, and a rarefaction wave moving inward towards the origin. The shock wave quickly leaves the domain, and the rarefaction wave eventually reflects off the origin, leaving an evacuated region behind it. This generates a secondary shock wave traveling inward, which implodes at the origin and subsequently explodes outward. This secondary exploding shock passes through the original contact discontinuity, resulting in Richtmyer-Meshkov instability, before leaving the domain.

This problem poses a number of challenges to a compressible flow solver. The problem is radially symmetric at the initial time, and the exact solution remains so for all time. However, a rectangular grid cannot exactly capture this symmetry, and the resulting asymmetries grow in the unstable contact discontinuity. These grid-scale perturbations in the contact are amplified by the passage of the exploding shock, and a Richtmyer-Meshkov mixing zone is created. Resolving this mixing zone without creating spurious Gibbs oscillations is a challenging task: on the one hand, a

high order, low dissipation method is needed to avoid smearing out the small-scale structure in the contact and suppressing the instability; on the other hand, some numerical dissipation is needed to stabilize the shock waves, especially at the moment of implosion.

We would like to use our multiscale model to capture this RM mixing region, but there is an obstacle to doing so in the problem as described: the length scale of the perturbations in the contact are tied fundamentally to the size of the background rectangular mesh, as the initial asymmetry stems from the failure of the rectangular grid to resolve an radial function. Consequently, although the multiscale model with (for example) a 32×32 background grid can resolve the instability better than a 32×32 C-method run, the dominant wavenumbers which drive the instability in this simulation will be (roughly) 16 times larger than the dominant wavenumbers in a 512×512 C-method or multiscale run, making it difficult to compare apples to apples among simulations with different resolutions. Nevertheless, our multiscale model exhibits moderately more developed RM instability for the radial Sod problem (Figure 3.7a) compared with the results from the multiscale method of Ramani and Shkoller (2020) (Figure 3.7b). For both multiscale methods, we employ a 32×32 grid and a 1024-node interface, with a final time of $T = 6$.

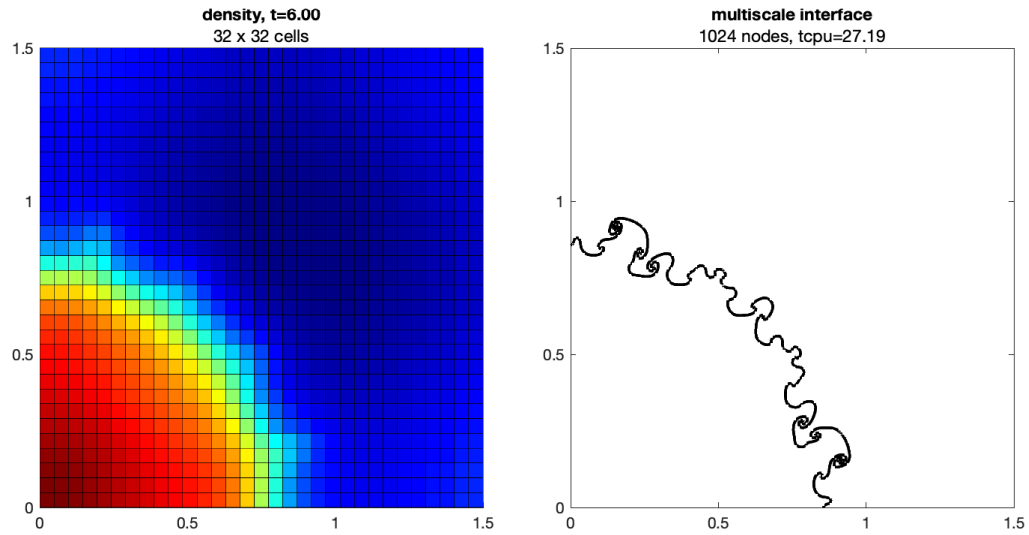
Our solution to the problem of grid-dependent scales is to "seed" the initial surface of discontinuity with an azimuthal perturbation of a fixed wavenumber that is well above grid scale. In particular, we use the initial data

$$\rho_0(\boldsymbol{x}) = \begin{cases} 1, & r < r_0(\theta) \\ 0.125, & r \geqslant r_0(\theta) \end{cases} \qquad \boldsymbol{u}_0(\boldsymbol{x}) = 0, \qquad e_0(\boldsymbol{x}) = \begin{cases} 2.5, & r < r_0(\theta) \\ 2, & r \geqslant r_0(\theta) \end{cases}$$

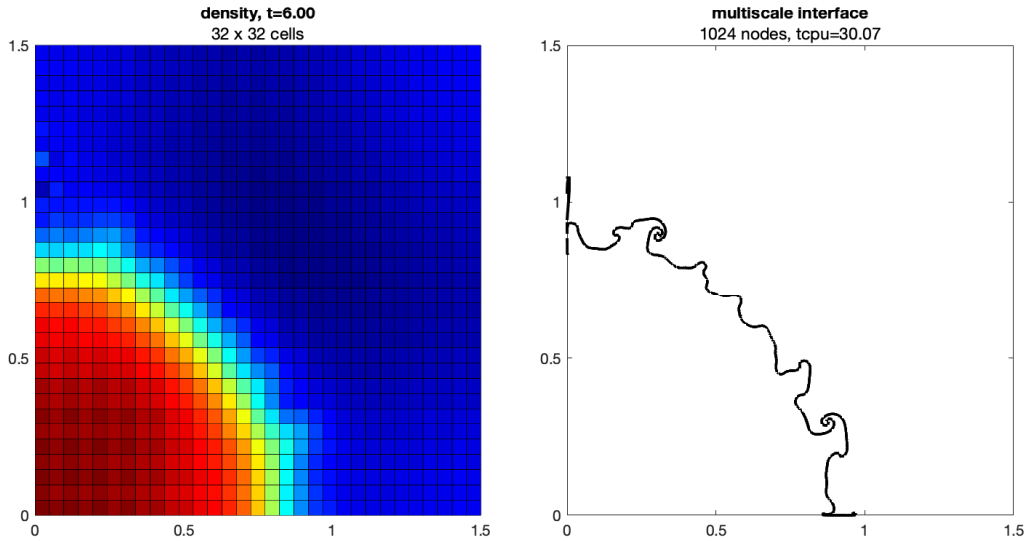
where

$$r_0(\theta) = 0.4 + 0.05\cos(16\theta).$$

The domain is once again a square with $L_x = L_y = 1.5$, and the simulation is run up to the final time $T = 6$. This initial condition results in four mushroom-shaped Richtmyer-Meshkov plumes in the first quadrant, accelerated by the secondary exploding shock wave. This provides an excellent test case for our multiscale z-model with variable density ratio—the density ratio across the contact not only varies with time as the gas contracts and expands, but also varies along the interface by up to an order of magnitude (see Figure 3.8). Comparing Figure 3.10 with Figure 3.11a, we find that



(a) The radial Sod problem (without azimuthal perturbation) using our mulstiscale model with a 32×32 background mesh and a 1024-node interface, showing the instability generated from grid-scale perturbations in the contact.



(b) The radial Sod problem (without azimuthal perturbation) using the mulstiscale model of Ramani and Shkoller (2020) with a 32×32 background mesh and a 1024-node interface, showing the instability generated from grid-scale perturbations in the contact.

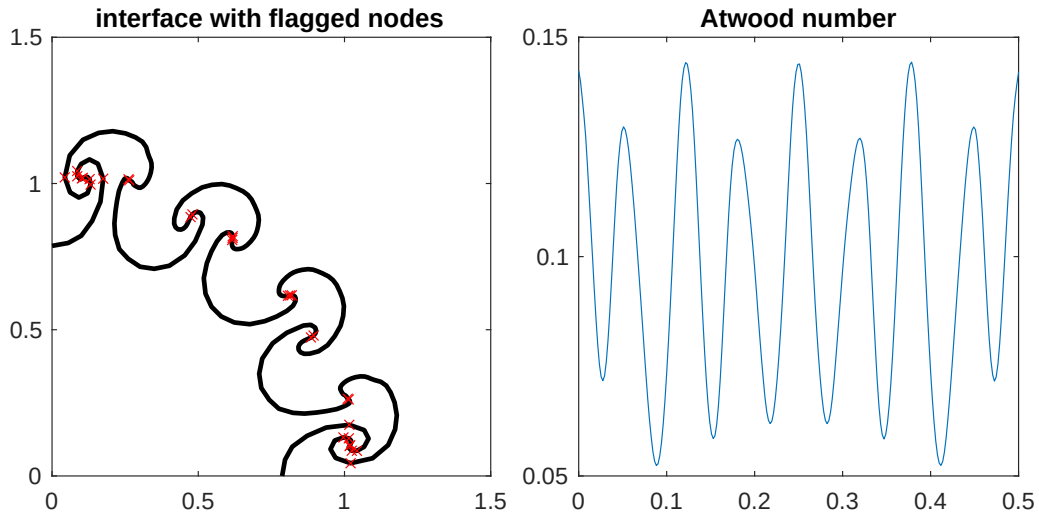


Figure 3.8: Interface with flagged nodes and numerically computed Atwood number for the perturbed Sod problem at time $t = 6$, computed using our multiscale method.

the multiscale model of Ramani and Shkoller, which uses the constant Atwood number z-model for its small-scale part, underpredicts the rollup of the contact, while our variable-density multiscale model captures the additional small-scale behavior.

The following table shows the parameters used for various runs of the perturbed Sod problem, and the resulting computation times. The 64×64 multiscale run (Figure 3.11a) captures as much small-scale structure as the 128×128 C-method run (Figure 3.9), at 60% the computational expense. Moreover, the multiscale method of Ramani and Shkoller (Figure 3.10) significantly underpredicts the interfacial rollup, barely improving upon the pure C-method simulation at the same resolution (Figure 3.11b).

	N_x	N_y	α	β_u	β_e	ε	κ	N_z	$\bar{A}$	δ	ν	T_{CPU}
64×64 C-method	64	64	2	5	5	2	10	–	–	–	–	39s
128×128 C-method	128	128	2	5	15	2	10	–	–	–	–	197s
64×64 multiscale	64	64	2	5	5	2	10	256	0.1	$\frac{1}{16}$	$\frac{1}{64}$	107s

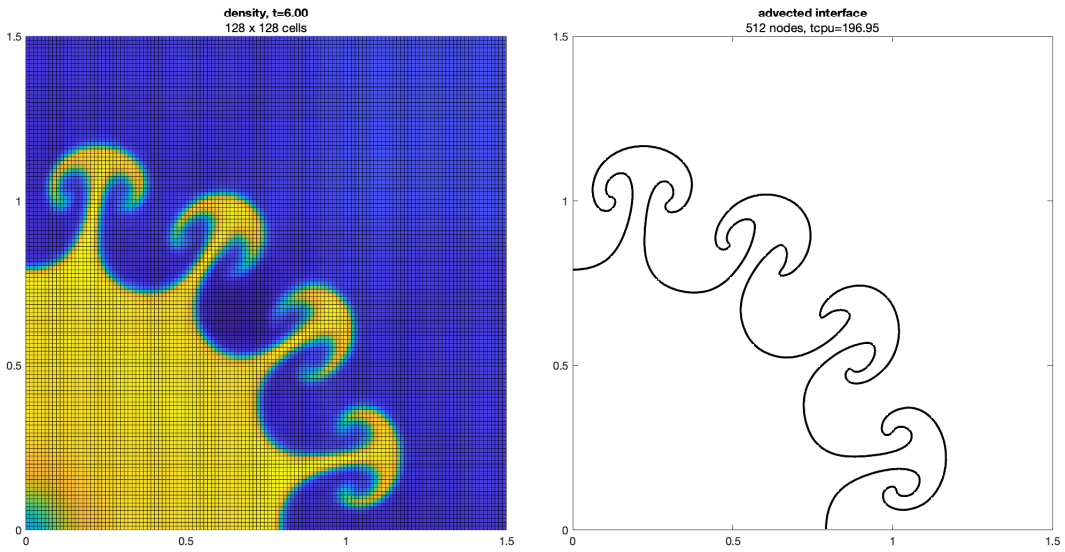


Figure 3.9: The perturbed radial Sod problem using the C-method with a 128×128 mesh.

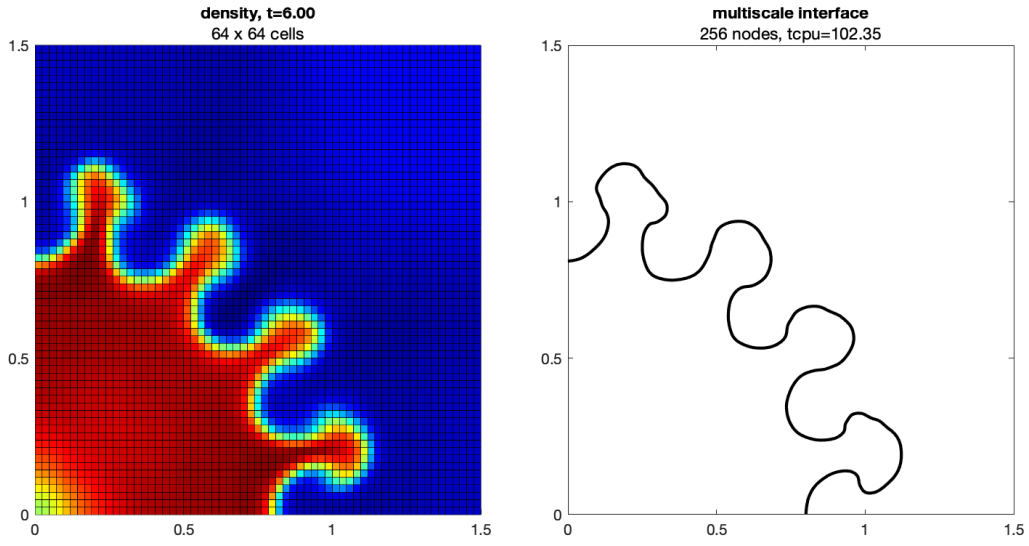
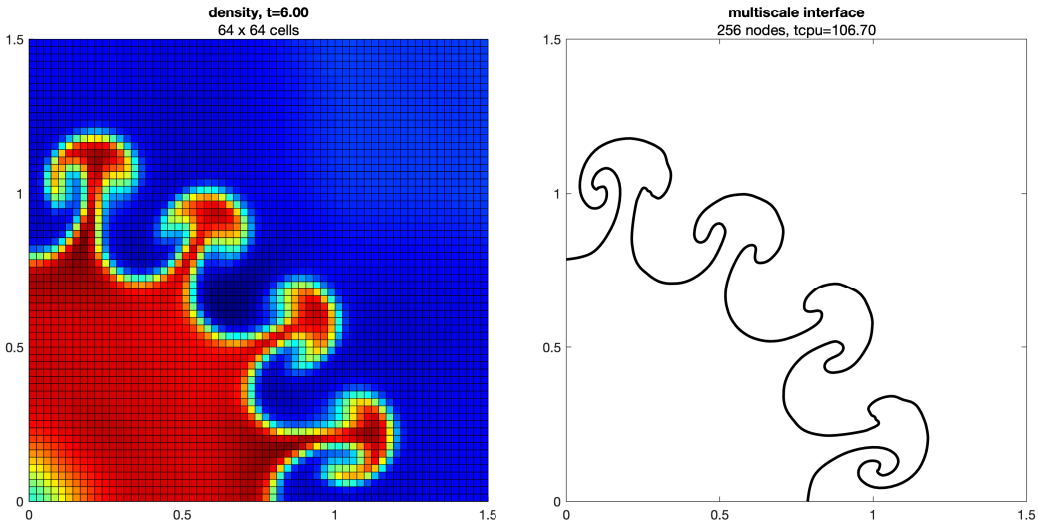
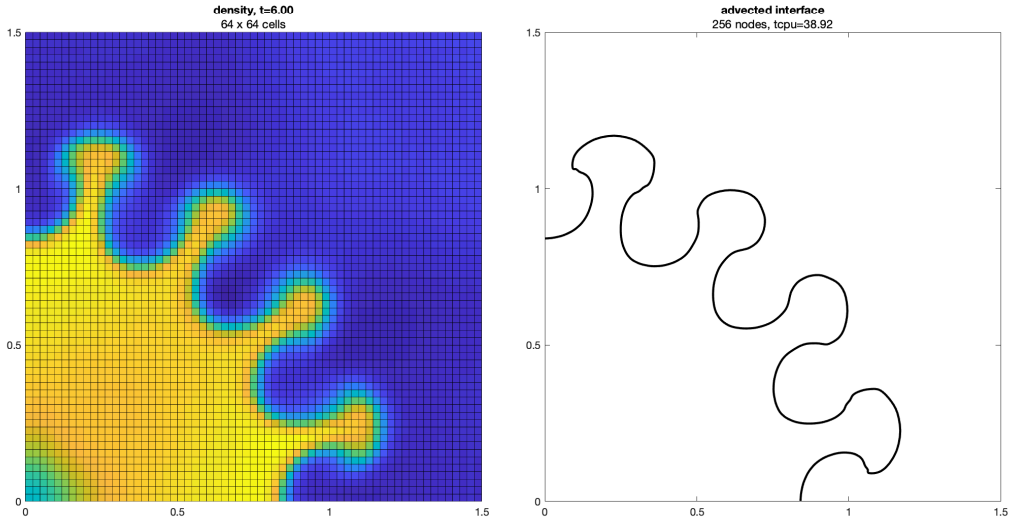


Figure 3.10: The perturbed radial Sod problem with constant Atwood number model and a 64×64 background mesh.



(a) The perturbed radial Sod problem with variable Atwood number model and a 64×64 background mesh.



(b) The perturbed radial Sod problem with no subgrid scale model and a 64×64 background mesh.

Figure 3.11: (a) Multiscale solution for the radial Sod explosion problem with azimuthal perturbation, computed using a 64×64 background grid and a 256-node interface. (b) C-method solution for the same problem, using the same 64×64 grid and identical parameters.

3.8 Conclusions

We have developed a multiscale computational framework that integrates the fine interfacial resolution of incompressible interface models like the z-model with the versatility of compressible flow solvers. By generalizing the z-model to compressible regimes through a continuous-singular vorticity decomposition, we enable accurate simulation of contact discontinuities in vortex-dominated flows with significant compressible effects. Coupling this model to a coarse-grid compressible background via a velocity decomposition yields substantial computational savings while preserving key physical features such as vortex roll-up and baroclinic vorticity generation. Our numerical experiments confirm the capability of the multiscale z-model to resolve fine-scale structure in RTI and RMI scenarios, even at reduced computational cost compared to uniformly high-resolution simulations. Moreover, our results on the radial explosion problem highlight the model's ability to handle dynamically evolving density ratios and complex interface geometries. Future studies will extend our methods to three-dimensional and axisymmetric regimes, as well as incorporate adaptive mesh refinement into the background flow, enabling even greater computational efficiency.

Bibliography

S. Albeverio and A. B. Cruzeiro. Global flows with invariant (gibbs) measures for euler and navier-stokes two dimensional fluids. *Commun. Math. Phys*, 129:431–444, 1990.

G. R. Baker and L. D. Pham. A comparison of blob methods for vortex sheet roll-up. *Journal of Fluid Mechanics*, 547:297–316, 2006.

G. R. Baker, D. I. Meiron, and S. A. Orszag. Boundary integral methods for axisymmetric and three-dimensional rayleigh-taylor instability problems. *Physica D: Nonlinear Phenomena*, 12 (1-3):19–31, 1984.

J. T. Beale and A. Majda. Vortex methods. i. convergence in three dimensions. *Mathematics of computation*, 39(159):1–27, 1982.

G. Birkhoff. Helmholtz and taylor instability. *Proc. symp. appl. math*, 13:55–76, 1962.

Guido Boffetta, Filippo De Lillo, and S Musacchio. Nonlinear diffusion model for rayleigh-taylor mixing. *Physical review letters*, 104(3):034505, 2010.

W. H. Cabot and A. W. Cook. Reynolds number effects on rayleigh–taylor instability with possible implications for type ia supernovae. *Nature Physics*, 2(8):562–568, 2006.

J. Canfield, N. Denissen, M. Francois, R. Gore, R. Rauenzahn, J. Reisner, and S. Shkoller. A comparison of interface growth models applied to rayleigh–taylor and richtmyer–meshkov instabilities. *Journal of Fluids Engineering*, 142(12):121108, 2020.

Patricia Ruiz Chapman and JW Jacobs. Experiments on the three-dimensional incompressible richtmyer-meshkov instability. *Physics of Fluids*, 18(7):074101, 2006.

R. L. Cole and R. S. Tankin. Experimental study of taylor instability. *The Physics of Fluids*, 16 (11):1810–1815, 1973.

A. W. Cook, W. H. Cabot, and P. L. Miller. The mixing transition in rayleigh–taylor instability. *Journal of Fluid Mechanics*, 511:333–362, 2004.

B. J. Daly. Numerical study of two fluid rayleigh-taylor instability. *The Physics of Fluids*, 10(2): 297–307, 1967.

D. G. Ebin. Motion of a slightly compressible fluid. *Proceedings of the National Academy of Sciences*, 72(2):539–542, 1975.

H. W. Emmons, C. T. Chang, and B. C. Watson. Taylor instability of finite surface waves. *Journal of Fluid Mechanics*, 7(2):177–193, 1960.

J. Glimm, J. W. Grove, X. L. Li, K. Shyue, Y. Zeng, and Q. Zhang. Three-dimensional front tracking. *SIAM Journal on Scientific Computing*, 19(3):703–727, 1998.

V. N. Goncharov. Analytical model of nonlinear, single-mode, classical rayleigh-taylor instability at arbitrary atwood numbers. *Physical review letters*, 88(13):134502, 2002.

R. Granero-Belinchón and S. Shkoller. A model for rayleigh–taylor mixing and interface turnover. *Multiscale Modeling & Simulation*, 15(1):274–308, 2017. URL https://doi.org/10.1137/16m1083463.

Steven W Haan. Onset of nonlinear saturation for rayleigh-taylor growth in the presence of a full spectrum of modes. *Physical Review A*, 39(11):5812, 1989.

C. W. Hirt and B. D. Nichols. Volume of fluid (vof) method for the dynamics of free boundaries. *Journal of computational physics*, 39(1):201–225, 1981.

JW Jacobs and SB Dalziel. Rayleigh–taylor instability in complex stratifications. *Journal of Fluid Mechanics*, 542:251–279, 2005.

S. Jiang, Q. Ju, F. Li, and Z. Xin. Low mach number limit for the full compressible magnetohydrodynamic equations with general initial data. *Advances in Mathematics*, 259:384–420, 2014.

S. Klainerman and A. Majda. Singular limits of quasilinear hyperbolic systems with large parameters and the incompressible limit of compressible fluids. *Communications on Pure and Applied Mathematics*, 34(4):481–524, 1981.

R. Krasny. A study of singularity formation in a vortex sheet by the point-vortex approximation. *Journal of Fluid Mechanics*, 167:65–93, 1986a.

R. Krasny. Desingularization of periodic vortex sheet roll-up. *Journal of Computational Physics*, 65(2):292–313, 1986b.

Zhi Lin, Jean-Luc Thiffeault, and Charles R Doering. Optimal stirring strategies for passive scalar mixing. *Journal of Fluid Mechanics*, 675:465–476, 2011.

R. Liska and B. Wendroff. Comparison of several difference schemes on 1d and 2d test problems for the euler equations. *SIAM Journal on Scientific Computing*, 25(3):995–1017, 2003.

J. Liu and Z. Xin. Convergence of vortex methods for weak solutions to the 2-d euler equations with vortex sheet data. *Communications on Pure and Applied Mathematics*, 48(6):611–628, 1995.

J. Liu and Z. Xin. Convergence of the point vortex method for 2-d vortex sheet. *Mathematics of computation*, 70(234):595–606, 2001.

M. C. Lopes-Filho, J. Lowengrub, H. J. Lopes, and Y. Zheng. Numerical evidence of nonuniqueness in the evolution of vortex sheets. *ESAIM: Mathematical Modelling and Numerical Analysis*, 40 (2):225–237, 2006.

G. Mathew, I. Mezić, and L. Petzold. A multiscale measure for mixing. *Physica D: Nonlinear Phenomena*, 211(1-2):23–46, 2005.

G. Métivier and S. Schochet. The incompressible limit of the non-isentropic euler equations. *Archive for Rational Mechanics and Analysis*, 158:61–90, 2001.

G. Pandya and S. Shkoller. Interface models for three-dimensional Rayleigh–Taylor instability. *Journal of Fluid Mechanics*, 959:A10, 2023.

G. Pandya and S. Shkoller. Subgrid-scale modeling of contact discontinuities. *In Preparation*, 2025.

R. Ramani and S. Shkoller. A multiscale model for rayleigh-taylor and richtmyer-meshkov instabilities. *Journal of Computational Physics*, 405:109177, 2020. URL https://doi.org/10.1016/j.jcp.2019.109177.

R. Ramani, J. Reisner, and S. Shkoller. A space-time smooth artificial viscosity method with wavelet noise indicator and shock collision scheme, Part 1: The 1-D case. *J. Comput. Phys.*, 387:81–116, 2019a. ISSN 0021-9991. URL https://doi.org/10.1016/j.jcp.2019.02.049.

R. Ramani, J. Reisner, and S. Shkoller. A space-time smooth artificial viscosity method with wavelet noise indicator and shock collision scheme, Part 2: The 2-D case. *J. Comput. Phys.*, 387:45–80, 2019b. ISSN 0021-9991. URL https://doi.org/10.1016/j.jcp.2019.02.048.

P. Ramaprabhu, Guy Dimonte, Y. N. Young, A. C. Calder, and B. Fryxell. Limits of the potential flow approach to the single-mode rayleigh-taylor problem. *Physical Review E*, 74(6):066308, 2006.

Lord Rayleigh. Investigation of the character of the equilibrium of an incompressible heavy fluid of variable density. *Proceedings of the London Mathematical Society*, s1-14(1):170–177, 1883.

K. I. Read. Experimental investigation of turbulent mixing by rayleigh-taylor instability. *Physica D Nonlinear Phenomena*, 12(1-3):45–58, 1984.

J. Reisner. Private communication, 2020.

J. Reisner, J. Serencsa, and S. Shkoller. A space-time smooth artificial viscosity method for nonlinear conservation laws. *J. Comput. Phys.*, 235:912–933, 2013. ISSN 0021-9991. URL https://doi.org/10.1016/j.jcp.2012.08.027.

J. R. Ristorcelli and T. T. Clark. Rayleigh–taylor turbulence: self-similar analysis and direct numerical simulations. *Journal of Fluid Mechanics*, 507:213–253, 2004.

B. Rollin and M. J. Andrews. On generating initial conditions for turbulence models: the case of rayleigh–taylor instability turbulent mixing. *Journal of Turbulence*, 14(3):77–106, 2013.

N. Rott. Diffraction of a weak shock with vortex generation. *Journal of Fluid Mechanics*, 1(1): 111–128, 1956.

David H Sharp. An overview of rayleigh-taylor instability. *Physica D: Nonlinear Phenomena*, 12 (1-3):3–18, 1984.

L. Székelyhidi. Weak solutions to the incompressible euler equations with vortex sheet initial data. *Comptes Rendus Mathematique*, 349(19-20):1063–1066, 2011.

G. I. Taylor. The instability of liquid surfaces when accelerated in a direction perpendicular to their planes. *Proceedings of the Royal Society of London. Series A*, 201(1065):192–196, 1950.

J. L. Thiffeault. Using multiscale norms to quantify mixing and transport. *Nonlinearity*, 25(2):R1, 2012.

S. Ukai. The incompressible limit and the initial layer of the compressible euler equation. *Journal of Mathematics of Kyoto University*, 26(2):323–331, 1986.

S. O. Unverdi and G. Tryggvason. A front-tracking method for viscous, incompressible, multi-fluid flows. *Journal of computational physics*, 100(1):25–37, 1992.

J. P. Wilkinson and J. W. Jacobs. Experimental study of the single-mode three-dimensional rayleigh-taylor instability. *Physics of Fluids*, 19(12):124102, 2007. URL https://doi.org/10.1063/1.2813548.

D. L. Youngs. Numerical simulation of turbulent mixing by rayleigh-taylor instability. *Physica D: Nonlinear Phenomena*, 12(1-3):32–44, 1984.

D. L. Youngs. Modelling turbulent mixing by rayleigh-taylor instability. *Physica D: Nonlinear Phenomena*, 37(1-3):270–287, 1989.

D. L. Youngs. The density ratio dependence of self-similar rayleigh–taylor mixing. *Philosophical Transactions of the Royal Society A: Mathematical, Physical and Engineering Sciences*, 371, 2013.

Y. Zhou. Rayleigh–taylor and richtmyer–meshkov instability induced flow, turbulence, and mixing. i. *Physics Reports*, 720-722:1–136, 2017a. Rayleigh-Taylor and Richtmyer-Meshkov instability induced flow, turbulence, and mixing. I.

Y. Zhou. Rayleigh–taylor and richtmyer–meshkov instability induced flow, turbulence, and mixing. ii. *Physics Reports*, 723:1–160, 2017b.

Y. Zhou, R. Williams, P. Ramaprabhu, M. Groom, B. Thornber, A. Hillier, W. Mostert, B. Rollin, S. Balachandar, P. Powell, A. Mahalov, and N. Attal. Rayleigh–taylor and richtmyer–meshkov instabilities: A journey through scales. *Physica D: Nonlinear Phenomena*, 423:132838, 2021.

Y. Zhou, J. D. Sadler, and O. A. Hurricane. Instabilities and mixing in inertial confinement fusion. *Annual Review of Fluid Mechanics*, 57:197–225, 2025.

ProQuest Number: 32241115

INFORMATION TO ALL USERS
The quality and completeness of this reproduction is dependent on the quality
and completeness of the copy made available to ProQuest.



Distributed by
ProQuest LLC a part of Clarivate (2025).
Copyright of the Dissertation is held by the Author unless otherwise noted.

This work is protected against unauthorized copying under Title 17,
United States Code and other applicable copyright laws.

This work may be used in accordance with the terms of the Creative Commons license
or other rights statement, as indicated in the copyright statement or in the metadata
associated with this work. Unless otherwise specified in the copyright statement
or the metadata, all rights are reserved by the copyright holder.

ProQuest LLC
789 East Eisenhower Parkway
Ann Arbor, MI 48108 USA